

5-1-2022

The Dissolution and Recovery of Critical Materials (Li₂CO₃ and UF₆) from Ionic Liquid

Cassara Higgins

Follow this and additional works at: <https://digitalscholarship.unlv.edu/thesesdissertations>

 Part of the [Chemistry Commons](#)

Repository Citation

Higgins, Cassara, "The Dissolution and Recovery of Critical Materials (Li₂CO₃ and UF₆) from Ionic Liquid" (2022). *UNLV Theses, Dissertations, Professional Papers, and Capstones*. 4409.
<http://dx.doi.org/10.34917/31813290>

This Dissertation is protected by copyright and/or related rights. It has been brought to you by Digital Scholarship@UNLV with permission from the rights-holder(s). You are free to use this Dissertation in any way that is permitted by the copyright and related rights legislation that applies to your use. For other uses you need to obtain permission from the rights-holder(s) directly, unless additional rights are indicated by a Creative Commons license in the record and/or on the work itself.

This Dissertation has been accepted for inclusion in UNLV Theses, Dissertations, Professional Papers, and Capstones by an authorized administrator of Digital Scholarship@UNLV. For more information, please contact digitalscholarship@unlv.edu.

THE DISSOLUTION AND RECOVERY OF CRITICAL MATERIALS (Li_2CO_3 AND UF_6)
FROM IONIC LIQUID

By

Cassara Jolleen Higgins

Bachelors of Science – Chemistry
Bachelors of Science – Physics
University of Northern Iowa
2016

A dissertation submitted in partial fulfillment
of the requirements for the

Doctor of Philosophy- Radiochemistry

Department of Chemistry and Biochemistry
College of Sciences
The Graduate College

University of Nevada, Las Vegas
May 2022

Dissertation Approval

The Graduate College
The University of Nevada, Las Vegas

March 30, 2022

This dissertation prepared by

Cassara Higgins

entitled

The Dissolution and Recovery of Critical Materials (Li_2CO_3 and UF_6) from Ionic Liquid

is approved in partial fulfillment of the requirements for the degree of

Doctor of Philosophy - Radiochemistry
Department of Chemistry and Biochemistry

David Hatchett, Ph.D.
Examination Committee Chair

Kenneth Czerwinski, Ph.D.
Examination Committee Member

Gordon Jarvinen, Ph.D.
Examination Committee Member

Ashkan Salamat, Ph.D.
Graduate College Faculty Representative

Kathryn Hausbeck Korgan, Ph.D.
*Vice Provost for Graduate Education &
Dean of the Graduate College*

Abstract

The Dissolution and Recovery of Critical Materials (Li_2CO_3 and UF_6) from Ionic Liquid

By

Cassara Jolleen Higgins

Dr. David W Hatchett, Committee Chair

Associate Vice President of Research, Professor of Chemistry and Radiochemistry

University of Nevada, Las Vegas

Lithium and uranium are critical materials in both the energy industry and for national security. Lithium is necessary for the next generation of batteries and ^6Li is valuable for the production of tritium necessary for both fusion energy and to maintain our nuclear stockpiles. Uranium is a fuel source or precursor fuel source for commercially operating nuclear fission power. The monitoring of uranium hexafluoride (UF_6) enrichment at foreign facilities is important for the monitoring of nuclear safeguards and enforcement of non-proliferation treaties.

Recovery methods for lithium at the end of life of batteries are necessary to ensure abundance of the element for commercial use. The ionic liquid (IL), 1-methyl-1-propylpiperidinium bis(trifluoromethylsulfonyl)imide ([MPPi][TFSI]) has an electrochemical window which encompasses the very negative (-3.04 V vs SHE) reduction potential of lithium. Pathways for direct and indirect dissolution of Li_2CO_3 into [MPPi][TFSI] were developed. The dissolved LiTFSI species was evaluated electrochemically. Two methods for recovery were explored. The first method consisted of holding the working electrode at one potential, and the second method pulsed the potential of the working electrode. Deposition was exhibited on both gold and several carbon electrodes. The recovered lithium was characterized using PXRD and SEM imaging.

The f-elements also typically have negative reduction potentials that are difficult to achieve in aqueous systems and the metals are often produced in traditional molten salts. ILs have the potential to achieve recovery of f-elements without the need for molten salt systems which require high quantities of thermal energy and are corrosive. The direct dissolution of UF_6 into $[\text{MPPi}][\text{TFSI}]$ was completed. The characterization and stability of the dissolved species was evaluated. The UF_6 was found to be stable in inert atmosphere in the $[\text{MPPi}][\text{TFSI}]$. Characterization was done using XAFS, UV-Vis, FT-IR, and Raman. Three routes for recovery of the uranium were completed. Two routes of recovery involved the precipitation of air and water stable uranium fluoride compounds. It was shown that uranium oxides could be obtained by heating the precipitates with available oxygen. The third route of recovery was electrochemically driven. This method achieved deposits of lithium hydride but was a low throughput method. Precipitates and deposits were evaluated through TGA, SEM-EDS, PXRD, UV-Vis, FT-IR, and Raman. Ultimately it was shown ILs could be used to stabilize the volatile UF_6 for conversion to stable waste forms. It was also shown that UF_6 in an IL could be shipped to another facility for recovery of the uranium for isotopic evaluation.

Acknowledgements

The journey of achieving a PhD requires more people to thank than can be listed here. I would like to first thank my advisor Dr. David Hatchett for providing with a positive graduate school experience. Dave gave me the space to grow and learn to be a scientist with which questions to ask and how to answer them. To Dr. Ken Czerwinski for adding to my lab experiences and providing council throughout my graduate experience. With the addition of Dr. Gordon Jarvinen and Dr. Ashkan Salamat to Dave and Ken for taking the time to serve on my committee and reading my dissertation. I would like to extend my thanks to the support of Wendee Johns, Julie Bertoia, and Kelley Seeley for keeping the radiochemistry program moving forward. To James Louis-Jean, Eddie Montoya, and Hughes Badet whom have all been at one-point roommates and several times supportive friends. Thank you for the support of the rest of the Hatchett group, Katherine Lubke, Phillip Hammer, Bea Martinez, and Nicole Golozov. I would also like to thank the greater UNLV Radiochemistry Family. I would like to acknowledge too fantastic communities I have had the pleasure of being a part of during my time in Las Vegas. Las Vegas Ultimate is where I made several of my first friends in Vegas and made Vegas home. Through the last few years of the pandemic, I started endurance running and have made several lifelong friends with Las Vegas Runners. I would not have stayed sane during the last six years without the collection of friends I made with these two communities.

Lastly, I would like to thank the two beings that have waited for me at home every day. Firstly, my dog Bailey, who I adopted about two weeks after moving to Vegas when I went to the Animal Foundation “just to look.” Bailey has always been there silently ready to offer any love I needed. Secondly, my fiancé and soon to be husband Chip. Chip who has loved and supported me through the dissertation writing process.

Table of Contents

Abstract	iii
Acknowledgements	v
List of Tables	x
List of Figures	xi
List of Equations	xvi
Chapter 1. Introduction	1
1.1 Motivation.....	1
1.2 Lithium Demand and Traditional Recovery as a Critical Material.....	1
1.3 History and Chemistry of Uranium Hexafluoride in the Nuclear Fuel Cycle	3
1.3.1 Traditional Processing of Spent Nuclear Fuel in the Nuclear Fuel Cycle	9
1.4 Overview of Room Temperature Ionic Liquids:.....	12
1.5 Room Temperature Ionic Liquids in the Nuclear Fuel Cycle.....	17
1.5.1 Radiolytic stability of ILs	18
1.6 Organization of Dissertation	19
Chapter 2. Experimental Methods	21
2.1 Dissolution of Critical Materials into [MPPi][TFSI].....	21
2.1.1 Dissolution of Li_2CO_3 into [MPPi][TFSI]	21
2.1.2 Dissolution of UF_6 into [MPPi][TFSI]	22
2.2 Electrochemical methods	23

2.2.1 Electrochemical Cell and Reference electrode production	31
2.3 Instrumentation and Analytical Methods.....	32
2.3.1 Ultraviolet Visible Spectroscopy	32
2.3.2 FT-IR.....	34
2.3.3 Raman Spectroscopy.....	36
2.3.4 Inductively Coupled Plasma- Atomic Emission Spectroscopy	39
2.3.5 X-Ray Absorption Fine Structure Spectroscopy.....	40
2.3.6 Scanning Electron Microscopy and Energy Dispersive X-ray Spectroscopy..	43
2.3.7 Powder X-Ray Diffraction.....	44
2.3.8 Thermal Gravimetric Analysis.....	45
2.3.9 Karl-Fisher Titration	46
Chapter 3. Dissolution and Recovery of Lithium from IL.....	48
3.1 Introduction.....	48
3.2 Methods and Materials.....	51
3.2.1 Chemicals and Solutions.....	51
3.2.2 Dissolution of Lithium.....	51
3.2.3 Electrochemical Methods for Deposition	52
3.2.4 Analysis Instrumentation	53
3.3 Dissolution and Electrochemical Response of Lithium in IL.....	54
3.4 Deposition of Lithium on Gold Electrodes	57

3.5 Deposition of Lithium on Carbon Electrodes	64
3.6 Conclusions.....	68
Chapter 4. Dissolution and Characterization of UF ₆ in [MPPi][TFSI].....	70
4.1 Introduction.....	70
4.2 Methods and Materials.....	76
4.2.1 Chemicals and Solutions.....	76
4.2.2 Dissolution of UF ₆	76
4.2.3 XAFS Studies.....	76
4.2.4 UV-Vis, FTIR, and Raman Spectroscopy.....	77
4.2.5 Electrochemical Studies.....	77
4.3 Dissolution of UF ₆ in IL	78
4.4 Characterization with XAFS Studies	79
4.5 UV-Vis Transition Assignments and other Spectral Data	83
4.6 Electrochemical Characterization	89
4.7 Conclusions.....	96
Chapter 5. Recovery of Uranium Species from the IL	97
5.1 Introduction.....	98
5.2 Methods and Materials.....	100
5.2.1 Chemicals and Solutions.....	100
5.2.2 Time Dependent Precipitation	101

5.2.3 Water Driven Precipitation	101
5.2.4 Electrochemical Recovery	101
5.2.5 Analysis Instrumentation	102
5.3 Time Dependent Precipitation of Uranium from IL	103
5.4 Water Driven Precipitation of Uranium from IL	109
5.4.1 Mass Balance Studies for Uranium Recovery Utilizing Water	113
5.4.2 Optimization Study for Uranium Recovery Utilizing Water	116
5.5 Spectral Characterization of Precipitates	120
5.6 Electrochemical Recovery of Uranium from IL	127
5.7 Conclusions	131
Chapter 6. Conclusions and Future Work	133
6.1 Conclusions:	133
6.2 Future Work:	135
References	137
Curriculum Vitae	156

List of Tables

Table 1: Absorption edge and white-line at the U_L3 edge of samples in Figure 32.	82
Table 2: Structural parameters obtained from the adjustment of the k3-EXAFS spectra of the solution samples at various ages and concentration.	83
Table 3: Data from Scan Rate Study.....	93
Table 4: Standard Uranium Reduction Potentials ⁸⁹	94
Table 5: Mass Work Up for Uranium Recovery for 0.26 M and 0.08 M Uranium at 4 hours and 1 week after addition to the [MPPi][TFSI].	114
Table 6: Uranium Recovery for 0.11 M UF ₆ at 4 days after addition to the [MPPi][TFSI].....	115
Table 7: Comparison of FT-IR peaks marked in red in Figure 61. All peaks are in cm ⁻¹ . Instrument resolution was 4 cm ⁻¹	124
Table 8: Possible vibrational frequency assignments for the time and water driven precipitates compared to UCl ₆ ²⁻ compounds in literature. All values are in cm ⁻¹	125

List of Figures

Figure 1: The Nuclear Fuel Cycle ¹⁷	4
Figure 2: Phase Diagram of UF ₆ ²³	6
Figure 3: Common IL anions, ordered by most viscous to least.	13
Figure 4: Structures of cations [BMMIm] and [BMIm].	14
Figure 5: Comparison of electrochemical windows of [Me ₃ NBu][TFSI] in the solid line with 0.1 M H ₂ O ₄ solution in the dashed lines with different working electrodes. ⁵⁷	16
Figure 6: P10 tube of UF ₆ shipped from URENCO	23
Figure 7: The electrode/solution interfaces when a negative potential is applied to the electrode. ⁷³	24
Figure 8: Potential profile of a two electrode cell between the interior of the working electrode and counter electrode. ⁷³	26
Figure 9: Potential profile in a three-electrode cell. ⁷³	27
Figure 10: A) a representation of applied potential over time. B) is current as a function of applied potential applied over time. ⁷⁵	29
Figure 11: Types of stretching (A) and bending (B) ⁷⁹	35
Figure 12: Schematic diagram of a Michelson interferometer. ⁷⁹	36
Figure 13: Schematic of Rayleigh, Stokes, and anti-Stokes scattering and how they are plotted in Raman spectroscopy. ⁸⁰	38
Figure 14: Schematic of an ICP-AES ⁸²	39
Figure 15: Example readouts of raw XAFS, background subtracted XANES, and k ³ -weighted EXAFS data. ⁸³	41

Figure 16: Radioactive solution sample holder on the left and a solid sample holder on the right.	42
Figure 17: Secondary containment sample holders for liquid and solid samples.....	42
Figure 18: Schematic of PXRD Instrumentation ⁸¹	45
Figure 19: Schematic of the Mettler Toledo D-32 Karl Fischer Titrator ⁸⁶	47
Figure 20: Cyclic voltametric response of an Au electrode in a. IL without Li. b. 0.5 M LiTFSI. and c. 0.7 M Li ₂ CO ₃ dissolved directly into IL. The scan rate was 0.1 V/s.	55
Figure 21: Cyclic voltametric response of a glassy carbon electrode in a. IL without Li. b. 0.5 M LiTFSI. and c. 0.5 M Li ₂ CO ₃ dissolved directly into IL.....	57
Figure 22: a. Li deposits obtained from steady state potential of -3.6 V vs. Ag/AgCl. b. Li deposits obtained from differential pulse methods. c. dendritic deposits collected from constant potential deposition. Solutions contained 0.5 M Li.	59
Figure 23: SEM images of a. Pristine Au electrode. b. Au electrode after 20 cycles between -3.6 V and +3.6 V vs. Ag/AgCl. c. Au electrode after the steady-state deposition method. d. Au electrode after the differential pulse method.	60
Figure 24: Powder X-Ray Diffraction (PXRD) of Li deposits at a gold electrode. a. Raw data b. Fit data for LiH, and c. the difference between raw data and the fit.	62
Figure 25: Deposits on glassy carbon electrode in glove box after 44 hours of deposition at -3.6 V inside the glove box.	65
Figure 26: The grafoil electrode after 20 hours at -3.6 V in the glovebox.	66
Figure 27: The screen-printed electrode after 42 hours of total deposition time on PXRD stage before exposure to atmosphere.	66
Figure 28: Glassy carbon sheet electrode after 24 hours at -3.63 V vs Ag/AgCl.....	67

Figure 29: Lithium deposits on carbon fiber electrode after 40 hours of pulsed deposition.	67
Figure 30: A 0.1 M solution A) as addition occurred, B) after shaking C) two days later	79
Figure 31: Fitted k3-EXAFS spectra (bottom) and Fourier Transform (top) of k3-EXAFS spectra of 0.1 M UF ₆ in [MPPi][TFSI] at 10 days old. Adjustment between $k = [2.4-12.5] \text{ \AA}^{-1}$. Residual = 3.27%. Experimental data in black and fit in orange. Fitted for 6.2 ± 1.2 U-F bonds at $2.05 \pm 0.02 \text{ \AA}$	81
Figure 32: Normalized XANES spectra at the U_L3 edge of (a.) 1 week 100mM UF ₆ (b.) 6 month old 100mM UF ₆ and (c.) 6 month old 700mM UF ₆	82
Figure 33: Normalized XANES spectra at the U_L3 edge of the same samples with standards.	83
Figure 34: UV-Vis over time of 0.1 M UF ₆ in [MPPi][TFSI]. The bottom spectrum was 4 hours, 24 hours and the top being 8 days. The 24 hour and 8 day spectra are shifted up for comparison.	84
Figure 35: IR Spectra of 0.1 M UF ₆ in [MPPi][TFSI] over the course of a week.....	86
Figure 36: The difference in the spectra after subtracting the [MPPi][TFSI] from the aged UF ₆ solutions.	87
Figure 37: Raman spectra of [MPPi][TFSI] and 0.5 M UF ₆ in [MPPi][TFSI] at 1 week old.	88
Figure 38: Raman Spectra with labeled U(V) vibrations.....	89
Figure 39: Cyclic voltammetry of the 0.096 M UF ₆ in [MPPi][TFSI] with a glassy carbon electrode.....	90
Figure 40: Isolated U(V) /U(IV) redox couple (in red) and coupled with the U(IV) to U(V) peak (in blue).....	91
Figure 41: Scan rate study of U(V)/U(IV) couple with glassy carbon disc electrode.	92
Figure 42: Peak currents graphed as a function of the square root of scan rate.	93

Figure 43: A 0.95 M UF_6 in IL freshly made, after 1 day, 8 days, and 49 days.	104
Figure 44: Changes in UV-Vis of 0.1 M UF_6 in $[\text{MPPi}][\text{TFSI}]$ over extended time.	104
Figure 45: Changes in the FT-IR of a 0.1 M UF_6 solution over a week and a 0.6 M UF_6 solution at 138 days.	105
Figure 46: Solid precipitates collected from a 0.7 M UF_6 solution.	106
Figure 47: PXRD of UF_6 precipitate. In blue is the pattern for $\text{UF}_4(\text{H}_2\text{O})_2$	107
Figure 48: TGA of three separate samples of the precipitates that form over time.	108
Figure 49: PXRD of time dependent precipitate after running TGA/DSC.	108
Figure 50: PXRD of sample after heating time dependent precipitate in tube furnace.	109
Figure 51: 5.6 mL of 0.04 M solution of UF_6 in $[\text{MPPi}][\text{TFSI}]$ with 4.4 mL of DI H_2O shaken by hand, centrifuged, solid filtered from solution.	110
Figure 52: PXRD of UF_6 water driven precipitates fitted to $\text{UF}_4 \cdot 1.5(\text{H}_2\text{O})$	111
Figure 53: TGA results of the water-induced.	112
Figure 54: PXRD of water driven precipitates after running TGA/DSC.	112
Figure 55: UV-Vis of aqueous phase after extraction of uranium.	114
Figure 56: The two tubes on the left received a 3 μL spike of water, the middle two received a 30 μL spike of water and the right two received a 300 μL spike of water.	117
Figure 57: Gelatinous material produced from 3 and 30 μL spikes. Pictured is a 3 μL sample.	118
Figure 58: On the left are the vials of dried gel from the two 3 μL (top) and two 30 μL (bottom).	118
Figure 59: On the right are the $[\text{MPPi}][\text{TFSI}]$ samples after the secondary 3 mL water extraction with the samples from top to bottom in sets of two, 3 μL , 30 μL , and 300 μL initial water spikes.	119

Figure 60: UV-Vis of the time dependent, water driven precipitates and [MPPi][Cl].	121
Figure 61: FT-IR Spectra of HTFSI, [MPPi][Cl], time dependent and water driven precipitates.	123
Figure 62: Raman of the time dependent and water driven precipitates with [MPPi][TFSI].....	125
Figure 63: Averaged TGA mass losses for the time and water precipitates with labeled temperature ranges.	126
Figure 64: Cyclic voltammetry of the 0.082 M UF_6 in [MPPi][TFSI] on gold foil electrode....	128
Figure 65: A) A photo of the cell before deposition began, B) after 20 hours of deposition, and C) is after the final 40 hours of deposition at -3.5 V.	128
Figure 66: A) the electrode after being removed from the IL. B) the solution remaining in the cell with the deposits.	129
Figure 67: SEM images of gold electrode after UF_6 deposition.....	130
Figure 68: SEM image where point EDS was completed showing the deposits to be uranium. The EDS for spectrum 1 and 2 are shown below.....	130

List of Equations

Equation 1: Conversion UO_2 to UF_4	4
Equation 2: Oxidation of UF_4 to UF_6	5
Equation 3: Conversion of UF_6 to UO_2F_2	8
Equation 4: Reduction of UO_2F_2 to U_3O_8 (United States Method)	8
Equation 5: Reduction of UO_2F_2 to U_3O_8 (French Method)	9
Equation 6: Reduction of UO_2F_2 to UO_2	9
Equation 7: Guzman-Andrade Law	14
Equation 8: Vogel-Tamman-Fulcher equation	14
Equation 9: Stokes-Einstein Equation for Diffusion	15
Equation 10: Conversion of Li_2CO_3 to LiTFSI	21
Equation 11: Side reaction of LiTFSI production.....	21
Equation 12: Faraday's Law.....	25
Equation 13: Relation of current to reaction rate, v ($\text{mol sec}^{-1} \text{ m}^{-2}$).	25
Equation 14: Ohm's Law.....	26
Equation 15: The Nernst Equation.....	30
Equation 16: The Randles-Sevciks Equation.....	30
Equation 17: Equation relating peak current to scan-rate with an electrode absorbed species. ...	31
Equation 18: Beer-Lambert Law	33
Equation 19: Bragg's Law	44
Equation 20: Chemical Reaction utilized in a Karl Fischer Titration.....	46
Equation 21: Chemical reactions with the anolyte and water.....	47
Equation 22: Synthesis of LiTFSI from Li_2CO_3	50

Equation 23: Evolution of carbon dioxide	51
Equation 24: Oxidation of Gold.....	56
Equation 25: Hydrogen Evolution	56
Equation 26: Reaction of UF_6 with water	72
Equation 27: Reaction to covert uranyl fluoride to U_3O_8	72
Equation 28: Reaction to covert uranyl fluoride to UO_2	72
Equation 29: Dissolution of UO_2CO_3 with HTFSI.....	74
Equation 30: Possible fragmentation of TFSI• radical ¹²⁵	88
Equation 31: Randles-Sevcik equation for a fully reversible system.	92
Equation 32: Randles-Sevcik equation for a quasi-reversible or irreversible system.	92
Equation 33: Proposed Mechanism for the Dissolution and Reduction of UF_6	96
Equation 34: Chemical reaction for the water driven precipitation.	116

Chapter 1. Introduction

1.1 Motivation

The work presented in this dissertation explores the dissolution and recovery of strategically important materials including lithium and uranium hexafluoride (UF_6), into room temperature ionic liquids (ILs). Specifically, the first part of the dissertation focuses on the dissolution of Li_2CO_3 into 1-methyl-1-propylpiperidinium bis(trifluoromethylsulfonyl)imide ([MPPi][TFSI]). This is followed by an evaluation of pathways for electrochemical recovery of the lithium with different deposition techniques and electrode materials. The second part of the dissertation examines the direct dissolution and characterization of UF_6 into [MPPi][TFSI]. Several precipitation and electrochemical recovery methods were examined for the recovery of the uranium after dissolution of UF_6 . The reactive dissolution of UF_6 via ILs is significant impacting both the nuclear fuel cycle and nuclear safeguards for non-proliferation.

1.2 Lithium Demand and Traditional Recovery as a Critical Material

Industrial uses of lithium include ceramics, glass, lubrication greases, and batteries.¹ However, the development of portable consumer electronics of 1970's necessitated the development of small lithium batteries with manganese dioxide cathodes. Initially these were single use batteries, but interest quickly transitioned to the rechargeable lithium-ion batteries (LIBs).² A recent study modeling lithium demand showed an increase from 25 kt Li/yr in 2008 to 400 kt Li/yr by 2050 and 857 kt Li/yr by 2200. The primary cause of increased demand stems from the penetration of electric vehicles into the auto industry and the use of LIBs.³ Another study expects increasing lithium demand for electric vehicles through 2042 before leveling out. They predict a lithium inflow of 850 kt Li/yr by 2050, an increase from 32 kt Li/yr in 2012.⁴ The

large-scale industrial use of Li is somewhat hindered by the fact that lithium abundance in the earth's crust is less than 0.01% by weight. Furthermore, the majority of lithium is currently produced from natural brines and ore mining with less than 1% produced from recycled materials.⁵ In fact, the recycling of LIBs has primarily focused on the recovery of other materials including cobalt, copper, and nickel.⁶

The increasing demand of Li suggests that recovery of Li from batteries will become increasingly important in the supply chain as the production from mining becomes more expensive. The use of lithium metal electrodes in LIBs will continue to focus on producing batteries with the highest possible specific energy thereby increasing demand. The traditional use of Li in LIBs involves the repetitive oxidation/reduction or cycling of lithium ion using LiCoO_2 that can form small microstructures called dendrites on the electrode surface.⁷ The specific energy can only be maintained if the cycling of lithium is fully reversible and the formation of dendrites is minimized.⁸ Reducing dendrites allows the battery to more fully charge and discharge over time increasing the lifetime. The development of next generation battery systems such as Li-Sulfur and Li-Air battery systems are specifically concerned with controlling the formation of dendrites.^{9,10} The aggregation of dendrites can also compromise the battery safety if the deposits are sufficient such that an ohmic connection between the cathode and anode occurs within the cell¹¹. Therefore, dendritic formations of lithium deposits are currently the main limiting factor in the LIBs lifecycle.

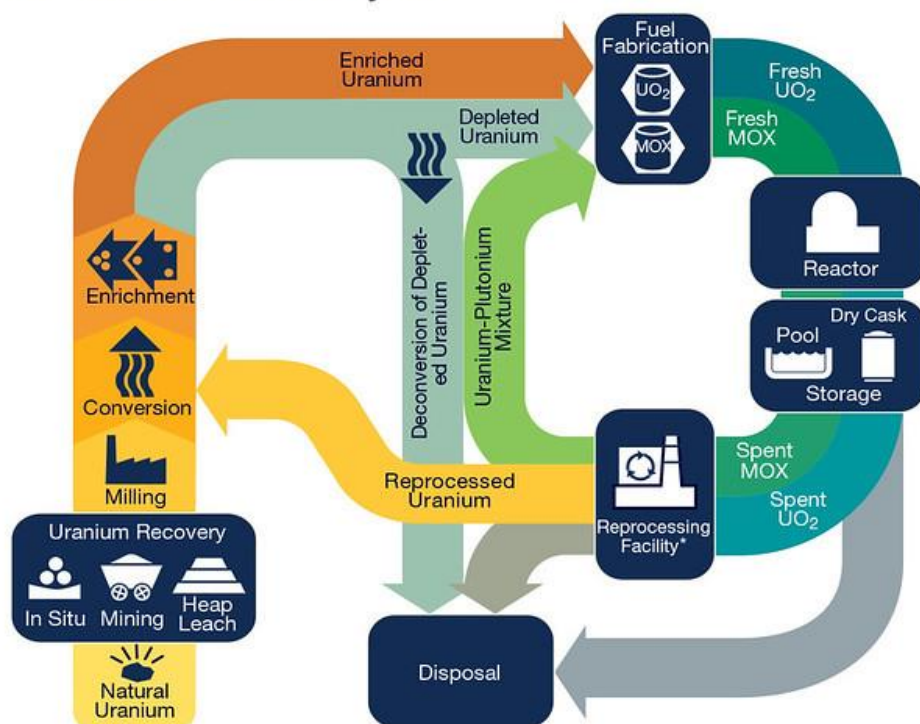
The Toxco process is a traditional method that has been used for the commercial recovery of lithium since 1993.^{6,12,13} In fact, the Toxco process was demonstrated with the Tesla Roadster automotive pack recently.¹³ The Toxco process utilizes liquid nitrogen to reduce lithium reactivity while the batteries are shredded to one-inch pieces. The lithium containing material is

reacted with an aqueous solution of LiOH at pH 10 in a reaction vessel. The water is then evaporated to precipitate out LiCl, Li₂CO₃, and LiSO₃ from the supersaturated solution. All of the materials listed are collected and dissolved in dilute sulfuric acid in a container equipped with an electrolytic membrane to separate the lithium ions from the various anions. Finally, the Li ions are precipitated as LiOH and converted to Li₂CO₃.¹⁴ The Toxco process has been utilized because it is a simple hydrometallurgical process with acceptable energy efficiency and high metal recovery rates with reasonable purities. However, it does require corrosive reagents and it produces a highly acidic waste stream which can limit the economic value.¹⁵ For comparison, pyrometallurgical processes melt spent LIBs, smelting and oxidizing the components to polymetallic slags. These processes produce hazardous gas and liquid waste and have high rates of loss of valuable materials. In addition, the molten process is energy expensive when compared to the more traditional chemical methods.^{15,16}

1.3 History and Chemistry of Uranium Hexafluoride in the Nuclear Fuel Cycle

The nuclear fuel cycle is the process of taking mined natural uranium and processing it to a material that can be used to produce usable electricity. The full cycle is shown in Figure 1. A country can have an open or closed fuel cycle. In an opened fuel cycle, spent nuclear fuel is not reprocessed, instead it is sent directly for disposal. In a closed fuel cycle, the spent nuclear fuel is reprocessed and placed back into a nuclear power plant to be burned again. Commercial nuclear power plants in the United States exclusively participate in the open nuclear fuel cycle. The open fuel cycle necessitates the continuous enrichment of uranium to be used as fuel.

The Nuclear Fuel Cycle

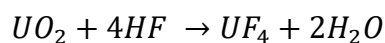


* Reprocessing of spent nuclear fuel, including mixed-oxide (MOX) fuel, is not currently practiced in the United States.
Note: The NRC has no regulatory role in mining uranium.

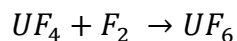


Figure 1: The Nuclear Fuel Cycle¹⁷

Natural Uranium is 99.28% and 0.0055% non-fissile ^{238}U and ^{234}U respectively and 0.720% fissile ^{235}U . Through an acid leaching process, uranium ore is converted and purified to UO_2 . In order to use uranium as a fuel source for nuclear power it must be enriched to 3-5% ^{235}U .¹⁸ The historical and current enrichment processes rely on the inherent physical properties (volatility) of UF_6 to achieve enrichment¹⁹. During the conversion step of the fuel cycle, the UO_2 is converted to UF_6 utilizing the reactions in Equation 1 and Equation 2.



Equation 1: Conversion UO_2 to UF_4



Equation 2: Oxidation of UF₄ to UF₆

Evaluation of the phase diagram (Figure 2) suggests room temperature UF₆ is a colorless, volatile solid. The solid can be liquefied at 64 °C with heating at reduced pressure. Finally, the triple point at 65 °C allows for UF₆ to be sublimed to a gas.²⁰ Thus, gaseous diffusion, gas centrifuges, and laser separation techniques have all been used to exploit the physical properties of UF₆ for enrichment. The single, naturally occurring isotope of fluorine, ¹⁹F, makes UF₆ an ideal compound for isotopic separation by minimizing the total number of compound masses possible.²¹ UCl₆ has similar physical properties without the ability to produce HF gas.²² However, there are two naturally occurring isotopes of chlorine, ³⁵Cl and ³⁷Cl, resulting in multiple mass combinations, complicating the enrichment process. With UF₆ there are two compound masses, 352 and 349 corresponding to ²³⁸U and ²³⁵U.

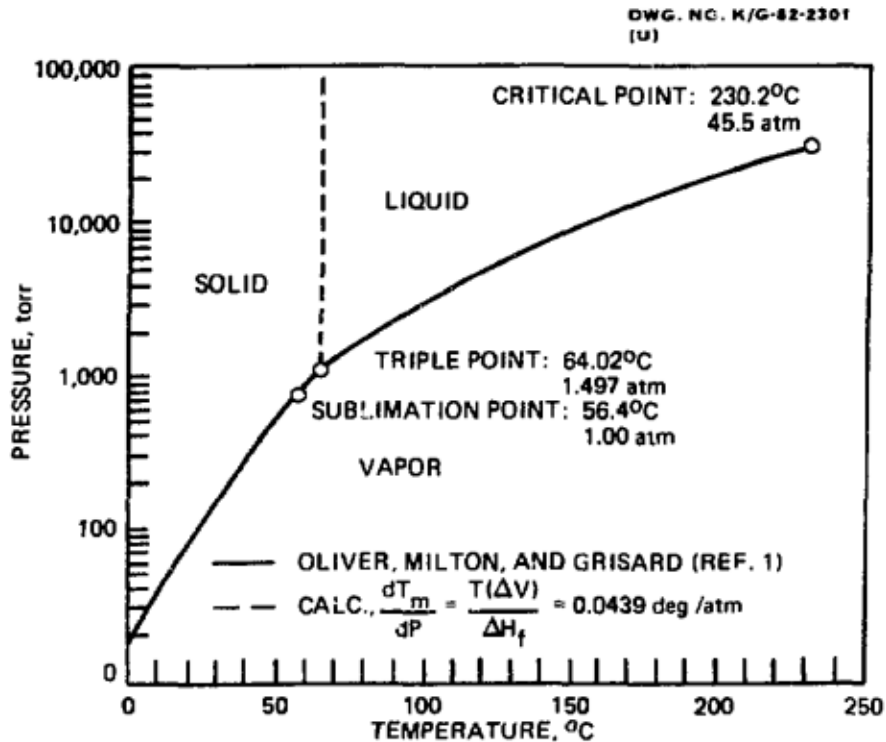


Figure 2: Phase Diagram of UF_6 ²³

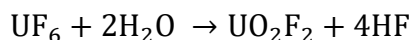
Enrichment techniques utilize the volatility of UF_6 . The two main processes of enrichment involve either gaseous diffusion or centrifugation. Within a gaseous diffusion cell, the UF_6 molecules are in thermal equilibrium and all isotopes having the same kinetic energy. The lighter $^{235}\text{UF}_6$ molecules travel at a higher velocity resulting in more collisions with the porous diffusion barrier, thus increasing concentration of ^{235}U within each sequential diffusion cell. In gas centrifugation, the isotopes are spun in large cylinders with a feed inlet in the center. Centrifugal force moves the heavier $^{238}\text{UF}_6$ preferentially to the outside and the lighter ^{235}U to the inside. The separation factor is dependent on the peripheral speed and temperature of the gas. Separate output lines collect the enriched and depleted gases. Additional centrifugations could be completed until the desired level of enrichment was obtained.²⁴

In 1999 the DOE produced a programmatic environmental impact statement (PEIS) that evaluated impact and needs of the then 704,000 metric tons of depleted UF_6 (DUF_6) waste found at three DOE sites.²⁵ The PEIS listed options for the waste ranging from doing nothing to converting the waste to either metal or oxides to be stored as waste or for future use. The record of decision (64 FR 43358) then stated the DOE decided to convert the DUF_6 , using as much as possible and storing the rest for future use or disposal.²⁶ Meanwhile, as of 2019, the world capacity for synthesizing UF_6 was 62,000 metric tons of uranium per year (tU/yr), but only utilized 34,500 tU. After enrichment, about 90% of the original UF_6 is DUF_6 . This stream is stored primarily as UF_6 in 15 ton drums. As of 2007, only one fourth of the world's 1.5 million tons of DUF_6 had been converted back to uranium oxides or UF_4 .²⁷ The accumulation of DUF_6 from enrichment has become more significant over time and the material must be stored safely. After the PEIA decision, two reprocessing plants were decided on at the Paducah and Portsmouth enrichment sites and projected to open in 2010.²⁵ However over the past two decades there have been several delays along with a safety related shutdown in 2015. As of 2018, four of seven conversion lines have reopened. All seven lines are expected to be running at full capacity by 2022.²⁶ At full capacity it will take approximately 25 years to convert the current US DUF_6 waste to an oxide form.^{18,25,26}

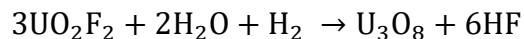
While the phase diagram of UF_6 is advantageous for enrichment methods, it also creates hazards for transporting and storing UF_6 . Typically, DUF_6 is stored in large cylinders as a solid. If the UF_6 melts to a liquid, it expands by 40%. This can result in burst containment and cause release of material. Once released, UF_6 is highly reactive with moisture in the air to produce HF and a fine cloud of UO_2F_2 .²⁸ The hydrolysis of UF_6 is vigorous and exothermic (-211.3 kJ/mol)²² when exposed to water, producing UO_2F_2 (Equation 3). The hydrolysis of UF_6 through inhalation

poses a severe risk where the in-situ formation of UO_2F_2 and subsequent formation of HF could occur in the lungs providing a long-term radiological dose. Moreover, the production of HF can target Ca in bones forming CaF_2 deposits in addition to the fact it is a known irritant to the eyes, skin, and mucus membrane.²⁹ The compounds UF_6 , UO_2F_2 , and HF are all strong fluorinating agents that will react with most oils, lubricants, and metals. The UF_6 must be contained with fluorocarbons, chlorocarbons, nickel, aluminum or their alloys.²⁴ The high volatility and possible exposure risk for UF_6 if inhaled or ingested can be mitigated by safely converting the species to a less reactive and volatile species to reduce the chemical hazards associated with storage and to individuals.³⁰

The current deconversion methods implemented at Paducah and Portsmouth enrichment plants are shown in Equation 3 and Equation 4. The gaseous UF_6 is purposefully reacted with water vapor to produce UO_2F_2 and HF. While vaporized, the UO_2F_2 is heated to 700 °C and reacted further with water vapor and H_2 to produce the black U_3O_8 powder.³¹



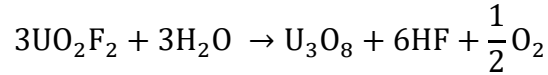
Equation 3: Conversion of UF_6 to UO_2F_2



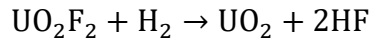
Equation 4: Reduction of UO_2F_2 to U_3O_8 (United States Method)

The compound U_3O_8 has been produced at AREVA's W plant in France, without the addition of H_2 for several decades. Vapor UF_6 is reacted with water vapor with a N_2 air stream. U_3O_8 is then collected (Equation 5). Typically U_3O_8 is the oxide of choice for storage.³² When enriched UF_6 is

used for fuel it is further processed to UO_2 through reduction of UO_2F_2 with H_2 gas (Equation 6).³³



Equation 5: Reduction of UO_2F_2 to U_3O_8 (French Method)



Equation 6: Reduction of UO_2F_2 to UO_2

1.3.1 Traditional Processing of Spent Nuclear Fuel in the Nuclear Fuel Cycle

After enrichment UO_2 can be used as fuel in light water reactors. After removal from the reactor and spending several months in cooling pools, the spent nuclear fuel is processed to separate the high and low activity waste products for disposal. Important fission products from light water reactor plants are ^{137}Cs , ^{90}Sr , and ^{99}Tc due to their long half-lives and mobility in the environment. Also produced are trans-uranic actinides (TRUs) such as neptunium, plutonium, americium, and curium. The ^{239}Pu isotope is particularly important due to its fissile nature and ability to be used in nuclear weapons. For a separation method to be proliferation resistant, plutonium should not be isolated. The actinides have a large range of potential oxidation states. This characteristic causes their unique behaviors compared to all other elements and is exploited in separating the actinides from other elements. Primarily separation is completed using aqueous and organic extractions or pyrochemical processes.³⁴

One of the main processes completed is the Plutonium and Uranium Recovery by Extraction (PUREX). In the first step of PUREX the irradiate fuel is dissolved in 7M HNO_3 . A

liquid/liquid extraction is completed with 30% tri-butyl phosphate (TBP) in odorless kerosene (OK). The TBP complexes with the UO_2^{2+} and the Pu(IV), extracting them into the organic phase, leaving the fission products and trivalent TRUs in the aqueous phase. From the organic phase the Pu(IV) is reduced to Pu(III) and back extracted into the aqueous phase. After the removal of the Pu, uranium can be extracted from the organic phase with dilute HNO_3 .³⁵ This process does result in the separation of pure plutonium.³⁵ The initial aqueous phase of the PUREX process can be further processed with the transuranic extraction (TRUEX) process to remove the TRUs. Either carbamoylmethyl-phosphineoxide (CMPO) or carbamoylmethyl-phosphate (CMP) is dissolved in a hydrocarbon solvent and selectively extracts the trivalent transuranics.³⁴

At current day the US does not reprocess but has investigated UREX process, extracting uranium and technetium, leaving plutonium in the aqueous phase with the other transuranics and fission products. The UREX process is proliferation-resistant since it does not separate the plutonium. The plutonium is complexed by adding acetohydroxyl amine as a complexing agent to the initial aqueous phase to prevent the extraction of the plutonium to the organic phase. Additional processes can be added onto the back end of the UREX process to continue to separate out specific TRUs or fission products to partitioned into separate waste streams or to be used in other applications. Uranium and technetium are separated via ion exchange. TRUEX after UREX can be used to separate the actinides and lanthanides from other fission products. Finally the trivalent actinide lanthanide separation with phosphorus-reagent extraction from aqueous complexes (TALSPEAK) process can be completed to separate the lanthanides from the remaining actinides.³⁶

Aside from liquid-liquid separation techniques, there are nonaqueous processes for the separations of spent nuclear fuel. In the 1960s it was explored if the hexafluorides of U, Pu, and Np could be used to separate the three actinides from other spent fuel as all three were volatile. After a route of fluorination was determined for the oxides, the separation factors were tested. The process was successful for the stable UF_6 , but was less successful for the PuF_6 and NpF_6 . The PuF_6 and NpF_6 tended to decompose and deposit as solid fluorides throughout the equipment. It was concluded that fluoride volatility processing would only be practical for the separation of uranium.³⁷

Molten salt systems are used in the pyrochemical processes, conducted at high temperatures between 500 and 800 °C. These processes have high separation factors of elements of the same chemical families. However, this process can be difficult and expensive due to the requirement of the structural materials to withstand the high temperatures and corrosive nature of the molten salts. The Integral Fast Reactor (IFR) fuel separation process has been developed at Argonne National Lab. The IFR process selectively electrorefine U, Pu, and other TRUs in a molten chloride salt using a molten cadmium solvent anode. Typically to prevent the isolation of Pu, it is removed with the minor TRUs into the liquid anode at once but the process can be made selective by making adjustments to the potential used.³⁴

Current methods for processing spent nuclear fuel primarily occur in volatile organic compounds (VOCs) or in high temperature, corrosive molten salts. The VOCs can be detrimental to our atmosphere, influencing regional photochemistry and having potential impact on global warming. They are also potentially toxic and carcinogenic if released into the environment.³⁸ The utilization of molten salts requires expensive alloys able to withstand the corrosive nature of fluoride and chloride salts. Room temperature molten salts or ionic liquids have the potential to

replace the organic solvents and extractants of liquid-liquid separations as well as perform as the medium for electrochemical separation methods currently conducted in molten salts.

1.4 Overview of Room Temperature Ionic Liquids:

Room temperature ionic liquids (ILs) are composed of often an organic cation and anion with a melting point at or below 100 °C.³⁹ The much lower melting point differentiates ILs from molten salts. Molten salts are inorganic salts with melting points between 150 to 1000°C and are often corrosive in nature.⁴⁰ Early ILs were aluminum halides with imidazolium or pyridinium halides. The first electrochemical studies in ILs were reported in 1975 in a 2:1 ratio of aluminum chloride to Ethylpyridinium bromide. These early ILs were very water sensitive, leading them to be difficult to work with and require inert atmospheres.⁴¹ In the 1990's modern ILs were produced by replacing the haloaluminate analogs to tetrafluoroborate ([BF₄]) or hexafluorophosphate ([PF₆]) anions. These new ILs were less sensitive to air and water, allowing them to be produced and used outside of the glovebox.⁴²

Ionic Liquids have several attractive qualities, giving rise to research in using them for electrochemical studies. They have negligible vapor pressure and are nonflammable. They also have high thermal stability up to 300 to 500 °C.⁴³ The anion and cation pairs can be selected to engineer solubility for either polar or nonpolar solutes. The ionic make-up of the ILs allows them to be used without supporting electrolyte and have high conductivity. Their resilience to reduction and oxidation gives rise to electrochemical windows larger than those of traditional aqueous and organic solvents.⁴⁴ ILs are however not resistant to sonication and degrade over time.⁴⁵ The major drawback of ILs are their high viscosities and low metal solubility.⁴⁶

Ionic Liquids have viscosities that are often one to three orders of magnitudes higher than traditional aqueous and organic solvents. For any given cation, the viscosity of an IL is

determined by the size and shape of the anion. Viscosity tends to be lower for large anions like bis(trifluoromethylsulfonyl)imide ([TFSI]) and higher for non-planar, symmetrical anions like $[\text{PF}_6]^{43,47}$ (Figure 3). The delocalization of electrons in the S-N-S backbone of the [TFSI] anion assists in decreasing the strength of interactions between it and the cation.⁴⁸ Other factors can play into viscosity aside from shape and size including the anion's ability to form hydrogen bonds or increased van der Waal's forces. The bulkier bis(perfluoroethylsulfonyl)imide anion ([BETI]) has a viscosity about 100 mPa·s larger than the smaller [TFSI]. The increased number of fluorides in the [BETI] increases the hydrogen bonding that occurs with the cations of the IL.⁴⁸

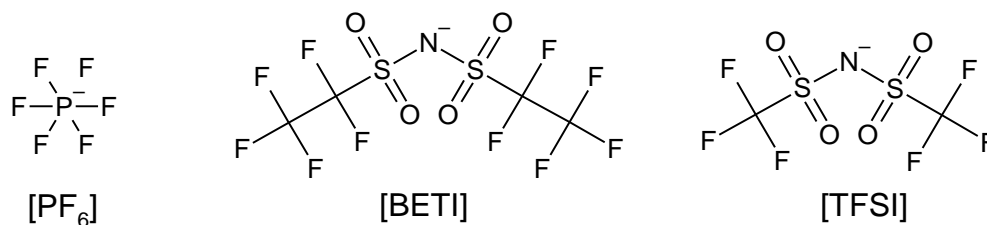


Figure 3: Common IL anions, ordered by most viscous to least.

The make-up of the cation similarly plays a role in the viscosity of the IL. The longer alkyl chained substituents produce stronger van der Waals interactions, increasing viscosity.⁴⁹ The branching of alkyl chains however, decreased viscosity.⁵⁰ A different study of 1-alkyl-3-imidazolium chloride ([BMIm][Cl]) and 1-alkyl-2,3-dimethyl-imidazolium chloride ([BMMIm][Cl]) was completed (Figure 4). It was expected that the additional methyl group in [BMMIm] would decrease the strength of the cation-anion interaction, therefore decreasing viscosity. The results of the study however showed viscosity increasing in the [BMMIm][Cl].

Calculations of the cation-anion interactions do show decreased strength, showing other factors increase the viscosity. The addition of the methyl group decreased the entropy of the IL, restricting the number of ion-pair configurations and resulting in increased order in the IL.⁵¹

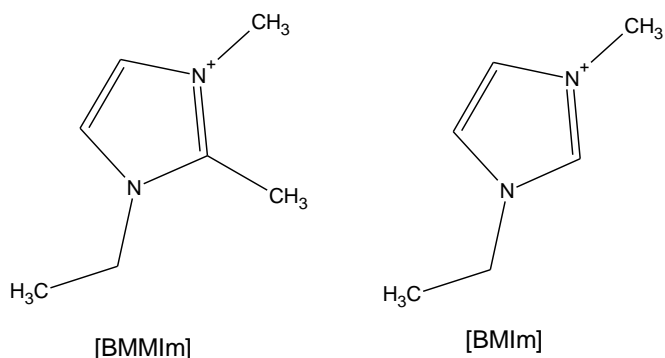


Figure 4: Structures of cations [BMMIm] and [BMIm].

Increasing temperature has been found to significantly decrease the viscosity of the ILs. Viscosity of ILs followed either the Arrhenius-type relationship (Guzman-Andrade Law) (Equation 7) or Vogel-Tamman-Fulcher (VTF) (Equation 8) equation.⁵²

$$\eta = A e^{E/(RT)}$$

Equation 7: Guzman-Andrade Law

$$\eta = \eta_0 e^{B/(T-T_0)}$$

Equation 8: Vogel-Tamman-Fulcher equation

Where E is activation energy of viscous flow and η_0 (mPa s), B (K), and T_0 (K) are all constants. ILs that followed the Arrhenius law contained asymmetrical cations with no functional groups on

the alkyl chains. ILs that tended to follow the VTF equation tend to have small, symmetrical cations.⁵²

With high viscosity solutions there are also slow diffusion rates of electroactive solutes. Typical diffusion constants for ILs are on the order of $10^{-7} \text{ cm}^2 \text{ s}^{-1}$.⁵³ This diffusion coefficient is two orders of magnitude lower than typically displayed in organic or aqueous media.⁴³ The Stokes-Einstein equation relates diffusion to viscosity,

$$D=(kT)/(c\pi\eta r_s)$$

Equation 9: Stokes-Einstein Equation for Diffusion

Where k is Boltzmann's constant, T is temperature (K), r_s is effective hydrodynamic radius, and c is a constant. The constant is either 4 or 6. In the case of a large solute in a small solvent, c is 6. As the ratio of solute to solvent size increases or viscosity increases, then c decreases to 4.⁴⁸

An advantage to ILs is their conductivity without the need for supporting electrolyte in electrochemical studies. The typical range of conductivity for ILs is 0.1 to 20 mS cm^{-1} , with the highest coming from imidazolium family.^{43,44,54} Conductivity of ILs are considerably lower than those of concentrated aqueous solutions such as 29.4 wt% KOH solution with a conductivity of 540 mS cm^{-1} .⁴³ Conductivity is inversely proportional to viscosity, so the less viscous [TFSI] containing ILs tend to have higher conductivities.⁵⁴

Electrochemical windows of ILs are generally very wide compared to aqueous and other nonaqueous mediums. ILs have been reported to typically have electrochemical windows with a width of 4.5 to 5.0 V but windows of over 7.0 V have been reported.⁵⁵ The limits of the electrochemical window is the reduction of the cation and oxidation of the anion in the IL.^{49,55} Comparisons of electrochemical windows of various ILs in literature is difficult due to

differences in IL purity and types of counter, working, and reference electrodes.⁴³ Figure 5 is a comparison of voltammograms of a 0.1 M H₂O₄ aqueous solution in the dashed lines with pristine N-Trimethyl-butylammonium bis(trifluoromethylsulfonyl)imide ([Me₃NBu][TFSI]). There is also the comparison of platinum, gold, and glassy carbon working electrodes. Glassy carbon has the largest electrochemical window due to lack of catalytic interactions with the [Me₃NBu][TFSI] as compared to the metal.⁵⁶

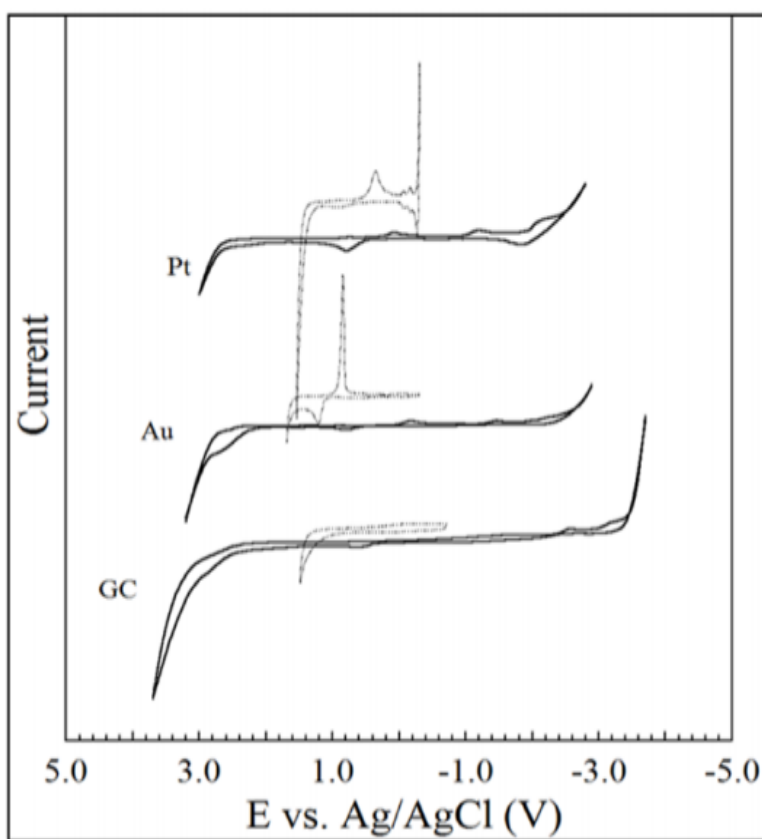


Figure 5: Comparison of electrochemical windows of [Me₃NBu][TFSI] in the solid line with 0.1 M H₂O₄ solution in the dashed lines with different working electrodes.⁵⁷

Modern ILs are typically air and moisture stable. While hydrophobic, they are often hygroscopic, resulting in water impurities in the IL from the atmosphere on the order of ~2%.^{58–60} Water impurities in ILs have been found to affect physical properties such as reducing viscosities,^{59,60} increasing conductivity, and shrink the electrochemical window.⁶⁰ There are also electrochemical interferences with the oxidation and reduction of water within a sample. Oxygen is also soluble in ILs, further interfering with electrochemical processes. Oxygen can be removed through bubbling with argon before experiments are completed.⁶¹ These water and oxygen impurities can be troubling impurities when attempting to reduce lithium and actinides to their metallic states.

1.5 Room Temperature Ionic Liquids in the Nuclear Fuel Cycle

Traditional methods for the separations of spent nuclear fuel such as SREX, CSEX, PUREX, and REDOX use volatile or semi-volatile organic compounds. These solvents and extractants introduce risk to the separation process due to their toxic and flammable natures. The non-volatile and stable nature of ILs make them ideal solvents for the processing of spent nuclear fuel.⁶² Hundreds of studies thus far have looked at solvent extraction and electrochemical separation of actinides and lanthanides utilizing ILs.^{30,46,63}

Traditional electrochemical reduction of actinides has been completed in molten salts since 1904. Uranium and thorium metals were electrochemically obtained at scale in the 1930s by the Westinghouse Electric Corporation. Potassium uranium pentafluoride or uranium tetrafluoride was dissolved in molten solutions of 80% CaCl and 20% NaCl. The 900 °C bath contained a graphite crucible anode and a molybdenum cathode with a current density of 150 A/dm². Extensive wash and drying steps were needed to remove the salts from the reduced uranium metal.⁶⁴ In the 1980s, uranium chlorides were dissolved and electrochemically and

spectroscopically examined in first generation chloro-aluminate ILs.^{65,66} Reduction and recovery of uranium metal was not successful in the first generation ILs due to their poor cathodic stability.⁶³ Electrochemical reduction of several actinides^{67,68} and lanthanides^{69,70} have been investigated with second generation ILs, primarily with the [TFSI] anion. A more thorough discussion of the electrochemical properties of actinides will be included in Chapters 4 and 5.

1.5.1 Radiolytic stability of ILs

To be used with spent nuclear fuel, ILs must have a high level of stability to radiative and thermal damage. In most processes, ILs would be replacing the TBP and kerosene mixture. This makes the TBP and kerosene the benchmark comparison for radiolysis for ILs. During spent nuclear fuel processing, ILs would be exposed to high doses of alpha, beta, and gamma radiation. In one comparative study, 1-butyl-3-methylimidazolium nitrate [BuMeIm][NO₃], 1-ethyl-3-methylimidazolium chloride [EtMeIm]Cl, and 1-hexyl-3-methylimidazolium chloride [HexMeIm]Cl were subjected to doses ranging from 2.0 to 400.0 kGy of gamma radiation. The samples were evaluated before and after by ¹H and ¹³C NMR. After irradiation there were no changes in the NMR spectroscopy, indicating a less than 1% conversion. In previous studies TBP and kerosene mixtures produced up to a 15% conversion after 400 kGy doses. Some damage was observed with UV-Vis and pH measurements, through the indication of [NO₂]⁻ anions being produced in the [BuMeIm][NO₃]. The study also concluded that radiolysis from beta and alpha radiation was minimal.⁷¹ A later study looked radiolysis of [BuMeIm][PF₆] and [BuMeIm][TFSI] at total radiation doses ranged from 100 to 600 kGy and 1200 kGy under both argon and air. The conductivity of both [BuMeIm][TFSI] and [BuMeIm][PF₆] decreased after 580 kGy of irradiation even though electrospray ionization mass spectrometry and NMR analysis did not show the presence of degradation products. It was concluded that the degradation

products were less than half of a mole percentage but was enough to increase the viscosity of the ILs, decreasing the conductivity.⁷²

1.6 Organization of Dissertation

The research performed in this dissertation explores the dissolution methods of Li_2CO_3 and UF_6 into 1-methyl-1-propylpiperidinium bis(trifluoromethylsulfonyl)imide ([MPPi][TFSI]). After dissolution, methods for the electrochemical reduction and recovery of lithium. Similarly, methods are developed for the recovery of uranium via precipitation and electrochemical reduction of UF_6 dissolved in IL.

Chapter 2 outlines methods for the dissolution for the Li_2CO_3 and UF_6 into [MPPi][TFSI]. It also presents the instruments and techniques utilized for characterization of solutions and precipitates, methods of precipitation, electrochemical reduction, and characterization of electrochemical deposits.

Chapter 3 examines and compares two different dissolution methods for Li_2CO_3 into [MPPi][TFSI] and two methods of electrochemical deposition on gold electrodes. The composition and morphology of deposits was evaluated via PXRD and SEM. Finally, deposition was examined and confirmed on several different types of carbon working electrodes.

Chapter 4 examines the dissolution of UF_6 into [MPPi][TFSI] and characterization of the species in the ionic liquid solution. The oxidation state of U is evaluated via XAFS, UV-Vis, Raman, and electrochemically to determine the mechanism and pathway for dissolution.

Chapter 5 demonstrates the recovery of uranium from the dissolved species through two precipitation methods and electrochemically. The different routes of precipitation are presented with the corresponding composition of the recovered species. These precipitates are characterized by PXRD, TGA, UV-Vis, Raman, and FT-IR. Thermal analysis and heating of

both precipitates are shown to produce uranium oxides. Electrochemical recovery of uranium is also briefly explored.

Chapter 6 provides a summary and conclusion for the overall dissertation and the discoveries made in the dissolution and recovery of Li and U species in IL.

Chapter 2. Experimental Methods

Chapter 2 presents the methods, instrumentation, and experimental of the following work. Here the dissolutions of strategic materials, Li_2CO_3 and UF_6 into $[\text{MPPi}][\text{TFSI}]$ will be presented. Followed by electrochemical techniques utilized in the experiments. Finally, instrumentation and theory of techniques used for evaluation will be described.

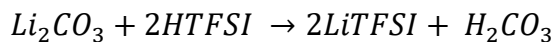
2.1 Dissolution of Critical Materials into $[\text{MPPi}][\text{TFSI}]$

2.1.1 Dissolution of Li_2CO_3 into $[\text{MPPi}][\text{TFSI}]$

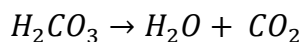
Lithium carbonate and bis(trifluoromethylsulfonyl)imide acid 99% (HTFSI) were purchased from Tokyo Chemical Industry and the 1-propyl-1-methylpiperidinium bis(trifluoromethylsulfonyl)imide 99% ($[\text{MPPi}][\text{TFSI}]$) was purchased from IoLiTec. Two methods for dissolution were explored to introduce Li_2CO_3 into the $[\text{MPPi}][\text{TFSI}]$.

2.1.1.1 Method 1

Li_2CO_3 and HTFSI with a 1:1 ratio of lithium to acid were directly added to $[\text{MPPi}][\text{TFSI}]$ in a 40 mL vial. A slight excess of Li_2CO_3 was used to minimize acid remaining in solution. The mixture was sonicated for up to 4 hours until gas evolution ceased indicating the reaction was complete. The solution was then rotary evaporated overnight at 45 mbar and 90 °C to remove any water and CO_2 produced from the dissolution of Li_2CO_3 and the formation of H_2CO_3 (Equation 10 and Equation 11).



Equation 10: Conversion of Li_2CO_3 to LiTFSI



Equation 11: Side reaction of LiTFSI production

The solution concentration was $\sim 1\text{M}$ Li ion when completed. The maximum concentration achieved from direct dissolution was $\sim 7\text{M}$. However, the viscosity increased dramatically and the solution solidified at this high concentration.

2.1.1.2 Method 2

The Li_2CO_3 was placed in an Erlenmeyer flask followed by 20 mL of $18.2\text{ M}\Omega$ water. The HTFSI was added and the solution and stirred for an hour to allow complete reaction. The solution was placed on a rotary evaporator overnight at 45 mbar and $55\text{ }^\circ\text{C}$ to remove the water added and produced during the reaction. A solid precipitate was recovered once the water was removed. The resulting LiTFSI was placed directly into [MPPi][TFSI] and sonicated to assist in dissolution. The solution was then placed on a rotary evaporator a second time to remove any trace of water. The synthesized and purchased LiTFSI were compared and used in the electrochemical recovery. There was no observed difference in voltammetric response or the deposits obtained from the synthesized and purchased LiTFSI.

2.1.2 Dissolution of UF_6 into [MPPi][TFSI]

The route for dissolution for the UF_6 is a direct addition of the solid to the RTIL, [MPPi][TFSI]. The 1-propyl-1-methylpiperidinium bis(trifluoromethylsulfonyl)imide 99% ([MPPi][TFSI]) purchased from IoLiTec. The UF_6 was natural uranium and supplied by URENCO. The UF_6 was shipped and stored in a P10 tube with a bolted top (Figure 6). All work was completed in an inert atmosphere in a VAC glovebox equipped with a cold well and cold storage assay. The P10 tube is stored in a cold storage assay at $-15\text{ }^\circ\text{C}$. Before dissolution, the P-10 tube was cooled to liquid nitrogen temperatures using the cold well. In a scintillation vial, a measured amount of room temperature [MPPi][TFSI] is added. The chilled P10 tube is opened

and the UF_6 is scooped out with a metal spatula and added directly into the $[\text{MPPi}][\text{TFSI}]$. The mass of the addition was measured by the mass changes of the vial. As the UF_6 warms, it becomes waxy and is more difficult to remove from the P10 tube. When this occurs, temporarily placing it back into the cold well to chill makes it easier to once again remove the UF_6 . The freshly made solutions are stirred with a stir bar and magnetic stir plate overnight.



Figure 6: P10 tube of UF_6 shipped from URENCO

2.2 Electrochemical methods

Electrochemical methods can be used to characterize the system or they can be used to reduce metal ions. The use of cyclic voltammetry can be used to characterize the oxidation state of metals in a solution. Metals can be reduced and recovered from solution with the use of steady-state voltammetry or differential-pulse voltammetry. These methods are discussed in the following as well as issues addressed when applying these techniques in RTILs.

An electrochemical event occurs when an electron transfer occurs between an oxidized species to a reduced species or vis versa. Both the oxidized and reduced species are stable and soluble in an electrolytic medium. In an electrochemical cell, this reaction occurs at an electrode

surface. Extending out from the electrode surface into the solution are three layers, the double layer, diffusion layer and bulk solution (Figure 7). In the case of reducing metal ions to a metallic state, the electrode provides an electron or electrons to the metal ion in solution, resulting in the deposition of the metal atom. The exchange of an electron occurs within the double layer. During reduction, the working electrode is negatively charged, resulting in the first layer of positively charged ions. Following the double layer is the diffusion layer. Here the charge distribution is not equal, with a higher concentration of positively charge ions present. Once the solution returns to electro-neutrality, the bulk solution has been reached.⁷³

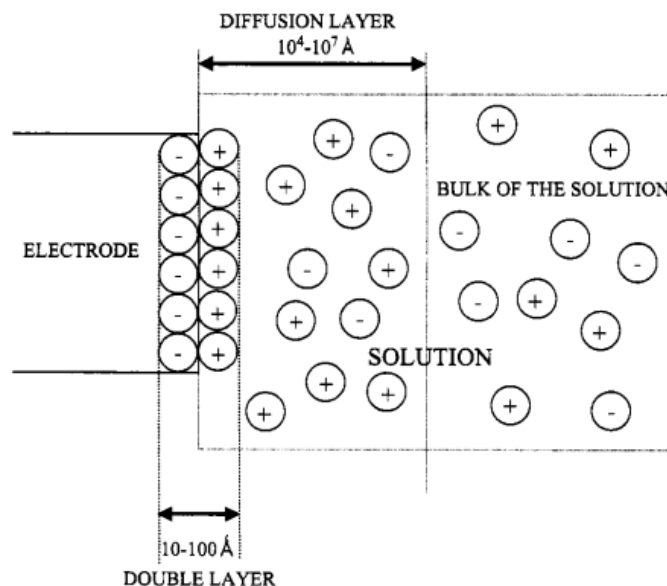


Figure 7: The electrode/solution interfaces when a negative potential is applied to the electrode.⁷³

The transfer of electrons between the electrode surface and electroactive species creates a current. This current is a measurement of the rate of reaction. Faraday's law relates moles of ions reduced, M , to the charge spent, Q , in Equation 12.

$$Q = n * F * M$$

Equation 12: Faraday's Law

F is Faraday's constant (96,485 C mol⁻¹). Current is the changes in charge over time. By taking the derivative of Faraday's law with respect to time, and normalizing for electrode surface, Equation 13 is derived.

$$i = n * F * A * \nu$$

Equation 13: Relation of current to reaction rate, ν (mol sec⁻¹ m⁻²).

Currents of chemical processes that obey Faraday's Law in Equation 13 are faradaic currents. If the current does not follow Faraday's law, it is a non-faradaic current.⁷³ In order to measure a current, multiple electrodes must be utilized in a contained system, or electrochemical cell.

In a two-electrode system there is a working electrode which facilitates the electron transfer to the analyte of interest. The counter electrode exists to maintain the electro-neutrality of the system. The difference in potential between the two electrodes is the cell potential. The cell voltage is illustrated in Figure 8. Between the electrode surface and double layer there is a sharp potential drop which are represented by the electrode potentials in Figure 8. There is additional resistance that intrinsically exists in the solution, R_s . When a current flow through the solution between the two electrodes a change in potential is experienced, which is called the ohmic drop, iR_s . This is simply derived from Ohm's Law in Equation 14.⁷³

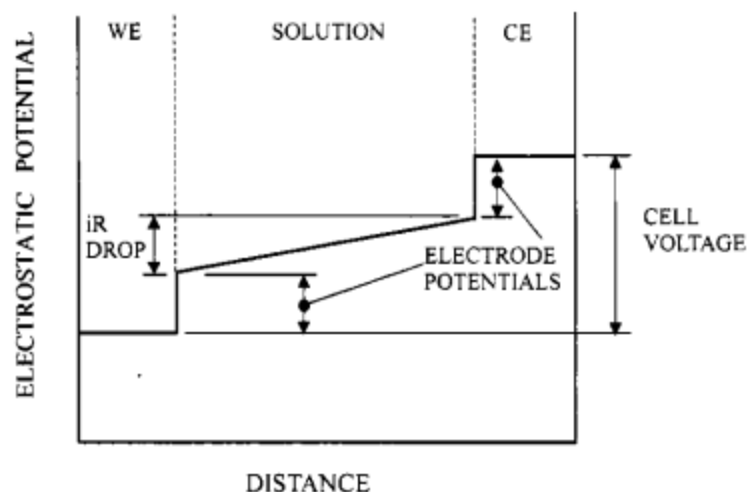


Figure 8: Potential profile of a two electrode cell between the interior of the working electrode and counter electrode.⁷³

$$V = i * R$$

Equation 14: Ohm's Law

The potential of the working electrode controls the electron transfer between the electrode and electro active species must be controlled to conduct any experiment. However, it becomes impossible to accurately control the potential of the working electrode unless the potential of the counter electrode is invariant and the ohmic drop is negligible. A half-cell system must be utilized that is unaffected by the current flow between the counter and working electrode. The components of the half-cell reaction are present in relatively high concentrations. The current therefore has a negligible effect on the concentrations of the reduced and oxidized species, maintaining a constant potential. This half-cell system is a reference electrode.⁷³

The working, counter and reference electrodes make up a three-electrode system. The counter electrode provides electro-neutrality to the system. The potential profile of the three-electrode cell is illustrated in Figure 9.

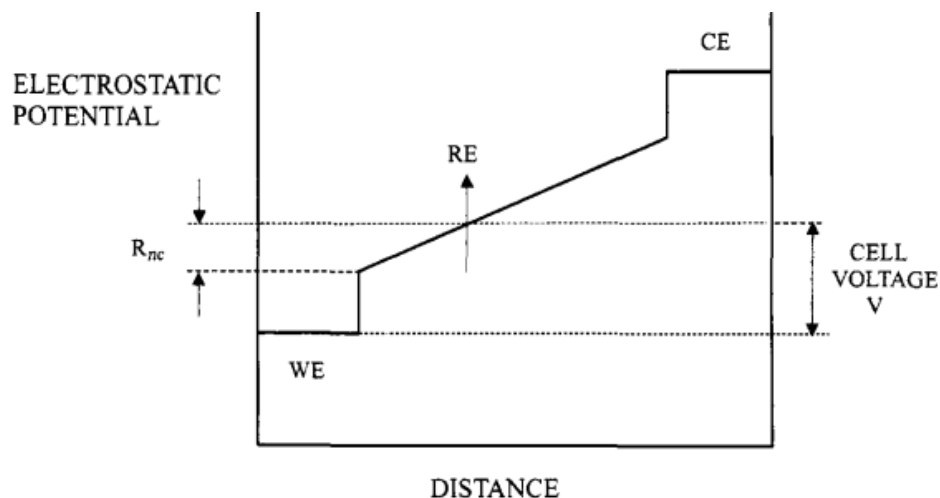


Figure 9: Potential profile in a three-electrode cell.⁷³

Unfortunately, even in a three-electrode system, the ohmic drop cannot be eliminated completely, but can be reduced by positioning the working and reference electrodes close to each other. In Figure 9, R_{nc} is the non-compensated resistance of the solution. The ohmic drop is equal to iR_{nc} . In general the ohmic drop only becomes a problem for fast electrochemical techniques in non-aqueous solvents.⁷³ General resistances of imidazolium based RTILs on a 1 mm disk electrode are in the 2.5 to 6 k Ω ⁷⁴, approximately one order of magnitude higher than conventional media such as acetonitrile/ Bu_4NBF_4 .⁴³ For most RTILs, classical equipment can compensate for these resistances as long as scan rates are below 50 V sec^{-1} .⁴³ Some RTILs such as $[\text{Me}_3\text{OctN}][\text{TFSI}]$ have resistances of 28 k Ω .⁷⁴ In these cases the ohmic drop cannot be overcome, making them less ideal for mechanistic studies.⁴³

Cyclic voltammetry is a method for studying the oxidation and/or reduction of an electroactive species in solution. During a cyclic voltammetry experiment a voltage is applied to the working electrode. An initial potential, E_i is applied to the electrode and then incrementally changed to a potential $E_{\lambda 1}$. From this potential, the scan direction is reversed and returns to E_i or some other end point, $E_{\lambda 2}$. When an electron transfer occurs between the working electrode and an electroactive species, a current is produced. This current is plotted as a function of applied potential, producing a cyclic voltammogram (CV). When the species in solution is reduced, a current, i_{pc} or peak cathodic current, is produced. The applied potential at the i_{pc} is the E_{pc} or peak cathodic potential. When scanning in the reverse and an oxidation occurs, a peak anodic current is produced at the peak anodic potential.⁷⁵

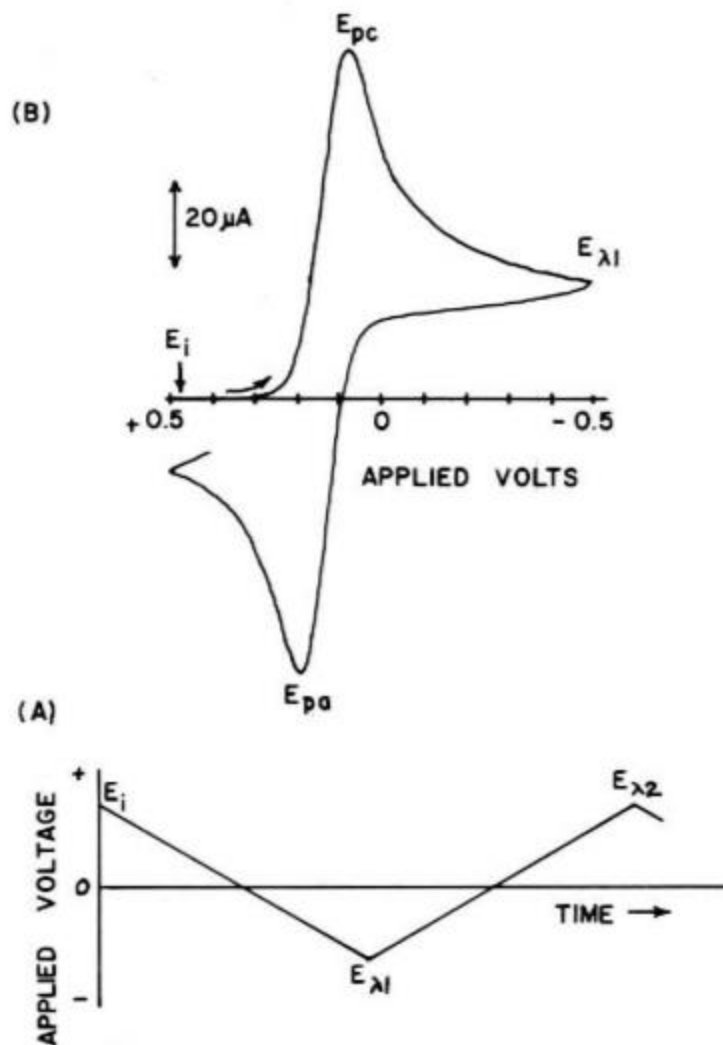


Figure 10: A) a representation of applied potential over time. B) is current as a function of applied potential applied over time.⁷⁵

From a CV, the formal reduction potential, E° , for the redox couple can be estimated by averaging E_{pc} and E_{pa} to produce $E_{1/2}$. Typically, $E_{1/2}$ is closest to E° when the electron transfer process is reversible and the diffusion coefficient for both species is the same. A system is considered fully reversible when the peak separation, ΔE_p is equal to $58/n$ mV, where n is the

number of electrons transferred.⁷⁵ When the redox couple is reversible and the electron transfer happens quickly the Nernst equation (Equation 15) in can be used to describe the cell potential.

$$E = E^{\circ} + \frac{RT}{nF} \ln \frac{a_{Ox}}{a_{Red}} = E^{\circ} + \frac{RT}{nF} \ln \frac{\gamma_{Ox}}{\gamma_{Red}} + \frac{RT}{nF} \ln \frac{[Ox]}{[Red]} = E^{\circ'} + \frac{RT}{nF} \ln \frac{[Ox]}{[Red]}$$

Equation 15: The Nernst Equation

Where R is the universal gas constant, T is temperature in Kelvin, n is number of electrons transferred, F is Faraday's constant, E° is the standard potential which takes into account the thermodynamic activity of the two species and their concentrations. The formal reduction potential, $E^{\circ'}$ encapsulates the activities of the species. Overall the Nernst equation describes how applying a potential at the working electrode will change the ratio of species in solution.^{73,75,76}

Cyclic voltammetry can also be used to investigate the diffusion rate of the electroactive species in solution. This is important for room temperature ionic liquids as diffusion is often an inhibiting factor. The Randles-Sevcik equation (Equation 16) relates peak current to scan rate, v.

$$i_p = 0.446nFAC^0 \left(\frac{nFvD_o}{RT} \right)^{1/2}$$

Equation 16: The Randles-Sevciks Equation

In the equation A (cm^2) is area of the electrode surface, D_o ($\text{cm}^2 \text{ s}^{-1}$) is diffusion coefficient, and C^0 (mol cm^{-3}) is concentration of bulk electroactive species. The Randles-Sevciks equations describes freely diffusing species of fully reversible electron transfer. When i_p is plotted as a

function of $v^{1/2}$, the trend should be linear. If the trend is not linear that would indicate the couple is either quasi-reversible or the electron transfer may be occurring via surface-absorbed species. Examining the change in peak separation can determine the cause. If the peak separation changes with scan rate, it indicates the system is quasi-reversible. If no peak-to-peak separation is observed, the non-linear species is caused by surface-absorbed species. Peak current for an electrode- absorbed species is described with Equation 17. Γ^* (mol cm⁻²) is the surface area coverage of the absorbed species.⁷⁶

$$i_p = \frac{n^2 F^2}{4RT} v A \Gamma^*$$

Equation 17: Equation relating peak current to scan-rate with an electrode absorbed species.

2.2.1 Electrochemical Cell and Reference electrode production

Non-aqueous reference electrode kits were purchased through Basi Part number MF-2062. These kits were composed of glass tubes with porous CoralPor tips with a silver wire. A silver nitrate solution was made following how it was prepared by A. Saheb, et. al. in their paper *Reference Electrode for Ionic Liquids*⁷⁷. Silver nitrate is not soluble in most ionic liquids. The AgNO₃ is initially dissolved in acetonitrile to make a 1.0 M solution. Then 50 μ L of the AgNO₃ solution was added to 450 μ L of the RTIL. The solution was then placed into the reference electrodes and they were closed. The electrodes were allowed to sit overnight to equilibrate. The reference electrodes were tested with a 2.5 mM ferrocene solution in the same RTIL. The ferrocene does not readily dissolve in an RTIL but will over the course of a day with stirring. Sonication can also be used but the ferrocene tends to precipitate over the course of a few days. A CV was run

between -0.7 V and 0.3 V to find the Fc/Fc^+ couple. From this point, all later CV's can be adjusted to any potential scale.

2.3 Instrumentation and Analytical Methods

2.3.1 Ultraviolet Visible Spectroscopy

Ultraviolet visible spectroscopy (UV-Vis) measures the transmission or absorption of radiation from about 100 to 1800 nm. Traditional UV-Vis runs in the UV range from 100 to 380 nm and the visible range to 800 nm. Beyond 800 nm is the near infrared range (NIR). The instrument used in the experiments presented in this dissertation were taken with a UV-Vis-NIR spectrometer. A single wavelength of light is passed through a compound or solution of interest. If that wavelength of light matches the excitation energy of an electron in the molecule, it can excite electrons from the highest occupied molecular orbital (HOMO) to the lowest unoccupied molecular orbital (LUMO), therefore the photon is absorbed and the transmission of light is less than 100%. When a range of wavelengths is scanned through a compound or solution, a characteristic spectrum can be obtained of the sample.

The characteristic spectra can give information on speciation, oxidation state, and functional groups. Chromophores are covalently unsaturated compounds with electronic transition energies in the UV-Vis range, responsible for giving a compound color. Covalently saturated compounds do not absorb in the UV-Vis range but can influence the absorbance of chromophores are called auxochromes. The changing of the environment of a chromophore can change the wavelength and intensity of absorbance. Environmental changes such as temperature and solvent can cause changes in the UV-Vis spectra.

UV-Vis can be used to determine concentrations. Typically the highest peak, λ_{\max} is used for concentration measurements. The Beer-Lambert law (Equation 18) describes the linear relationship between concentration and absorbance.

$$A = \log_{10} \frac{1}{T} = \log_{10} \frac{I_o}{I} = \epsilon * b * C$$

Equation 18: Beer-Lambert Law

The A is absorbance and is determined from the inverse of transmission, T, of light through the sample. Transmission is the change of intensity of light before the sample, I_o , and after the sample, I. Absorbance is proportional to the molar absorptivity of the sample, ϵ , the path length of light through the sample, b, and concentration, C. By making several standards of a sample, molar absorptivity can be calculated by the slope of the calibration curve. After making a calibration curve, an unknown concentration can be calculated from A of the same wavelength.

In a UV-Vis spectrometer two light sources are typically utilized. A tungsten lamp is used for the visible light range and a deuterium lamp is used for the UV-light range. A monochromator is used to separate the individual wavelengths. A UV-Vis spectrometer typically uses a beam splitter with two detectors. One beam goes through a sample (I) and the second beam goes through a blank without a sample (I_o). The intensities of the two beamlines are measured by a photodetector. A spectrometer that measures the NIR range (1100 to 1800 nm) will have a second detector for the longer wavelengths. The signals are sent to data processing where transmission is determined by comparing the intensity of the two beams. Software for the instrument can output either transmission or absorbance.⁷⁸

2.3.2 FT-IR

Fourier transform infrared (FT-IR) spectroscopy excites vibrational modes of molecules to produce a spectrum which can be used to for identification and structural analysis. The peaks of an FT-IR spectrum correspond with various types of chemical bonds and functional groups. Similar to UV-Vis, FT-IR can also be used to evaluate concentration based on comparison of amount of infrared energy absorbed. The FT-IR was not used for quantitative analysis in this dissertation.

As previously mentioned, FT-IR is primarily concerned with molecular vibrations in liquid and solid samples. A non-linear molecule with N atoms has a total of $3N$ degrees of freedom (DoF). Three of these DoF are the translational relative to the three axis, x , y , z . another 3 are related to the rotation of the molecule along the three axes, which can only be observed in the gas phase. So $3N-6$ DoF correspond to vibrational modes, describing bond stretching and bending. There can be symmetric and asymmetric stretching in a molecule and four types of bending, rocking, scissoring, wagging, and twisting (Figure 11). Because linear molecules cannot rotate along their single axis, they have $3N-5$ DoF.

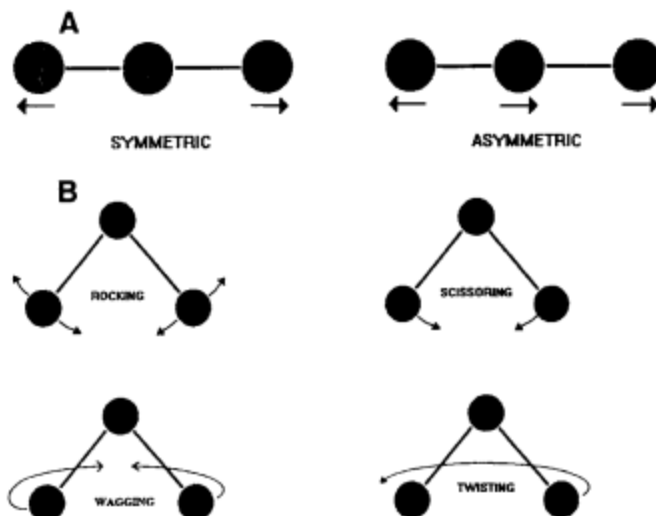


Figure 11: Types of stretching (A) and bending (B)⁷⁹

Not all vibrational modes are IR-active vibrations. To produce an infrared absorption band, the excitation of the vibration must result in a change in the dipole moment. So homonuclear diatomic molecules cannot be detected by FT-IR spectroscopy. Similarly, the symmetric stretching of a symmetric linear molecule such as CO_2 is not IR-active.

Historically, infrared spectroscopy was dispersive IR, functioning similar to how the UV-Vis works by scanning through multiple wavelengths and comparison of I/I_0 . In the 1970's FT-IR was developed. Modern day FT-IR utilizes a Michelson interferometer (Figure 12). The interferometer consists of a beam splitter with a fixed and moving mirror. The beam is split and hits both mirrors before being reflected back onto each other, forming constructive/deconstructive interference patterns. The beam then travels through the sample, where certain wavelengths are selectively absorbed, and into the detector.

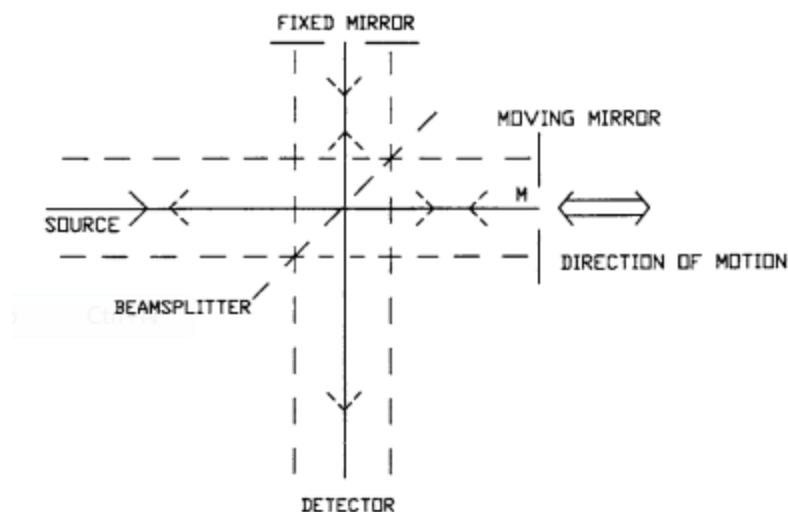


Figure 12: Schematic diagram of a Michelson interferometer.⁷⁹

The fluctuations in intensities of the beam at the detector give rise to an interferogram in the time domain. The Fourier transformation is completed on the data to convert the data into the frequency domain. Typically, the interferogram is plotted as intensity as a function of the path distance between the two mirrors. After the computer completes the Fourier transformation, the data is shown as intensity as a function of frequency in cm^{-1} . FT-IR is advantageous to dispersive IR with decreased signal to noise ratio and the ability to collect a range of wavelengths very quickly.

2.3.3 Raman Spectroscopy

Raman spectroscopy is completed by first irradiation a sample with a powerful visible or near-IR laser source. While the laser is focused on the sample, scattered radiation perpendicular to the laser source is measured. The laser used for excitation has energy $h\nu_{\text{ex}}$. The energy of the molecule goes to a virtual state and then deexcites, emitting a photon. If the emitted photon is the same energy as $h\nu_{\text{ex}}$ then Rayleigh scattering occurred. If the molecule deexcites to a higher

vibrational energy state, then the emitted photon is a lower energy or Stokes scattering. If the excited molecule started in an excited energy state when it was hit by the laser and then deexcites from the virtual level to the ground or a lower energy vibrational state, then an anti-Stokes scattering occurred. The difference in energy from the Stokes or anti-Stokes scattering from the Rayleigh scattering is plotted as the Raman shift from 0 cm^{-1} which is Rayleigh scattering. A visual example of these energy changes and the Raman shifts are shown in Figure 13. As shown in the figure, the intensities of the Stokes scattering are typically larger than the anti-Stokes since most molecules are likely to start in the ground energy state. At elevated temperatures these intensities equilibrate. However, if fluorescence is an issue in a sample, it is beneficial to measure the anti-Stokes scattering instead of the Stokes because the Stokes will be drowned out by fluorescence.

Raman spectroscopy is similar to FT-IR in which both methods measure excitation in the vibrational modes. However not all IR-active modes, as described in the previous section, are Raman-active. IR-active modes involve a change in dipole moment but Raman-active modes involves the polarizability of a molecule or a change in charge distribution with the excitation of a molecule.

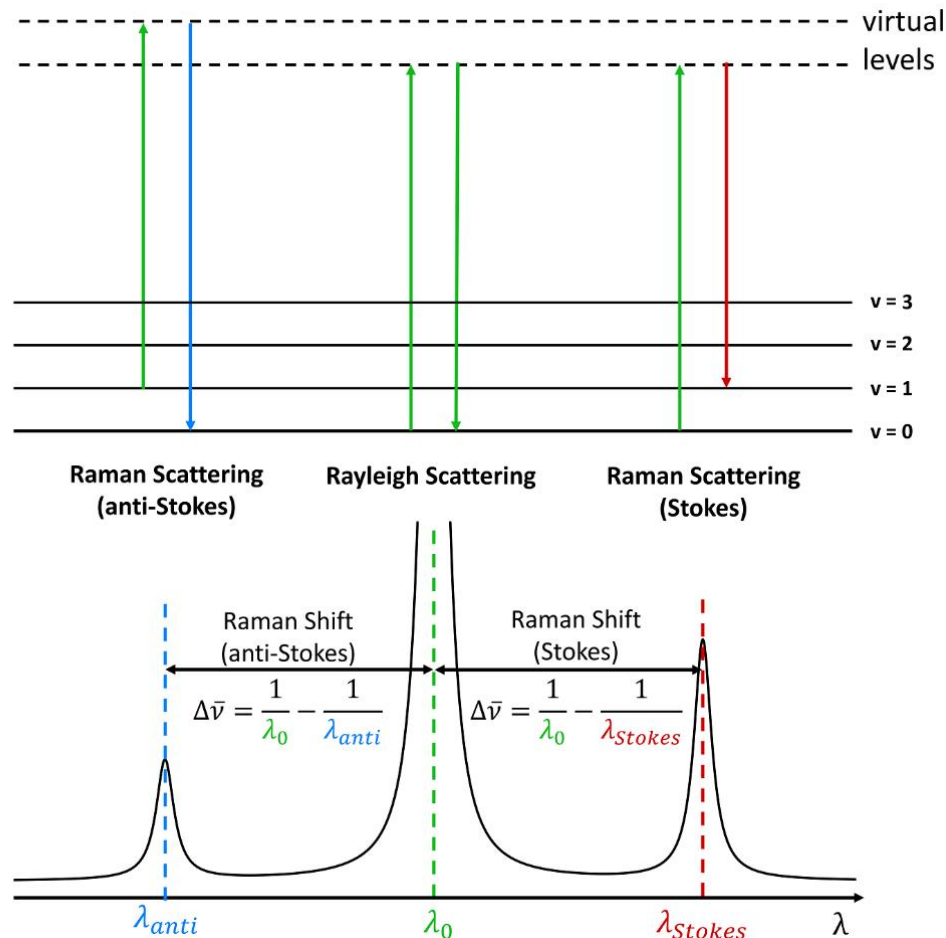


Figure 13: Schematic of Rayleigh, Stokes, and anti-Stokes scattering and how they are plotted in Raman spectroscopy.⁸⁰

The instrumentation involved in Raman spectroscopy is rather simple. The high-intensity laser is focused into a sample with several sets of mirrors. Perpendicular to the sample is the wavelength selector. The wavelength selector must be perpendicular to the sample to minimize the radiation from the laser. The purpose of the wavelength selector is to narrow the range of wavelengths examined. This is important to being able to find the weak Raman scattering lines compared to the Rayleigh Scattering. These wavelength selectors were historically

monochromators but have recently been upgraded to photodiode arrays. The signal then typically go through some sort of amplification process and then into computer processing to an output.⁸¹

2.3.4 Inductively Coupled Plasma- Atomic Emission Spectroscopy

Inductively coupled plasma- atomic emission spectrometry (ICP-AES) is a well-established technique able to detect trace-elements down to a few parts per million and some instruments to parts per billion and able to detect several different elements almost simultaneously. ICP-AES is a destructive technique, often requiring dilution of samples to an appropriate concentration of the element(s) of interest.

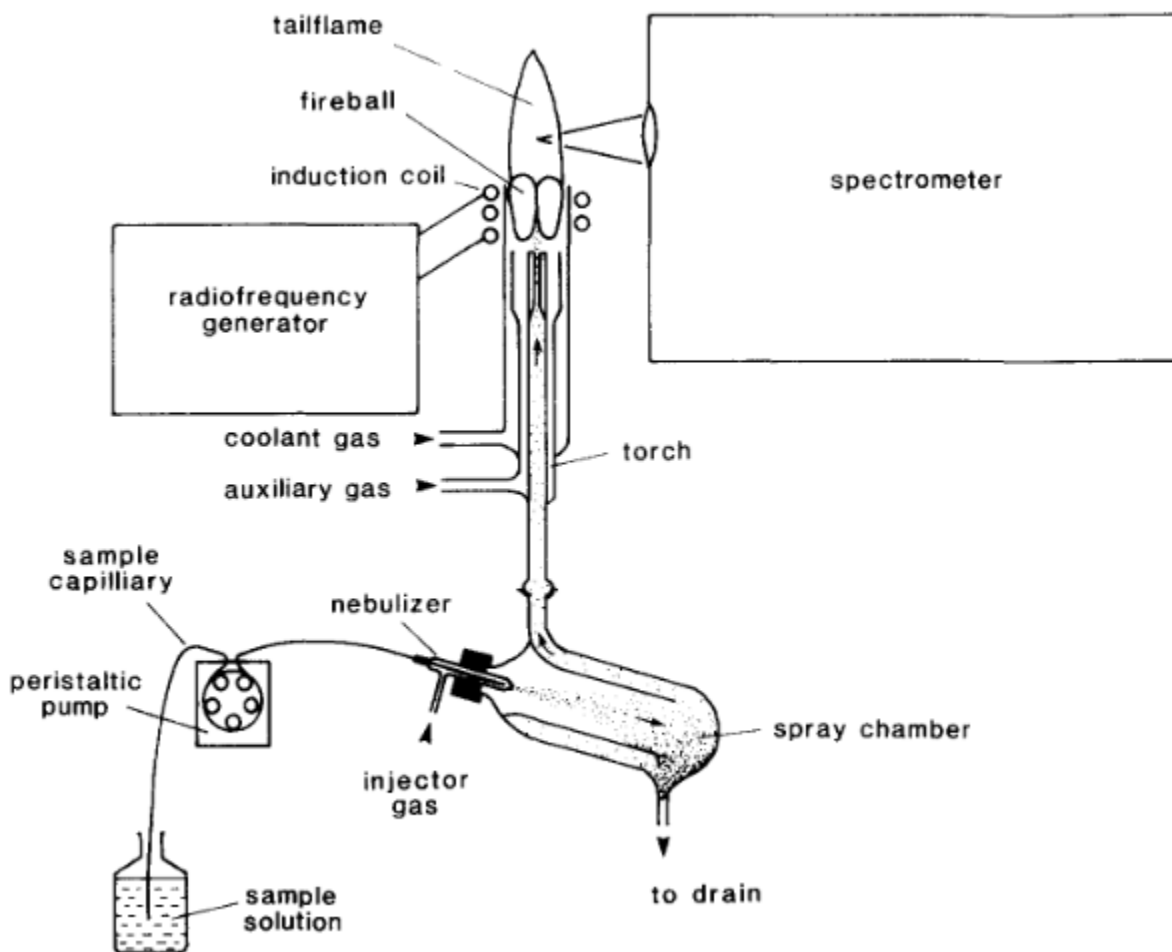


Figure 14: Schematic of an ICP-AES⁸²

The ICP portion of the instrument produces an argon plasma. A stream of argon at the end of a quartz tube is wrapped with cylindrical induction coils. The coils produce a radiofrequency magnetic field, causing the ignition of the argon plasma. Samples are diluted with solutions of 1 to 5% HNO_3 . The solutions are fed into a nebulizer where they are aspirated. An auxiliary argon gas stream delivers the aerosolized sample to the argon plasma. The argon plasma is temperatures as high as 10,000 K. Here the sample is vaporized to individualized atoms.

The AES portion of the instrument refers to the detection part of the instrument. In the plasma, the outer electrons of the elements of interest are excited to higher energy states. When they deexcite, a photon is emitted. Each element has a unique emission profile, dependent on the quantized energy levels of their electrons. The photons are ejected from the plasma and measured by a photodiode and read out by a computer. The number of photons emitted is proportional to the concentration of the element of interest in the sample. The detector is often set to measure certain wavelengths of interest for each sample to speed up data collection.⁸²

2.3.5 X-Ray Absorption Fine Structure Spectroscopy

X-Ray Absorption Fine Structure (XAFS) Spectroscopy utilizes the absorption of X-rays by matter through the photoelectric effect. Absorbance of the x-ray are measured as an inner shell electron to a higher energy state. This work utilized the U- L_3 edge at 17.166 keV. The absorbance of the incident x-rays is measured starting at 16.97 keV to 18.4 keV. The XAFS data then gives rise to two regions of interest, X-Ray Absorption Near Edge Structure (XANES) and Extended X-Ray Absorption Fine Structure (EXAFS). The two regions give different information about the atom of interest and the environment it is found in. An example of these

plots is shown in Figure 15. The XANES region can be used to compare a sample to standards to get an idea of the oxidation state of the atom of interest. In the EXAFS range the outgoing wavefunction is affected by the backscattering off neighboring atoms. So, the EXAFS oscillatory pattern is a presentation of the interferogram of the atoms arranged around the atom of interest, in this case uranium. This information can be fitted to determine the identity of distance of the surrounding atoms.⁸³

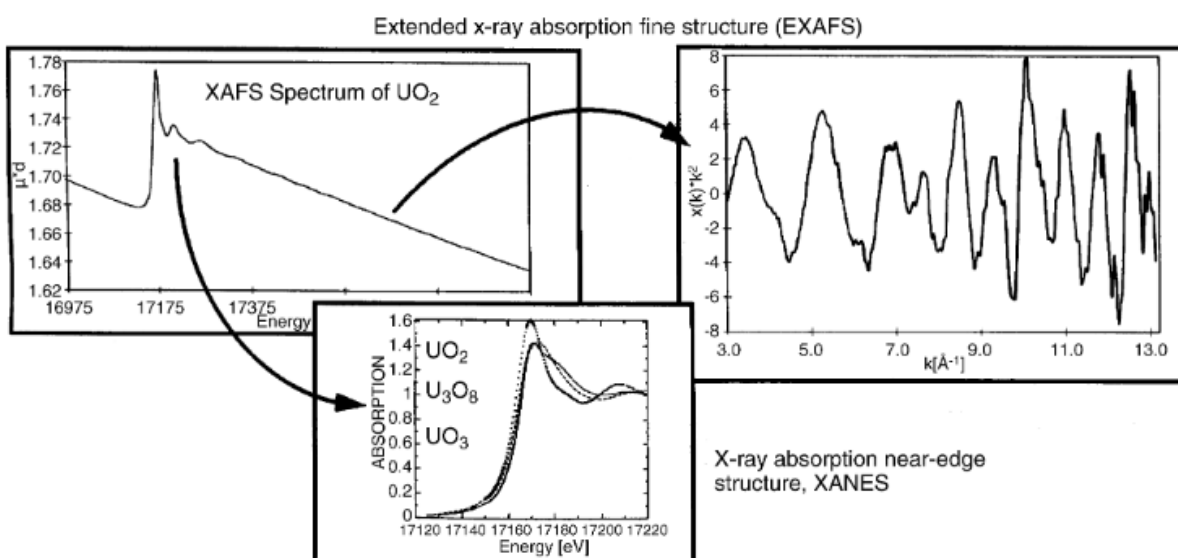


Figure 15: Example readouts of raw XAFS, background subtracted XANES, and k^3 -weighted EXAFS data.⁸³

The XAFS measurements were performed at the Advanced Photon Source at the BESSRC-CAT 12 BM station at Argonne National Laboratory. The U samples (solid and solution) were placed in an aluminum sample holder equipped with Kapton windows. These are shown in Figure 16. These holders were then placed in a secondary containment system shown in Figure 17 to ensure no leakage of radioactive materials.



Figure 16: Radioactive solution sample holder on the left and a solid sample holder on the right.

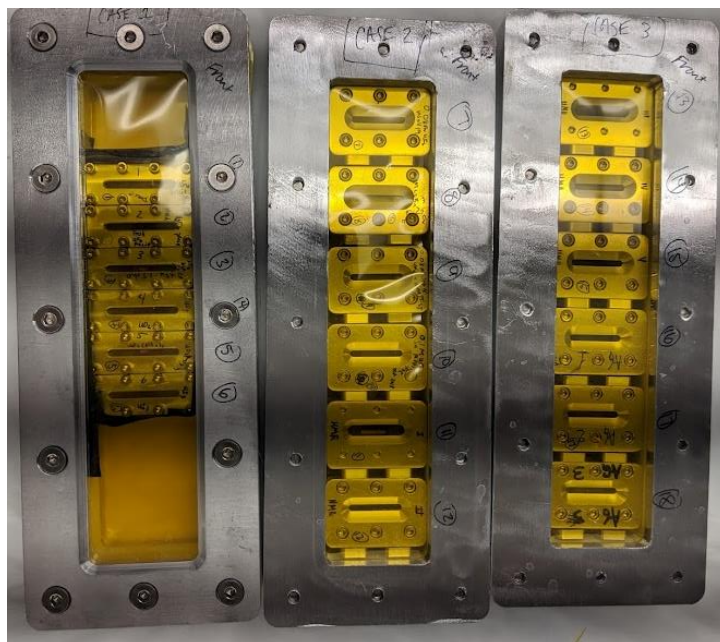


Figure 17: Secondary containment sample holders for liquid and solid samples.

2.3.6 Scanning Electron Microscopy and Energy Dispersive X-ray Spectroscopy

Scanning electron microscopy (SEM) provides the ability to examine the microstructure morphology of the surface of a solid sample. An SEM consists of an electron gun which shoots electrons at the surface of the sample. The electron interacts with the surface of the sample by either elastic or inelastic scattering. In elastic scattering the electrons are deflected by the specimen atomic nucleus or outer shell electrons with negligible energy loss. If the scattering occurs at an angle greater than 90° , they are called backscattered electrons and can be used for one type of imaging. Inelastic scattering occurs when incident electrons cause ionization of the specimen and ejection of electrons. These electrons are called secondary electrons and have energies less than 50 eV. Secondary electrons can be used to image or analyze the sample. The JEOL-5610 SEM used in this work was equipped with both secondary and backscatter electron detectors.

Secondary electrons can resolve surface structures down to 10 nm, providing a visualization of surface texture and roughness. Secondary electrons that are unable to make it to the detector cast a shadow on the image of the surface while more prominent feature appear brighter. The number of backscattered electrons is much larger than that of secondary electrons, resulting in less surface resolution than secondary electrons (approximately $1\ \mu\text{m}$). However, because of their higher energy they carry information about the features below the surface of the sample.⁸⁴

Coupled with the SEM is an energy-dispersive x-ray spectroscopy detector. This allows for chemical mapping simultaneously with the imaging from the SEM. The electron beam used in SEM simultaneously ejects an inner shell electron creating an electron hole. When an outer shell electron drops down to the electron hole to fill it an x-ray of the energy difference is

released. The energy of the x-ray is characteristic to the energy levels of specific elements. The x-rays hit a Si(Li) detector and produce a signal. The number of x-rays of specific energies correlates to the concentration of one element compared to other elements in the sample to create ratios.⁸⁵

2.3.7 Powder X-Ray Diffraction

Powder X-Ray Diffraction (PXRD) is utilized for qualitative identification of crystalline solids and does not require a perfect crystal. A sample is ground further to produce a homogenous powder and loaded onto a low background Si sample holder. The powders are spread onto the surface thinly, often with the aid of an alcohol that is evaporated off. Radioactive and air sensitive samples were capped with a dome to reduce the spread of materials. The sample holder is placed onto a stage in the Bruker D8 Advance powder X-ray diffractometer and spun continuously. A primary X-ray beam (in this work from a Ni-filtered Cu K α (1.54059 Å)) comes out of the x-ray tube and hits the sample. Incident x-rays are diffracted and are detected by a silicon strip detector (Lynxeye). A schematic of a PXRD system is shown in Figure 18.

Both the detector and sample stage change angles over time with an incident angle of 2θ . The instrument measures the number of diffracted x-rays as number of counts as a function of 2θ . The angles of the diffracted x-rays are dependent on the spacing between atom as described by Bragg's Law (Equation 19). The variables are the lattice interplanar spacing, d , the incident angle, θ , an integer, n , and the wavelength of the characteristic x-ray, λ . Two incident wavelengths are in-phase they result in constructive interference or more counts at that angle, which can be used to calculate the distances between the two atoms.⁸¹

$$2d(\sin \theta) = n\lambda$$

Equation 19: Bragg's Law

The patterns collected in this work were analyzed initially in the software package EVA v15 made for Bruker-AXS. EVA was used to compare the experimental patterns to patterns available in the Inorganic Crystal Structure Database to identify compounds found in the sample. The data was then fit in the Bruker TOPAS 4.2 software using Rietveld structure refinement on CIF files of known compounds.

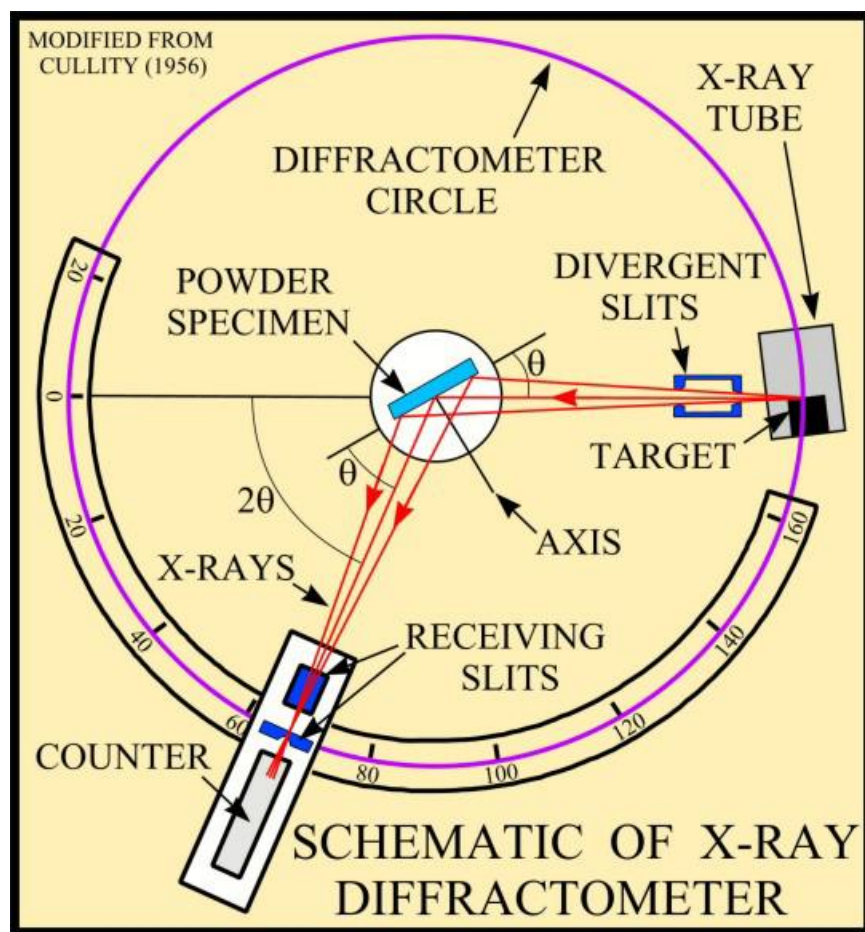


Figure 18: Schematic of PXRD Instrumentation⁸¹

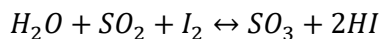
2.3.8 Thermal Gravimetric Analysis

Thermal gravimetric analysis (TGA) is a destructive method that is completed by heating up a sample to a certain temperature and observing the change in mass. There instrument is

comprised of a high precision balance that can measure masses down to the microgram. Sample masses of about 20 to 30 mg are loaded into a Al_2O_3 .

2.3.9 Karl-Fisher Titration

Water content of organic solutions can be determined with a Karl Fischer titration. The chemical reaction that occurs during a Karl Fischer titration is the reaction of SO_2 and I_2 with water as shown in Equation 20. Iodine is added to solution to excess, indicating the endpoint of the titration. The amount of iodine added is a 1:1 molar ratio to water.



Equation 20: Chemical Reaction utilized in a Karl Fischer Titration

In modern day, the Karl Fischer Titration is completed by specialized titrators. In this work a Mettler Toledo Karl Fischer DL32 Titrator was utilized to perform this titration. The titrator completes a coulometric titration to determine the water concentration and can resolve down to 50 ppm of water. A schematic of the titration cell is shown in Figure 19. The reactions that occur in a coulometric Karl Fischer titration differs from the historical titration. Two different solutions are used within the titrator, the catholyte and anolyte. These are commercially available and composition depends on the types of samples that will be measured for water content. In the main anode chamber contains an anolyte composed of sulfur dioxide, imidazole, and iodide. The reactions shown in Equation 21.

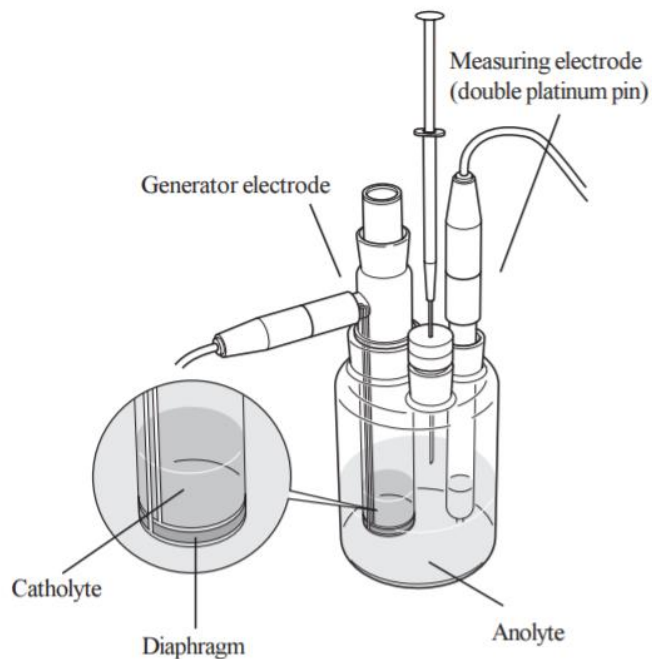
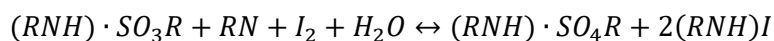
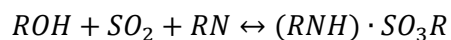


Figure 19: Schematic of the Mettler Toledo D-32 Karl Fischer Titrator⁸⁶



Equation 21: Chemical reactions with the anolyte and water.

After the chemical reaction occurs the iodide ions is oxidized to iodine at the anode. The catholyte contains an ammonium salt which is reduced at the cathode while the iodine is oxidized. A current is required to produce the sulfate and iodine. This current is equivalent to the amount of water that was present in the initial sample so 1 mg of water corresponds to 10.72 C.⁸⁶

Chapter 3. Dissolution and Recovery of Lithium from IL

In this chapter the dissolution of Li_2CO_3 into $[\text{MPPi}][\text{TFSI}]$ was explored through two methods. Both utilized the HTFSI acid to dissolve the Li^+ into the IL. The reaction was completed either before in an aqueous solution or concurrently into the IL. After dissolution into the $[\text{MPPi}][\text{TFSI}]$, two methods for electrochemical recovery of the lithium were evaluated.

Both methods began by performing a 20-cycle cyclic voltammetry (CV) scan from 3.2 to -4.0 V. This promotes the formation of nucleation sites. After the CV, two differing methods for deposition were utilized. The first was traditional steady state deposition at -4 V. The second used a differential pulse deposition method at -4 V for 5 seconds and then 1 V for 0.5 seconds. The differential pulse method produced deposits that better adhered to the electrode and were less dendritic. Both methods produced metallic colored deposits that appeared to be LiH with PXRD analysis. Deposition was successful on gold sheet electrodes as well as several different carbon electrodes.

3.1 Introduction

The nonflammable and nonreactive nature of ILs reduces the risk of thermal decomposition or combustion in LIBs compared to traditional carbonate electrolytes.⁸⁷ Initially, the 1-ethyl-3-methylimidazolium cation ($[\text{EMIm}]$) was studied extensively for its reduced viscosity relative to other ILs.⁸⁸ However, the cathodic limit of the $[\text{EMIm}]$ cation was not sufficient for the highly negative reduction potential of lithium. The standard reduction potential of Li is -3.0401 V vs SHE.⁸⁹ Studies focused next on quaternary ammonium-imide salts showing that lithium could be deposited and stripped.⁹⁰ From a cathodic stability standpoint, the quaternary ammonium cations fared better than their aromatic counterparts. The six-membered ring of the 1-methyl-1-propylpiperidinium ($[\text{MPPi}]$) cation was resistant to reduction as well as

achieving a higher coulombic efficiency than other quaternary ammonium ions.⁹¹ The [TFSI] anion has been selected primarily for its high conductivity, low melting point, and low viscosity.^{61,92}

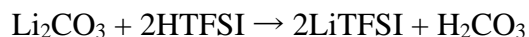
New methods for recycling lithium from traditional LIBs utilize ILs for selective extraction of Li from aqueous mixtures. The spent LIB cathode ($\text{LiNi}_{0.5}\text{Mn}_{0.3}\text{Co}_{0.2}\text{O}_2$) was dissolved in sulfuric acid with a pH of 3. With an organic phase of 80% TBP and 20% carboxymethyl trimethylammonium bis(trifluoromethyl)sulfonimide), 96.8% of Li was extracted after 5 stage extractions with only 7.0%, 4.2% and 13.6% of the Ni, Co, and Mn respectively extracted. The lithium was recovered from the organic phase using a mixture of 0.5 M H_2SO_4 and 0.5 M Li_2SO_4 with a 99.6% recovery rate.⁹³

In contrast, next generation LIBs are looking at utilizing ILs as a solvent instead of traditional carbonate-based solvents. ILs have been examined in an attempt to overcome or minimize dendritic formations during lithium ion cycling in batteries.⁹⁴ Two formations of dendritic deposits have been observed during the lithium cycling, singular needle like structures and 3D bush structures.⁹⁵ ILs have been shown to be able to provide a solid electrolyte interface (SEI) comparably to carbonate based solutions. The SEI is important to protecting the cathode from damage throughout the cycling of a battery's lifetime.⁹⁶

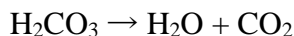
Many studies have examined the efficiencies of using various ILs and electrodes for LIBs. However, studies examining the reduction/deposition of lithium based on the ILs inherent negative potential limit have been largely overshadowed by the focus of reducing dendritic loss of efficiency in LIBs. Recovery of Li metal from Li_2O has been exhibited in 2:1 molar ratios of ethylene carbonate and chloroaluminate (EC): AlCl_3 . Typically, metal oxides are insoluble in ionic liquids, but in a chloroaluminate solution, it's suspected at elevated temperatures AlCl_2^+

cation acts as a Lewis Acid to dissolve the Li_2O readily. Because of the EC backbone of the ionic liquid, the solution can withstand the applied voltage required for reduction of lithium metal. At -3.1 V (vs Al) Li metal was deposited on a high purity Al sheet.⁹⁷

The oxidation/reduction of lithium in various ionic liquids has been previously studied in systems containing the [TFSI] anion.^{91,98–101} While these studies have examined lithium oxidation/reduction using cyclic voltammetry, they have not focused on the dissolution and electrochemical recovery. This chapter focuses on the direct dissolution of Li_2CO_3 into IL and the electrochemical recovery and characterization of the deposits. The process utilizes the carbonate derivative for the dissolution and subsequent electrochemical reduction of lithium. However, LiOH can also be utilized in the process through similar dissolution methods. The IL, 1-methyl-1-propylpiperidinium bis(trifluoromethylsulfonyl)imide ([MPPi][TFSI]) was selected for this study based on the electrochemical stability; the [MPPi] cation is resistant to reduction before -3.8 V vs Ag/AgCl with a glassy carbon working electrode.⁹¹ The [TFSI] anion was selected for its previous success in the literature¹⁰² as well as the availability of the acidic form, HTFSI. The goal was to overcome the primary obstacle of low metal solubility in the ionic liquid using the acidic functionality.¹⁰³ The acidic version of the [TFSI] anion has been used to dissolve the Li_2CO_3 into [MPPi][TFSI]. Li_2CO_3 was selected due to being the current chemical form for Li from recycled traditional LIBs. The basic equation of conversion to LiTFSI is shown in Equation 22 followed by the secondary reaction in Equation 23 to produce water and carbon dioxide.



Equation 22: Synthesis of LiTFSI from Li_2CO_3



Equation 23: Evolution of carbon dioxide

This dissolution of Li can be achieved in the [MPPi][TFSI] through direct dissolution of Li_2CO_3 or through the dissolution of LiTFSI produced from an aqueous reaction, recovered, and then dissolved in ionic liquid through a secondary reaction. The electrochemical recovery of Li was examined on a gold foil and several carbon-based working electrodes after dissolution into the [MPPi][TFSI]. The recovered materials were examined using powder X-ray diffraction and SEM imaging. This work recognizes the use of ILs as solvents in LIBs and establishes the potential use of ionic liquid solutions in the recovery of lithium as they reach end of life. This chapter specifically provides pathways for the dissolution and recovery of Li that when optimized may help reduce the reliance on mining/processing of lithium ores.

3.2 Methods and Materials

3.2.1 Chemicals and Solutions

Lithium carbonate and bis(trifluoromethylsulfonyl)imide acid 99% (HTFSI) were purchased from Tokyo Chemical Industry. The 1-propyl-1-methylpiperidinium bis(trifluoromethylsulfonyl)imide 99% ([MPPi][TFSI]) was purchased from IoLiTec. Two methods for dissolution were explored to introduce Li_2CO_3 into the [MPPi][TFSI].

3.2.2 Dissolution of Lithium

3.2.2.1 Method 1

Li_2CO_3 and HTFSI with a 1:1 ratio of lithium to acid were directly added to [MPPi][TFSI] in a 40 mL vial. A slight excess of Li_2CO_3 was used to minimize acid remaining in solution. The mixture was sonicated for up to 4 hours until gas evolution ceased indicating the

reaction was complete. The solution was then rotary evaporated overnight at 45 mbar and 90 °C to remove CO₂ and most of the water produced from the dissolution of Li₂CO₃ and the formation of H₂CO₃. The solution concentration was ~ 1M Li ion when completed. The maximum concentration achieved from direct dissolution was ~7M. However, the viscosity increased dramatically and the solution solidified at this high concentration.

3.2.2.2 Method 2

The Li₂CO₃ was placed in an Erlenmeyer flask followed by 20 mL of 18.2 MΩ water. The HTFSI was added and the solution and stirred for an hour to allow complete reaction. The solution was placed on a rotary evaporator overnight at 45 mbar and 55 °C to remove the solvent water and the additional water produced in the reaction. A solid precipitate was recovered once the water was removed. The resulting LiTFSI was placed directly into [MPPi][TFSI] and sonicated to assist in dissolution. The solution was then rotovapped a second time to remove water to a low level. The synthesized and purchased LiTFSI were compared and used in the electrochemical recovery. There was no observed difference in voltammetric response or the deposits obtained from the LiTFSI produced by the two methods.

3.2.3 Electrochemical Methods for Deposition

A non-aqueous reference electrode was constructed using a BASi (Part number MF-2062) kit. The Ag wire electrode was combined with an internal silver nitrate solution prepared as described by A. Saheb, et. Al.⁷⁷ For the experiments, 4 mL of 0.5 M LiTFSI in [MPPi][TFSI] were added to an electrochemical cell. The counter electrode was a platinum sheet. The working electrode was gold. The CH Instruments Inc 600 series potentiostat with the corresponding CHI software were used for all deposition studies. Studies were completed in a glovebox with an argon atmosphere. The gold disc electrode used for cyclic voltammetry was 1.6 mm diameter

(Part number MF-2014) purchased from BASi. The gold foil used for bulk deposition was 0.025mm thick 99.95% gold purchased from Alfa Aesar. A glassy carbon disc electrode (Part number MF-2012) with a 3.0 mm diameter was used for the cyclic voltammetry data as well. The carbon-based electrodes used for deposition were screen printed single working electrodes from CH Instruments (part number SE 100), 0.10 mm thick vitreous carbon foil from Goodfellow, and carbon fiber electrodes purchased from Carolina (Item number 211020).

Cyclic voltammetry (CV) was conducted before any deposition/recovery methods were initiated. The electrode was cycled twenty times from 3.2 V to -4.0 V at a scan rate of 0.1 V/sec. Following the twenty cycles using CV the deposition/recovery process using steady-state and differential pulse methods was conducted. The steady-state deposition was conducted without stirring at a set potential for a given period of time. The typical deposition was conducted at a potential of -4 V for 20 hours. In comparison, the differential pulse method was also used for the deposition. For this technique the typical parameters utilized were $E_i = 0$ V, and $E_1 = -4$ V with the time spent at E_1 set to 5 seconds. The pulse E_2 was set at 1 V for 0.5 seconds. The number of cycles was set to 13091 to be equivalent to 20 hours of run time. All voltages listed in the experimental are those entered into the CHI software and not corrected with a ferrocene standard. The potentials reported in the results and discussion are reported vs Ag/AgCl sat'd KCl based on the measurement of a ferrocene standard in the same IL with the same reference electrode.

3.2.4 Analysis Instrumentation

The SEM images of the lithium deposits were taken on a JEOL JSM6700F Field Emission SEM instrument without any additional surface pretreatment. The magnification range of 35 to 1200 times was used. The imaging conditions used a 15 kV accelerating voltage and a working

distance of 22 mm. The gold electrode with deposits was dipped in acetone before being placed on the stage to remove the [MPPi][TFSI] from the electrode surface. The PXRD patterns were collected using a Bruker D8 Advance powder x-ray diffractometer. The lithium deposits were placed on a silicon low background stage.

3.3 Dissolution and Electrochemical Response of Lithium in IL

Both dissolution methods provided sufficient Li^+ concentrations in IL such that visible deposits of LiH on Au electrodes were observed. The cyclic voltammetry for both methods for the direct dissolution of Li_2CO_3 and LiTFSI were identical indicating that Li^+ is the relevant species in the IL. However, the dissolution LiTFSI typically produced a system with less water or acid thereby reducing the impact of oxide formation at the Au electrode and hydrogen evolution during the deposition of Li. However, all samples had residual water between 200 to 450 ppm as measured by Karl-Fisher titration. The direct dissolution of Li_2CO_3 using HTFSI was more likely to produce visible hydrogen evolution at the working electrode from the excess acid and water remaining in the [MPPi][TFSI] solution. Excess Li_2CO_3 could be added to the [MPPi][TFSI] to reduce the acid in solution or alternative additional methods to reduce the acid and water in the IL can be utilized. However, the optimization of the processes was not considered in the scope of this chapter. The focus was on developing pathways for the dissolution and recovery of Li from Li_2CO_3 starting materials common in LIB recycling.

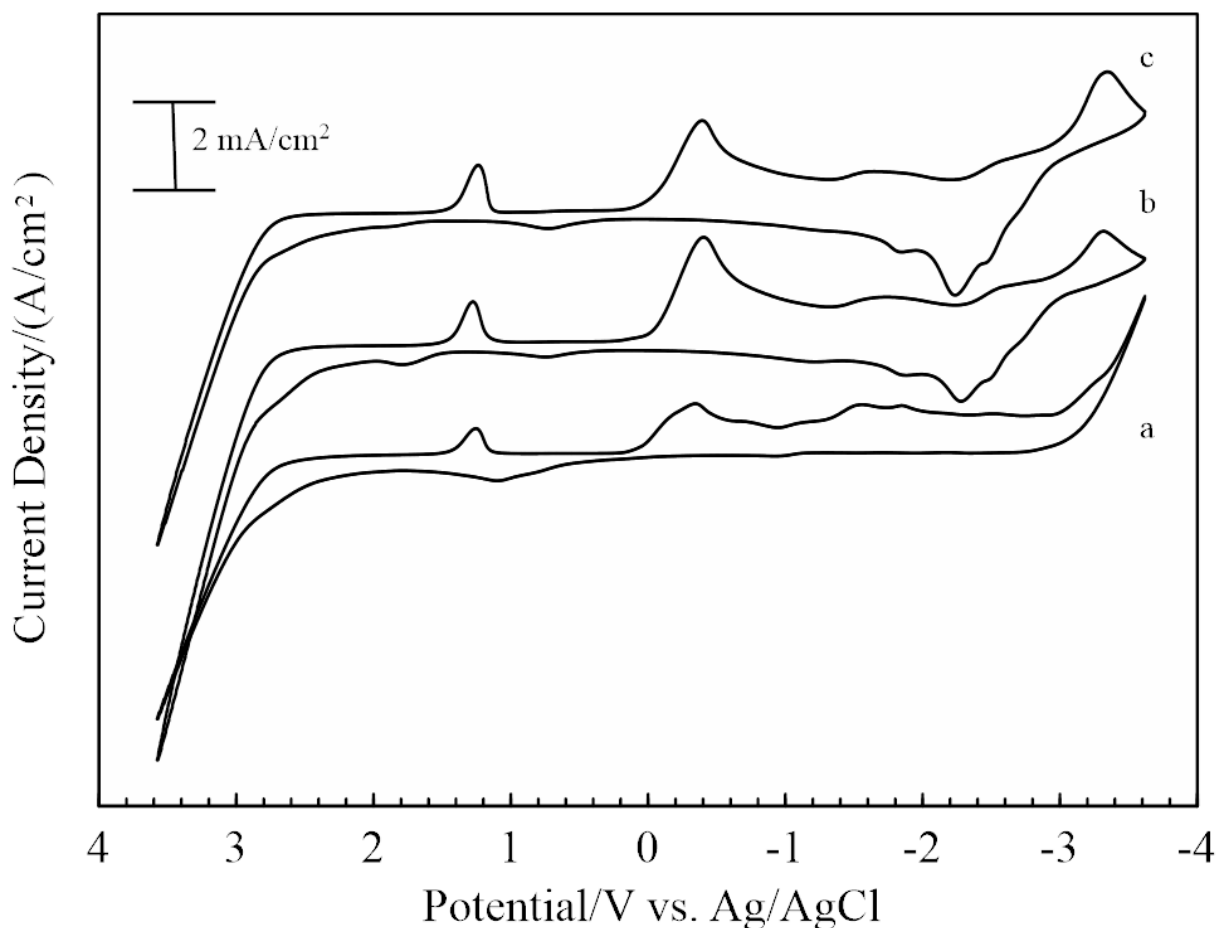


Figure 20: Cyclic voltammetric response of an Au electrode in a. IL without Li. b. 0.5 M LiTFSI. and c. 0.7 M Li₂CO₃ dissolved directly into IL. The scan rate was 0.1 V/s.

The full CVs for an Au disc electrode in [MPPi][TFSI], and IL containing dissolved Li are provided in Figure 20. All CVs were collected using the same gold disc electrode that was polished between experiments. The electrochemical response for both Li samples obtained from both dissolution methods have the same electrochemical features in comparison to the background of [MPPi][TFSI]. For samples containing Li⁺, the reduction is initiated at -2.37 V, reaching a peak maximum at -3.33 V vs Ag/AgCl. The reverse scan results in the oxidation of Li from the electrode surface reaching a maximum at -2.25 V vs Ag/AgCl. The presence of residual

water is also apparent in the cyclic voltammetry despite using the rotary evaporator. Specifically, the reduction of gold oxide is observed in all three solutions at +1.25 V vs Ag/AgCl consistent with Equation 24¹⁰⁴. The oxidation/reduction of gold oxide involves both residual water and proton species in the IL. Thus, hydrogen evolution occurs at -0.39 V vs Ag/AgCl consistent with Equation 25⁸⁹.



Equation 24: Oxidation of Gold



Equation 25: Hydrogen Evolution

The reductive deposition of Li onto the electrode occurs at potentials more negative than -3.2 V vs Ag/AgCl. The CVs of the two methods for dissolution show either method is viable for producing LiTFSI that readily dissolves in the IL.

After the deposition of lithium on gold electrodes, deposition was completed on several carbon-based electrodes. In Figure 21 are the CVs of the same solution as in Figure 20 but with a glassy carbon disc electrode. There are significantly less interactions between the glassy carbon and the [MPPi][TFSI] as compared to the background [MPPi][TFSI] CV with the Au electrode in Figure 20. The initial Li reduction peak is at -2.45 V vs Ag/AgCl for both of the method 1 and 2 solutions. This reduction is similar to the initial deposition peak at -2.37 V with the gold electrode. When comparing the two dissolution methods, there is an additional reduction peak at -0.4 V vs Ag/AgCl. This reduction peak is the reduction of the excess acid used for dissolution to

H₂ gas. This data further displays the lithium behaves the same in [MPPi][TFSI] whether dissolved using method 1 or method 2.

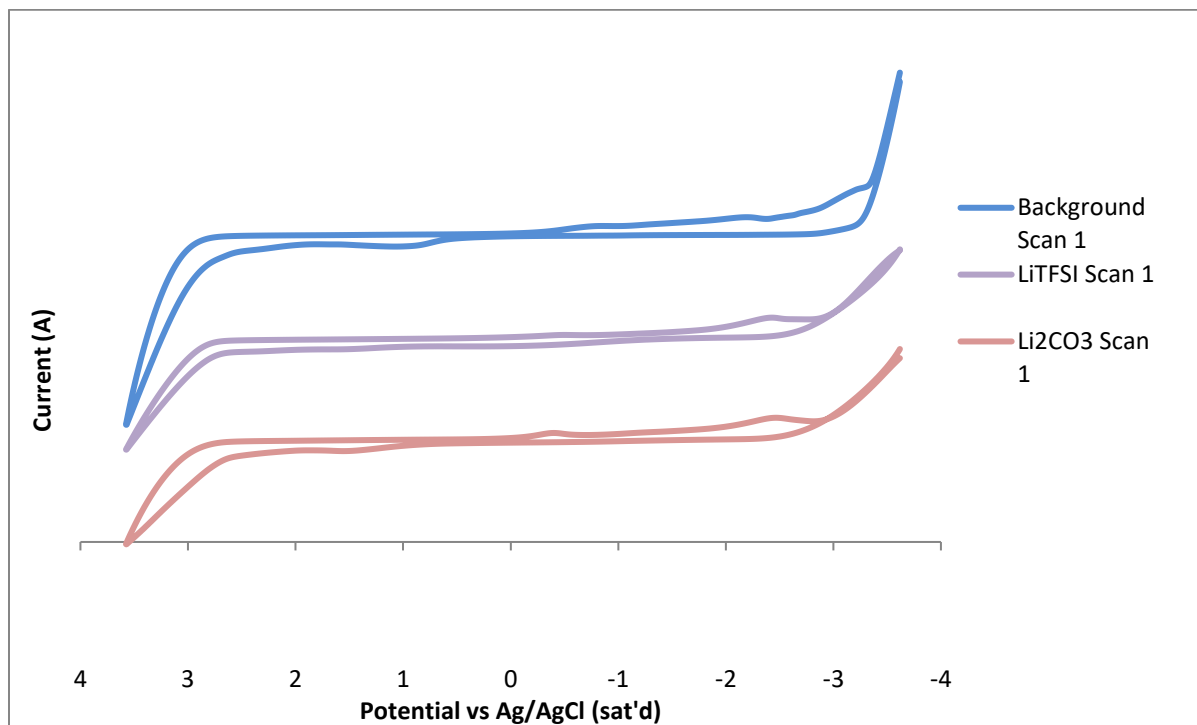


Figure 21: Cyclic voltametric response of a glassy carbon electrode in a. IL without Li. b. 0.5 M LiTFSI. and c. 0.5 M Li₂CO₃ dissolved directly into IL.

3.4 Deposition of Lithium on Gold Electrodes

Initially, the deposition of Li was achieved using a steady-state potential of -3.6 V vs Ag/AgCl. Deposition potentials in the range from -2.0 and -3.0 V vs Ag/AgCl were also attempted with less success. In addition, running twenty CVs before bulk deposition increased the overall deposits visible on the surface of the electrode. Lithium deposited on the edge of the electrode and grew dendritically when steady-state potential methods were utilized, Figure 22a. In contrast, a more uniform deposit of Li was achieved using the differential pulse methods after

CV conditioning, Figure 22b. The reduction pulse was -3.63 V vs Ag/AgCl for 5 seconds with the positive pulse held at +1.38 V vs Ag/AgCl for 0.5 seconds. The deposition was run for 20 hours in a 0.5 M LiTFSI solution. Deposits produced with the steady-state method adhered to the electrode poorly and delaminated from the electrode into the [MPPi][TFSI] when removed from solution. For comparison, the pulsed potential method produced deposits that adhered to the electrode surface with no observed delamination of deposits in the [MPPi][TFSI]. The recovery of Li material from the constant potential deposition was achieved and is provided in Figure 22c. The material was isolated from the IL and washed with acetone.

Bench top deposition produced deposits consistent with Figure 22 and provided the electrode was not exposed to atmosphere LiH was obtained. However, when removed from the IL the deposits rapidly converted to LiOH. The recovery of Li in inert atmosphere is necessary if LiH is the targeted product. Similarly, the use of rotary evaporation to reduce water in the [MPPi][TFSI] under decreased pressure significantly reduced visible hydrogen evolution during the deposition of LiH.

a.



b.



c.



Figure 22: a. Li deposits obtained from steady state potential of -3.6 V vs. Ag/AgCl. b. Li deposits obtained from differential pulse methods. c. dendritic deposits collected from constant potential deposition. Solutions contained 0.5 M Li.

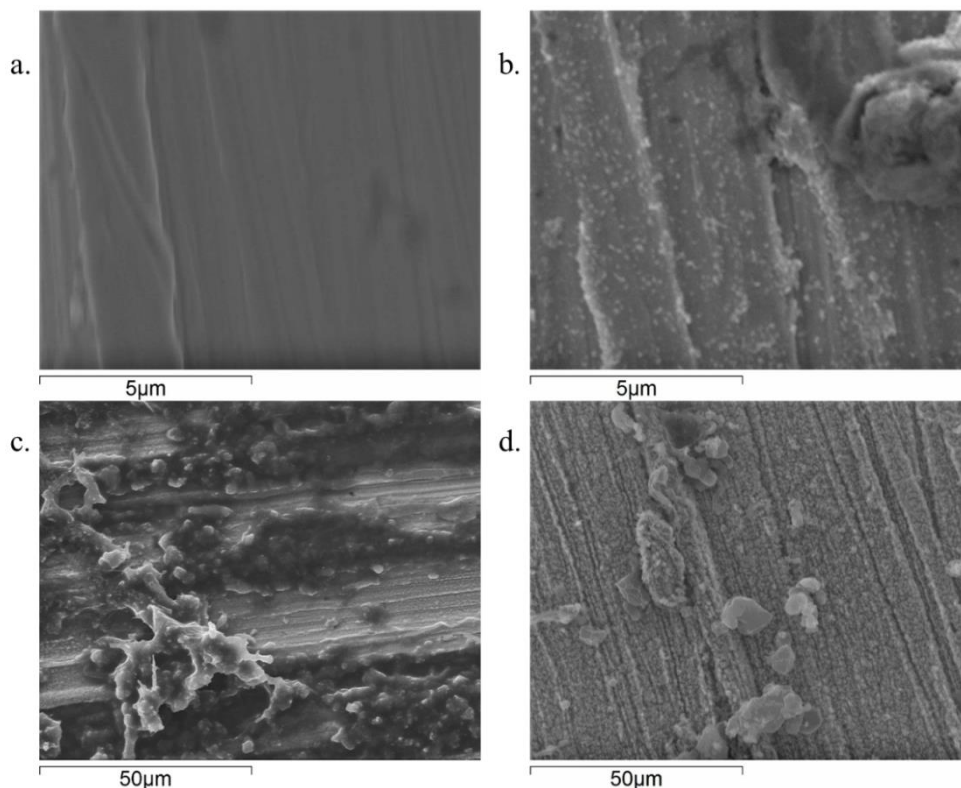


Figure 23: SEM images of a. Pristine Au electrode. b. Au electrode after 20 cycles between -3.6 V and +3.6 V vs. Ag/AgCl. c. Au electrode after the steady-state deposition method. d. Au electrode after the differential pulse method.

The SEM images of a pristine Au electrode, an Au electrode after 20 voltametric cycles, and electrodes after deposition of Li using both methods were obtained, Figure 23. The SEM image of the surface of a clean working electrode at 10,000 magnifications is shown in Figure 23a. The gold electrode surface after 20 voltametric cycles in a 0.5 M LiTFSI solution is presented in Figure 23b at 10,000 magnifications. The electrodes for steady-state and differential pulse methods are shown in Figure 23c and Figure 23d respectively at 1,000 times magnification. The vast majority of the deposits obtained from the steady-state electrode delaminated during the removal of the [MPPi][TFSI] with acetone washing. Therefore, only a few large dendritic

deposits are observed on the Au surface. In contrast the majority of the deposits from differential pulse method remained on the electrode during the removal of [MPPi][TFSI] with acetone. Further characterization with energy dispersive x-ray spectroscopy was not possible with the SEM system used. Therefore, the deposits were transferred to an inert cell and powder x-ray diffraction was obtained.

The electrochemical results show that performing 20 complete voltametric cycles produces Li nucleation sites. When the step was omitted from the deposition procedure, significantly fewer deposits were obtained at the electrode surface. The nucleation sites are well distributed on the electrode surface providing growth sites during subsequent reduction processes. In the case of the constant potential methods the evolution of hydrogen impacts the reduction of Li producing more dendritic deposits that do not adhere well. In contrast, deposition using differential pulse methods occurs within a much shorter period of time reducing the impact of hydrogen evolution at the negative potential limit. The continued replenishment of the double layer and shortened time at negative potentials allows the impact of hydrogen evolution to be diminished during Li reduction. Where holding the electrode at a constant potential that allows both Li^+ and H^+ reduction to occur based on bulk concentrations of both species and the inherent transport of species to the surface of the electrode. Thus, the SEM image of the steady-state deposition in Figure 23c also shows the formation of dendritic deposits on the micron scale. For comparison, the electrode from the differential pulse deposition (Figure 23d) has more uniform deposits that coated the Au electrode with some raised deposits on the surface.

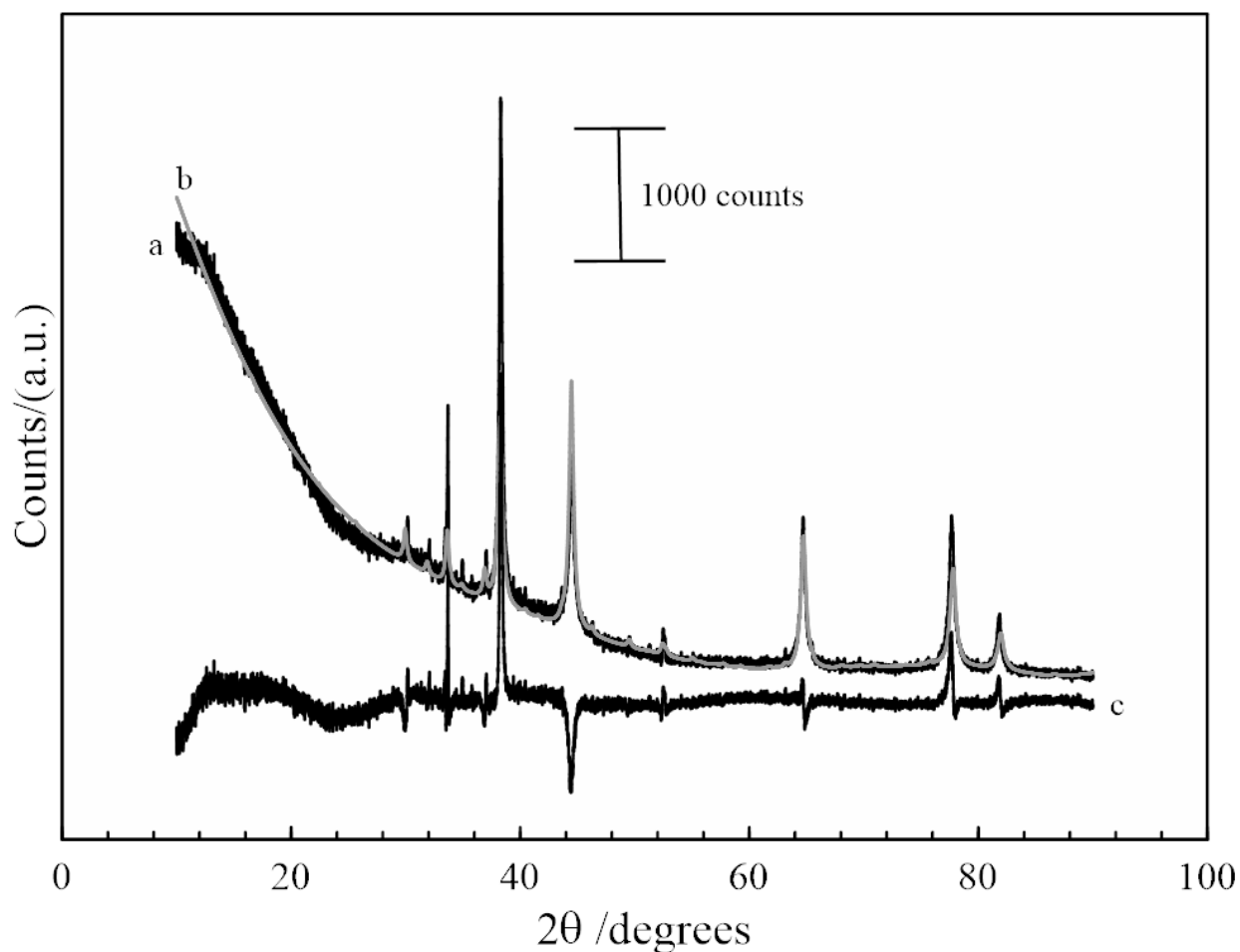


Figure 24: Powder X-Ray Diffraction (PXRD) of Li deposits at a gold electrode. a. Raw data b. Fit data for LiH, and c. the difference between raw data and the fit.

The powder x-ray diffraction was collected for the steady-state deposition, Figure 24. There was not an observable difference in diffraction for the deposits obtained from the two methods. Thus, only the steady-state response is presented. The raw diffraction pattern is provided in Figure 24a. The deposition of was fitted to primarily LiH (95%) with a small percentage of LiOH (5%), Figure 24b. The differential pattern between the raw and fitted data is also provided in Figure 24c. The pattern associated with LiH is obtained with PXRD when the

samples are in an inert atmosphere. However, once exposed to air, the deposits rapidly turn from grey metallic to black and the PXRD pattern is consistent with 100% LiOH (not shown). The chemical composition associated with the deposits is consistent with the electrochemical processes that are occurring at the gold electrode with hydrogen formation at -0.39 V and Li reduction at more negative potential to form LiH.

As discussed, the pulsed deposition lacks the dendritic growths of the steady state. The advantage to the pulse between the reduction potential of -3.63 V and 1.38 V is the replenishment of the double and diffuse layers. As the Li^+ is reduced and deposited onto the electrode surface, more of the species must diffuse into the double layer before it can be reduced. The pulsed method minimizes the impact of viscosity on the diffusion rate of species in ILs allowing the double and diffuse layer to be replenished. The irreversible nature of the lithium reduction makes this technique viable in ILs as less lithium is oxidized at positive potentials compared to the amount reduced during the negative potential pulse, Figure 20b and Figure 20c. The pulsed deposition resulted in much more uniform deposits that remained adhered to the electrode surface.

The discoloration of the [MPPi][TFSI] was also observed when utilizing steady state negative potential which is likely due to the reduction of the MPPi cation and subsequent degradation of the cation. Specifically, the [MPPi][TFSI] would turn a brown over the course of the 20 hours. The pulsed deposition method minimized the impact and no discoloration was observed after 20 hours. As noted in the background scan of the [MPPi][TFSI] in Figure 20a, the limit of the [MPPi][TFSI] is exceeded at -3.2 V vs Ag/AgCl and the MPPi and Li^+ are reduced. The potentials employed for the pulsed potential method minimize the time the MPPi can be reduced and subsequently allows the replenishment of both the Li and the cation with each cycle.

The collection of a PXRD pattern indicated that the recovered species is predominantly LiH. However, the reactive nature of the deposits gave rapid conversion to LiOH with exposure to the atmosphere. In some cases, the dendritic deposits were amorphous and not crystalline and the PXRD pattern was not easily obtained. The LiH patterns were collected by delaminating the deposits from the electrode surface onto a silicon low background stage that was then covered to maintain an inert atmosphere. In addition, the [MPPi][TFSI] can be left on the sample to provide a temporary barrier between the deposits and ambient oxygen and water in the air. However, over time as the sample remained exposed to air the conversion of LiH to LiOH was observed in the PXRD pattern.

3.5 Deposition of Lithium on Carbon Electrodes

Typically, LIBs utilize graphite electrodes. To maximize the lifespan of the LIBs, steps are taken to minimize the deposition of lithium during the cycling.¹⁰⁵ In this work, it was attempted to recover lithium on a macroscale with carbon electrodes. The same method of deposition was completed on a glassy carbon electrode as with the gold electrode. The steady-state deposition was completed after a 20 cycle CV. The electrode was held at -3.6 V for 44 hours in a 0.6 M LiTFSI solution in the glovebox. The resulting deposits are shown in Figure 25. These deposits are metallic in color and dendritic similar to those observed in the steady state deposits on the gold foil in Figure 22a. The success of depositing lithium on the glassy carbon disc electrode lead into experimenting with several other different forms of carbon.



Figure 25: Deposits on glassy carbon electrode in glove box after 44 hours of deposition at -3.6 V inside the glove box.

Deposits were successfully demonstrated using the steady state method on grafoil, carbon paste electrodes purchased from CH Instruments, and glassy carbon sheet electrode. Using the differential pulse method deposits were also achieved on a carbon fiber electrode. Li deposits on the grafoil are shown in Figure 26 after 20 hours at -3.6 V vs Ag/AgCl. Grafoil is a very cheap electrode. However, it could not withstand the very negative potential required for lithium reduction. The [MPPi][TFSI] solution after deposition on the grafoil electrode would be black due to the degradation of the electrode. Carbon screen printed electrodes were attempted next. Typically, this type of electrode is comprised of a carbon ink that has been screen printed onto a cardboard or plastic base with binders. Metallic deposits were achieved on the screen-printed electrode (Figure 27) after 42 hours at -3.6 V vs Ag/AgCl. This electrode caused minimal discoloration of the solution but the depositions were difficult to replicate due to bubbles forming

on the surface of the electrode. The bubbles were likely due to detrition of the binders, similar to the breakdown of the grafoil.



Figure 26: The grafoil electrode after 20 hours at -3.6 V in the glovebox.



Figure 27: The screen-printed electrode after 42 hours of total deposition time on PXRD stage before exposure to atmosphere.

Vitreous or glassy carbon is a form of graphite with glassy and ceramic properties. Glassy carbon disc electrodes are often used to gather speciation and electrochemical behavior information about electroactive species in solution as shown in section 3.3. Earlier in this section it was proven deposition of lithium on the glassy carbon electrode was possible. The glassy carbon foil

was used because it has a much larger surface area than the disc electrode so there is more area for electron transfers to occur. The electrode was held at -3.6 V Ag/AgCl for 24 hours. Deposits were present as shown in Figure 28 but minimal on the electrode surface and there were no deposits in the $[\text{MPPi}][\text{TFSI}]$ like when a gold foil is used.



Figure 28: Glassy carbon sheet electrode after 24 hours at $-3.63\text{ V vs Ag/AgCl}$.



Figure 29: Lithium deposits on carbon fiber electrode after 40 hours of pulsed deposition.

The most successful of the carbon electrode Li deposits were achieved with the carbon fiber electrode, shown in Figure 29. The [MPPi][TFSI] solution would absorb up the fibrous electrode so a gold foil was used to insulate the carbon fiber from the alligator clips. The pulsed deposition method was used for this electrode for a total of 40 hours. There was no discoloration of the [MPPi][TFSI] solution after deposition and deposits adhered to the electrode. The deposits were globular on the electrode surface despite the use of the differential pulsed deposition method, likely due to the lack of a uniform surface on the electrode.

It was shown that it is possible to deposit lithium on carbon electrodes. These deposits in the glove box were the same metallic color like the deposits on gold and are assumed to be LiH. Aside from the grafoil electrodes, all other carbon electrodes resulted in no discoloration of the solution even at longer run times, which always occurred with the gold electrodes after a 20-hour steady state deposition. This could make carbon-based electrodes more valuable in a process that would be reusing the [MPPi][TFSI]. However, the deposits often visually appeared to be much smaller than the deposits achieved with the gold electrodes. This is likely due to the poor electron transfer kinetics of carbon vs gold. Overall carbon electrodes are likely not as scalable as gold electrodes for the recovery of lithium from [MPPi][TFSI], but it was shown in this work that it is possible to recover lithium using a much cheaper, carbon-based electrode.

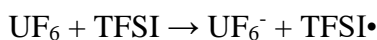
3.6 Conclusions

The direct dissolution of Li_2CO_3 or LiTFSI (obtained from Li_2CO_3) has been demonstrated in [MPPi][TFSI]. The solutions prepared from both chemical species are identical in terms of their electrochemical responses indicating Li^+ is the relevant species dissolved in IL. The production of nucleation sites using cyclic voltammetry was demonstrated and strongly impacted the bulk deposition of lithium on a gold electrode. The deposition was achieved using

both steady state and differential pulse potential methods. However, deposition using steady state methods produces dendritic deposits that do not adhere well to the electrode surface. The pulsed potential method produced more uniform and compact deposits that adhered to the electrode surface. The damage associated with the reduction of MPPi was visibly reduced with the pulsed potential deposition in comparison to the steady state potential method. PXRD of the lithium deposits obtained from both the dissolution of Li_2CO_3 and LiTFSI are consistent with LiH. Additional studies are necessary to evaluate the efficiency and optimize lithium recovery from IL. However, the results suggest that pulsed potential methods could be a viable option for the recovery of lithium from spent new generation LIBs in the form of LiH.

Chapter 4. Dissolution and Characterization of UF₆ in [MPPi][TFSI]

The direct dissolution of UF₆ into [MPPi][TFSI] is presented in this chapter. The uranium species in solution is characterized with XAFS, UV-Vis, FT-IR, Raman, and electrochemically. The reductive dissolution of solid UF₆ from U(VI) to U(V) occurs spontaneously after addition to the IL. It is proposed that the [TFSI] anion donates an electron to the uranium and becomes a free radical as shown below:



The XAFS and UV-Visible spectroscopy indicates the uranium remains in an octahedral conformation with 6 F⁻. The UV-Vis and Raman spectroscopies show the electronic transitions for the U(V) oxidation state. The isolation of the U(V)/U(IV) redox couple is used to help verify the initial oxidation state of the dissolved uranium species.

4.1 Introduction

The enrichment of uranium was performed to separate a sufficient quantity of highly-enriched U-235 to produce the first atomic bomb. The historical and current enrichment processes rely on the inherent physical properties (volatility) of uranium hexafluoride (UF₆) to achieve enrichment.¹⁹ The phase diagram indicates that UF₆ is a volatile solid at room temperature that can be liquefied at 64 °C with heating and reduced pressure. Finally, the volatility of UF₆ allows for the sublimation of the species to form gas at the triple point, 65 °C.²⁰ Using the volatility of UF₆, gaseous diffusion, gas centrifuges, and calutron techniques have all been used to exploit the physical properties of UF₆ for enrichment. The single, naturally occurring isotope of fluorine, ¹⁹F, makes UF₆ an ideal compound for isotopic separation by

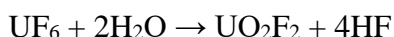
minimizing the total number of compound masses possible.²¹ Although UCl_6 does not produce HF gas²², it has similar physical properties. However, there are two stable isotopes of chlorine, ^{35}Cl and ^{37}Cl , resulting in multiple mass combinations, which complicates the enrichment process. UF_6 has two compound masses, 352 and 349 corresponding to ^{238}U and ^{235}U . Natural uranium is 99.3% ^{238}U and 0.7% ^{235}U , with trace amounts of ^{234}U . The enrichment of ^{235}U must be on the order of 3 to 5% to be useful for most current commercial nuclear power plants worldwide.²⁰

The two main historical processes of uranium enrichment involve gaseous diffusion or centrifugation. For gaseous diffusion, the UF_6 molecules are in thermal equilibrium and all isotopes having the same kinetic energy. The lighter $^{235}\text{UF}_6$ molecules travel at a higher velocity resulting in more collisions with a porous diffusion barrier, thus increasing concentration of ^{235}U within each sequential diffusion cell. In gas centrifugation, the isotopes are spun in large cylinders with a feed inlet in the center. Centrifugal force moves the heavier $^{238}\text{UF}_6$ preferentially to the outside and the lighter $^{235}\text{UF}_6$ to the inside. The separation factor is dependent on the peripheral speed and temperature of the gas. Separate output lines collected the enriched and depleted gases. Additional states of centrifugation are used until the desired level of enrichment is obtained.²⁴ The gas centrifuge method has displaced the gaseous diffusion method for all commercial uranium enrichment worldwide. As of 2019, the world capacity for UF_6 production was 62,000 metric tons of uranium per year (tU/yr). However, the actual amount of UF_6 produced was only 34,500 tU at approximately half the total capacity. After enrichment, about 90% of the original UF_6 is depleted uranium (DUF_6). This stream is stored primarily as UF_6 in 15 ton drums. As of 2007, only one fourth of the world's 1.5 million tons of DUF_6 had been converted back to uranium oxides or UF_4 ²⁷ resulting in a large stockpile of material. The

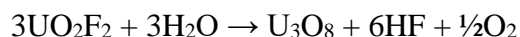
accumulation of DUF₆ from enrichment has become more significant over time and there are environmental concerns associated with the safe storage of this highly reactive and volatile material.

As stated previously the hydrolysis of UF₆ is vigorous and exothermic (-211.3 kJ/mol)²² when exposed to water, producing UO₂F₂, Equation 26. The reactivity poses considerable risk to storage, transportation, neutralization and recovery of useful materials from the UF₆. Likewise, the hydrolysis of UF₆ through inhalation poses a severe exposure risk where the in-situ formation of UO₂F₂ and subsequent formation of HF could occur in the lungs providing a long-term radiological dose. Moreover, the production of HF can target Ca in bones forming CaF₂ deposits in addition to the fact it is a known irritant to the eyes, skin, and mucus membrane²⁹. The high volatility and possible exposure risk for UF₆ if inhaled or ingested can be mitigated by safely converting the species to a less reactive and volatile species to reduce the chemical hazards associated with long term storage and individuals.³⁰

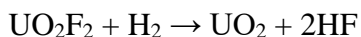
Current methods for conversion of UF₆ vapor utilize hydrolysis to form uranyl cation UO₂²⁺ which can then be converted to UO₂ or U₃O₈, Equation 27 and Equation 28.



Equation 26: Reaction of UF₆ with water



Equation 27: Reaction to covert uranyl fluoride to U₃O₈



Equation 28: Reaction to covert uranyl fluoride to UO₂

The addition of H_2 to the reactants of Equation 27 produces UO_2 instead of U_3O_8 .³² The species UF_6 is a strong fluorinating agent that will react with many oils, lubricants, and metals. The storage or containment of UF_6 is possible with fluorocarbons, chlorocarbons, nickel, aluminum or their alloys.²⁴ All of these factors make the storage, transport, and the conversion of UF_6 to more stable species difficult. Therefore, the use of alternative systems that eliminate water and volatility of UF_6 are desired to provide conversion pathways.

The ILs provide a unique chemical environment that has minimal water to limit the hydrolysis reaction with UF_6 . In addition, the cation/anion pairs associated with ILs can be chosen to provide high stability to minimize reactivity. They typically have relatively high viscosity when compared to aqueous systems, low volatility, and remain liquid at temperatures below 100 °C. Finally, ionic liquids have unique chemical properties including sufficient conductivity to allow the controlled electrochemical oxidation/reduction of chemical species that can be exploited in redox reactions. In addition, the stability of the cation and anion pairs is important as they can be reasonably resistant to radiative damage.^{71,106} Investigation of uranium in room temperature ionic liquids (ILs) began in the 1980s with the investigation of the U(IV)/U(III) redox couple and U(IV) to U(V) oxidation of uranium in $AlCl_3 + N$ -(*n*-butyl)pyridinium ([BPy]) chloride.⁶⁵ However, the reactivity of $AlCl_3$ based ILs with water required inert atmospheres to be useful. More recently the high stability of second generation ILs that utilize a variety of organic cations and anions have provided alternatives to water sensitive $AlCl_3$ based ionic liquids.⁶¹ However, the vast majority of second generation ILs suffer from low metal solubility and do not readily dissolve a variety of species.⁴⁶

Several studies have examined the dissolution and characterization of uranium oxides in ILs.^{63,107} These studies are often focused on utilizing ILs for electrochemical recovery of

uranium^{108,109} or extraction of uranium from spent nuclear fuel.¹¹⁰ In addition, the behavior of uranium halides in ILs has been explored. For example, UCl₄ was dissolved into an acidic mixture of AlCl₃ and N-(n-butyl)pyridinium chloride and electrochemically oxidized to U(V), confirmed by near-IR compared to previous work in molten salts.⁶⁵ In recent years, interest in ILs has increased as new techniques for dissolution of lanthanide and actinides have been developed.⁴⁶

The dissolution of uranium oxides has benefited from the development of acid functional cations in ILs. Dissolution of UO₃ was achieved using a 1:2 ratio with N,N-methylacetamidium [TFSI] in 1-ethyl-3-methylimidazolium [TFSI].¹⁰⁹ Dissolution of the carbonate species of f-orbital elements has easily been achieved with addition of the acidic anion of the IL.¹¹¹ This improves on the previously used acidic AlCl₃ mixtures by minimizing contaminants in the IL. In the example of uranyl carbonate the reaction in Equation 29 occurs to dissolve the uranyl and eventually off gases CO₂ and produces water that can be mostly removed via rotary evaporation.¹¹²



Equation 29: Dissolution of UO₂CO₃ with HTFSI

Additional methods utilized a mixture of carboxyl-functionalized ionic liquid and iron containing IL to improve the dissolution kinetics in dissolving UO₂.¹¹³ A new method for dissolution of f-orbital oxides utilizes an ozone stream through the IL to promote dissolution.¹¹⁴ Similarly, chlorine gas bubbled through 1-butyl-3-methylimidazolium ([BMIm]) [TFSI] resulted in the oxidation of UO₂ to form UO₂Cl₂.¹¹⁵

Dissolution has also been studied with tetra, penta, and hexavalent uranium halides. The U(IV) complexes of [EMIm]₂UBr₆ and [EMIm]₂UCl₆ ([EMIm] is 1-ethyl-3-methylimidazolium) were synthesized by adding uranium metal to their corresponding hydrogen halide with an excess of the ionic liquid of the [EMIm]X (X = Br or Cl). These compounds were successfully dissolved in both basic and acidic corresponding halide-aluminates.¹¹⁶ Similarly synthesized [BMIm]AnCl₆ (An = U, Np, Pu) and [MeBu₃N]UCl₆ ([MeBu₃N] is tri-n-butylmethyllummonium) have been successfully dissolved into [BMIm][TFSI] and [MeBu₃N][TFSI] respectively.^{67,68} Several UF₆⁻ salts were synthesized through the reduction of UF₅ with [Cation](FH)_nF resulting in green liquids of [Cation]UF₆ (Cations were [EMIm], [BMIm], [BPy], 1-butyl-1-methylpyrrolidinium ([BMPyr])).¹¹⁷ The [BMIm][UF₆] salt was later dissolved directly into [BMIm][TFSI] and evaluated electrochemically.¹¹⁸

The current studies examine the direct dissolution of UF₆ to help stabilize the volatile species. The goal is to provide a chemical matrix that can be used for U recovery, waste storage and/or safe transportation. A secondary goal is to develop pathways for capturing, transporting and analyzing forensic samples of UF₆ important in nonproliferation. As a non-volatile, non-reactive, and relatively temperature and radiation stable solvent, room temperature ionic liquids are a unique non-aqueous solvents for this task. This work demonstrates the direct dissolution of UF₆ into 1-methyl-1-propyl-piperidinium bis(trifluoromethylsulfonyl)imide ([MPPi][TFSI]). The characterization of dissolved UF₆ in the IL using spectroscopy including EXAFS and UV-Vis is examined and compared to literature. Finally, the dissolution mechanism will be presented.

4.2 Methods and Materials

4.2.1 Chemicals and Solutions

The dissolution of UF_6 is achieved through the direct addition of the solid to the IL, [MPPi][TFSI]. The 1-propyl-1-methylpiperidinium bis(trifluoromethylsulfonyl)imide 99% ([MPPi][TFSI]) was purchased from IoLiTec. The UF_6 was depleted and supplied by URENCO. The UF_6 was shipped and stored in a P10 tube with a bolted top.

4.2.2 Dissolution of UF_6

All work was completed in an inert atmosphere in a VAC glovebox equipped with a cold well and cold storage assay. The P10 tube is stored in a cold storage assay at $-15\text{ }^\circ\text{C}$. Before dissolution, the P-10 tube was cooled to liquid nitrogen temperatures using the cold well. In a scintillation vial, a measured amount of room temperature [MPPi][TFSI] is added. The chilled P10 tube is opened and the UF_6 is removed with a metal spatula and added directly into the [MPPi][TFSI]. The mass of the addition was measured by the mass changes of the vial. As the UF_6 warms, it becomes waxy and is more difficult to remove from the P10 tube. When this occurs, temporarily placing it back into the cold well to chill makes it easier to transfer once again. The freshly made solutions are stirred with a stir bar and magnetic stir plate overnight.

4.2.3 XAFS Studies

The XAFS measurements were performed at the Advanced Photon Source at the BESSRC-CAT 12 BM station at Argonne National Laboratory. The U samples (solid and solution) were placed in an aluminum sample holder equipped with Kapton windows. XAFS spectra were recorded at the U- L_3 edge (17,166 eV) in transmission mode (solution) and fluorescence mode (solid) at room temperature using a 13-element germanium detector. A double crystal of Si [1 1 1] was used as a monochromator. Energy calibration was performed

using a Zr foil (K edge = 17,998 eV). Several XAFS spectra were recorded over the k range [0–18 Å⁻¹ and averaged. The background contribution was removed using Athena software and data analysis performed using WINXAS. For the fitting procedure, scatterings wave functions were calculated by FEFF8.2; the input files were generated by ATOMS. The adjustments of EXAFS spectra were performed under the constraints $S_0^2 = 0.9$, a single value of energy shift ΔE_0 was used for all scattering. The uncertainty on the coordination number (C.N) is 20%, the uncertainty on the distance (R) is 20%. Samples were taken twice for XAFS measurements.

4.2.4 UV-Vis, FTIR, and Raman Spectroscopy

UV-Vis spectra were obtained at room temperature in a 1 cm sealed quartz cell under argon. The measurements were taken with a Cary 6000i double beam spectrometer. The UV-Vis of the UF₆ containing solutions was background subtracted with the [MPPi][TFSI].

The FT-IR spectra were collected on a Varian 3100 FT-IR Excalibur series spectrometer with the Varian Resolutions Pro, version 5.04.009 software. Ionic liquid solutions were measured by placing a small amount directly on the sample stage. Samples were disposed of afterwards due to their exposure to atmosphere.

Raman spectroscopy was completed in an inhouse sample holder with a sapphire window. The samples were sealed in inert atmosphere. The measurements were completed using 514.5 nm excitation line. The data was collected on a Princeton Instruments SP2750i spectrometer with a 1800 groove/mm holographic grating and a PIXIS 400 camera.

4.2.5 Electrochemical Studies

A non-aqueous reference electrode was constructed using a BASi (Part number MF-2062) kit. The Ag wire electrode was combined with an internal silver nitrate solution prepared as described by A. Saheb, et. al⁷⁷. For the experiments, approximately 4 mL of UF₆ in

[MPPi][TFSI] were added to an electrochemical cell. The counter electrode was a platinum sheet. The working electrode was gold or glassy carbon. A CH Instruments Inc 600 series potentiostat with the corresponding CHI software were used for all electrochemical studies. Studies were completed in a glovebox with an argon atmosphere. A glassy carbon disc electrode (Part number MF-2012) with a 3.0 mm diameter was used for the cyclic voltammetry data as well. The CV was conducted at various scan rates and potential ranges. All voltages listed in the experimental are those entered into the CHI software and not corrected with a ferrocene standard. The potentials reported in the results and discussion is reported vs Ag/AgCl Sat'd KCl based on the measurement of a ferrocene standard in the same IL with the same reference electrode.

4.3 Dissolution of UF₆ in IL

The handling and measurement of solid UF₆ held at liquid nitrogen temperature is relatively straight forward in an inert atmosphere glovebox equipped with an analytical balance. The white solid is measured directly into the IL on a balance to provide accurate mass. The dissolution occurred rapidly after addition to [MPPi][TFSI] with a visible change of the white solid to yellow, Figure 30a. The initial color change is followed by rapidly dissolution to form a turquoise solution within minutes, Figure 30b. At lower concentrations (< 0.5 M), dissolution is completed with stirring as the color of the solution gradually changes from turquoise to green over a few hours. At higher concentrations (> 0.5 M), dissolution happens rapidly with exothermic heating. The increase in temperature is responsible for the increased rate of dissolution at higher concentrations. The exothermic nature of the reaction is consistent with the spontaneous direct dissolution of UF₆ in the IL to form the green solution observed in Figure 30c. The evolution of gas was observed in the IL at higher concentrations suggesting some

degradation of the IL or formation of gaseous UF_6 occurs. The dissolution vial was capped after addition of UF_6 to minimize any possible emission of UF_6 into the glovebox.

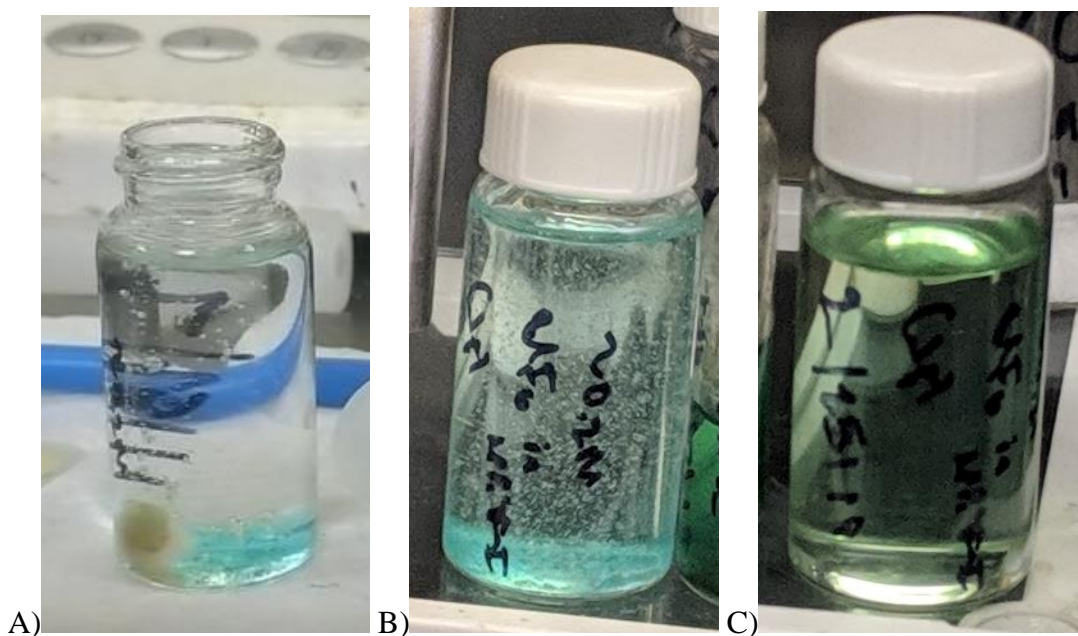


Figure 30: A 0.1 M solution A) as addition occurred, B) after shaking C) two days later

4.4 Characterization with XAFS Studies

The coordination of UF_6 in IL was examined and the fitted k^3 -EXAFS spectra and Fourier transform of k^3 -EXAFS spectra of 0.1 M UF_6 in $[\text{MPPi}][\text{TFSI}]$ at 10 days after preparation are presented in Figure 31. For reference, the spectra provided in Figure 31 could not be obtained for UF_6 dissolved in IL earlier as the samples had to be produced at University of Nevada, Las Vegas, packaged and shipped to the ATLAS beamline at Argonne National Lab in Chicago, Illinois. The fitted data indicates that the uranium remains bonded to all six fluorides. The U-F bond length is $2.02 \pm 0.02 \text{ \AA}$. The normalized XANES spectra of the U_L3 edge of the 0.1 M 1 week sample, a 0.1 M six-month-old sample and 0.7 M six-month-old sample are

presented in Figure 32. The absorption edges and maximum (white-line) energies listed in Table 1. The absorbance edges of the 0.1 M 1 week and 6-month samples were 17166.2 eV and 17166.1 eV and the 0.7 M 6 month sample was 17164.0 eV. The maximum of the XANES for the three samples were 17174.0, 17173.6 eV, and 17174.2 eV respectively. The consistency in all of these data points indicates the stability of the oxidation state of the U in the [MPPi][TFSI]. XANES of solid UF_4 and $\text{UO}_2(\text{NO}_3)_2$ and UI_3 in 1-butyl-1-methylpiperidium [TFSI] were collected as U(IV), U(VI), and U(III) reference materials. The comparison graph of the reference materials and UF_6 samples is included in Figure 33. The reference materials are in different environments from the UF_6 dissolved in [MPPi][TFSI] and therefore cannot be directly compared. However, the white line energies differ (> 2 eV) from the dissolved UF_6 , suggesting the U of the dissolved species is in the +5 state. Specifically, the initial dissolved species for UF_6 is the UF_6^- species in the IL solution. The bond lengths and coordinated atoms derived from the EXAFS data are provided in Table 2. The data includes samples of a 0.1 M solution at 1 week, 1 month, and 13 months and the 0.7 M sample at 6 months and 13 months. All samples were only found to be coordinated with 6 F atoms within the error associated with the measurements. The 1-month-old 0.1 M sample with 7.5 ± 1.5 U-F bonds is the only outlier observed. However, the value of 6 F is still within the error of the measurement. The bond lengths are consistent ranging from 2.04 to 2.06 ± 0.2 Å.

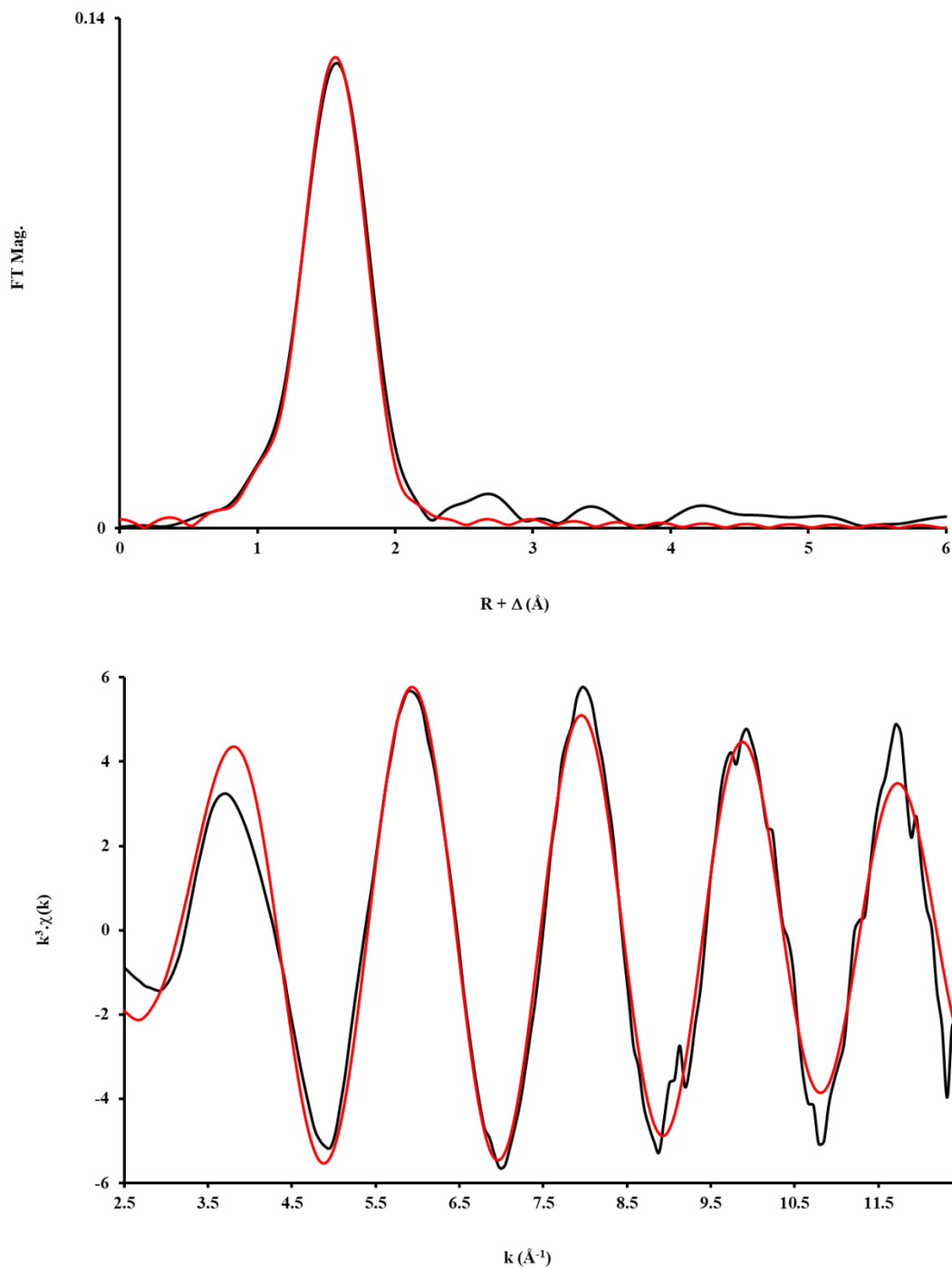


Figure 31: Fitted k3-EXAFS spectra (bottom) and Fourier Transform (top) of k3-EXAFS spectra of 0.1 M UF₆ in [MPPi][TFSI] at 10 days old. Adjustment between $k = [2.4\text{--}12.5]$ Å⁻¹. Residual = 3.27%. Experimental data in black and fit in orange. Fitted for 6.2 ± 1.2 U-F bonds at $2.05 \pm$

0.02 Å

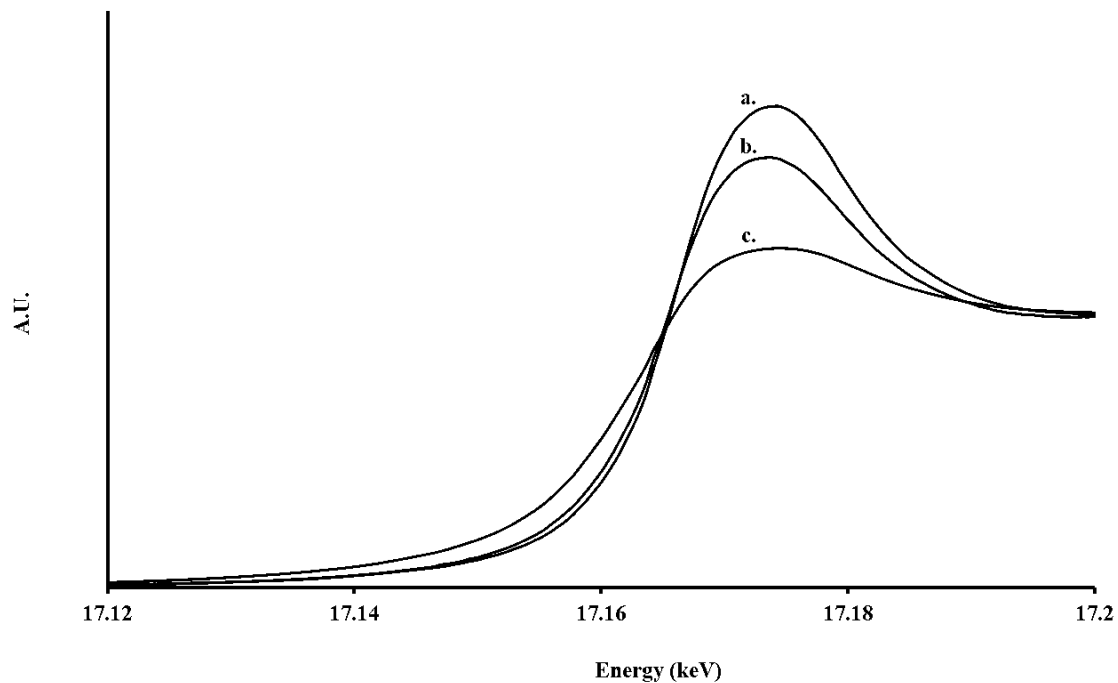


Figure 32: Normalized XANES spectra at the U_L3 edge of (a.) 1 week 100mM UF₆ (b.) 6 month old 100mM UF₆ and (c.) 6 month old 700mM UF₆

Table 1: Absorption edge and white-line at the U_L3 edge of samples in Figure 32.

Sample	Edge (eV)	White line (eV)
0.1 M UF ₆ 1 Week	17166.2	17174.0
0.1 M UF ₆ 6 Month	17166.1	17173.6
0.7 M UF ₆ 6 Month	17164.0	17174.2

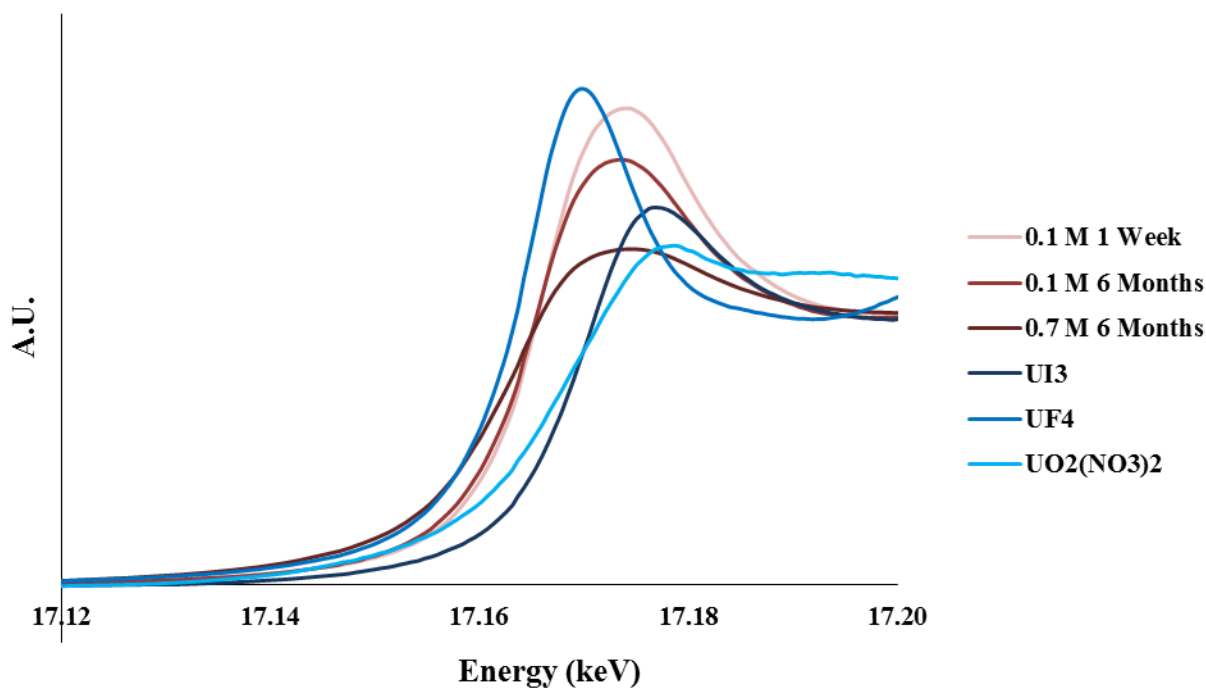


Figure 33: Normalized XANES spectra at the U_L3 edge of the same samples with standards.

Table 2: Structural parameters obtained from the adjustment of the k3-EXAFS spectra of the solution samples at various ages and concentration.

Solution Sample		C.N	R (Å)	σ^2 (Å ²)	ΔE_0 (eV)	R (%)
0.1 M UF ₆ 1 week	U-F	6.2 ±1.2	2.05(2)	0.003	-0.68	3.27
0.1 M UF ₆ 1 month	U-F	7.5 ±1.5	2.04(2)	0.003	-4.91	6.40
0.1 M UF ₆ 13 months	U-F	5.7±1.1	2.04(2)	0.003	-2.70	6.82
0.7 M UF ₆ 6 months	U-F	6.5 ± 1.3	2.06(2)	0.003	-8.22	4.19
0.7 M UF ₆ 13 months	U-F	6.1±1.2	2.05(2)	0.003	-1.38	2.94

4.5 UV-Vis Transition Assignments and other Spectral Data

The UV-Vis data for a 0.1 M UF₆ in [MPPi][TFSI] sample at 4 hours, 1 and 8 days is provided in Figure 34. The spectra are background subtracted for [MPPi][TFSI]. The spectra are

only presented at wavelengths longer than 500 nm due to the strong absorption at shorter wavelengths for the IL and specifically the TFSI anion. There are several characteristic peaks in this UV-Vis spectra that are associated with U(V). Specifically, bands in the 600 to 800 nm range including peaks at 621, 639, 706, 758 nm are assigned to the $\Gamma_7 \rightarrow \Gamma_6$ transition. The peak at 980 nm is assigned to the $\Gamma_7 \rightarrow \Gamma_8'$ transition. Finally the characteristic bands at 1262, 1322, 1328, 1352, and 1371 nm are assigned to the $\Gamma_7 \rightarrow \Gamma_7'$ transition.¹¹⁹

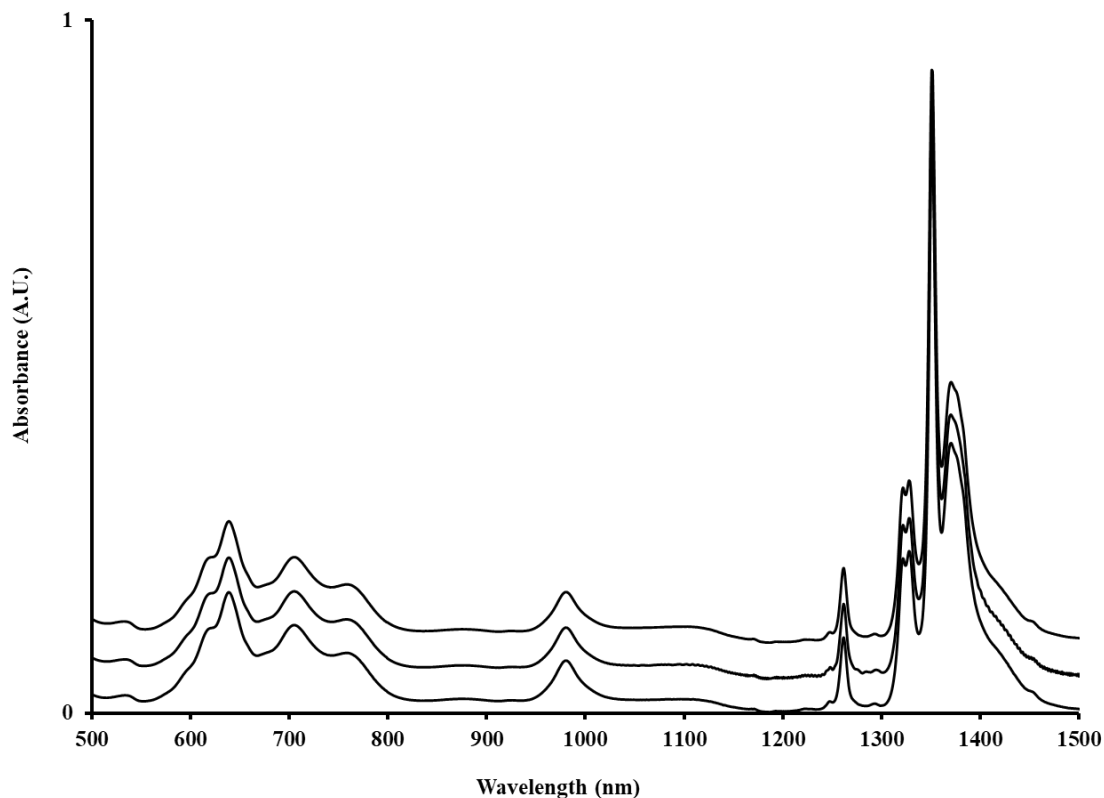


Figure 34: UV-Vis over time of 0.1 M UF_6 in $[\text{MPPi}][\text{TFSI}]$. The bottom spectrum was 4 hours, 24 hours and the top being 8 days. The 24 hour and 8 day spectra are shifted up for comparison.

There have been several studies of U(V) compounds with similar UV-Vis characteristics. Asprey and Penneman¹²⁰ reported the UV-Vis of 5 M U(V) in a 24% HF solution. They observed the solution to be blue for the U(V) compounds consistent with the initial turquoise color of the IL solutions with dissolved UF₆. In addition, bands for the $\Gamma_7 \rightarrow \Gamma_6$ and $\Gamma_7 \rightarrow \Gamma_8'$ transitions are present in their spectrum. They also observe the $\Gamma_7 \rightarrow \Gamma_7'$ transition for the U(V) species which is consistent with the spectra for the dissolution of UF₆ in IL. Finally, four different peak shapes are presented for the $\Gamma_7 \rightarrow \Gamma_7'$ transition indicating that the cation interacts with the UF₆⁻ complex in solution.^{120,121}

In a review of uranium (V) chemistry, Selbin and Ortego comprised the first few studies of U(V) compounds. U(V) is unique due to its 5f¹ electronic configuration. Most of the f-f transitions can be observed because of the singular 5f electron associated with U(V) compounds. The term symbol of the system is ²F_{5/2,7/2}. The initial splitting of the ²F_{5/2} and ²F_{7/2} energy levels is due to spin-orbit interactions. The O_h crystal field of the U further splits the ²F_{5/2} into the doubly degenerate Γ_7 and quadruple degenerate Γ_8 . For comparison, the ²F_{7/2} is split into the doubly degenerate Γ_7' and Γ_6 and quadruple degenerate Γ_8' .¹¹⁹ The presence of all three transitions within the UV-Vis spectra of solutions from the dissolution of UF₆ in the IL also further supports that the uranium remains in an octahedral configuration coordinated with six fluorides as observed in the XAFS data.

The IR spectrum of the [MPPi][TFSI] with and without UF₆ is shown in Figure 35 over the course of a week. In the short term there are few changes in the IR spectra. The spectra of the [MPPi][TFSI] with and without UF₆ are almost identical. In order to better see the changes in the two, the [MPPi][TFSI] spectra are subtracted from the UF₆ containing spectra in Figure 36. There are approximately three peaks that increase in intensity at 1326, 1162, and 1027 cm⁻¹ and

four that decrease at 1440, 1237, 1120, and 874 cm^{-1} . These changes are all less than 5 %Transmission. Uranium (V) and (IV) fluoride vibration bands in the IR range all occur at wavenumbers below 500 cm^{-1} which could not be observed by our instrumentation. The changes that occur in the UF_6 containing IR spectra are a result of interactions between the cation and the UF_6 anion.

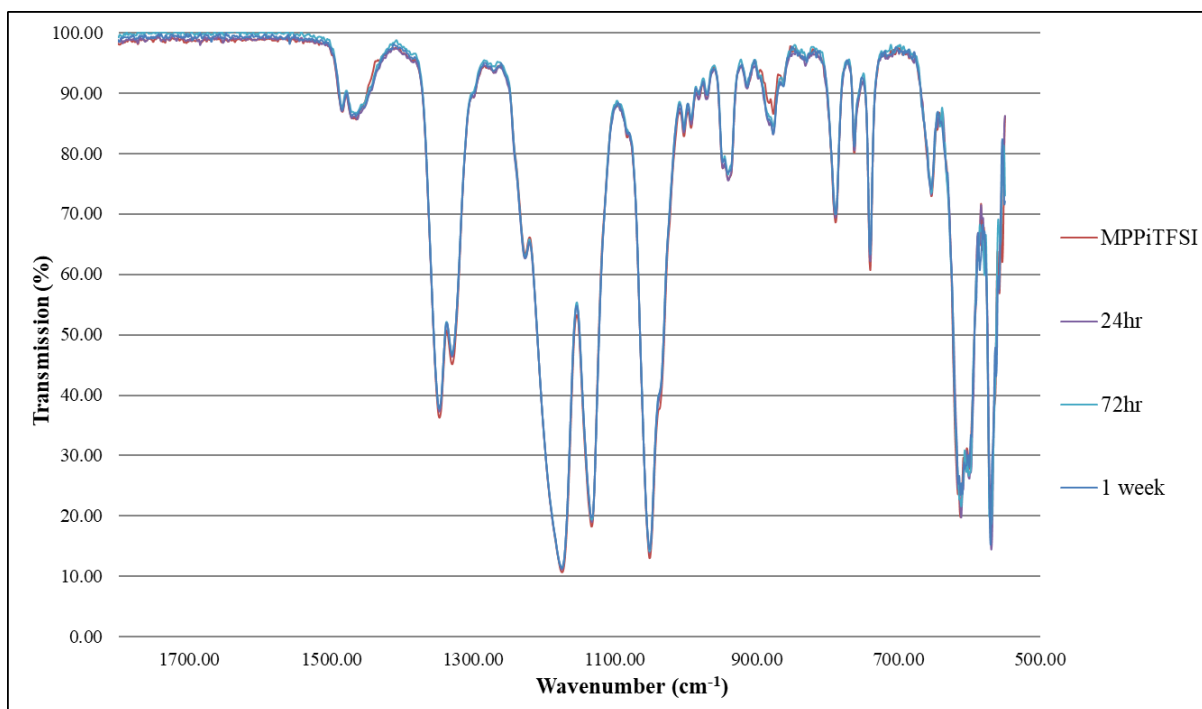


Figure 35: IR Spectra of 0.1 M UF_6 in $[\text{MPPi}][\text{TFSI}]$ over the course of a week.

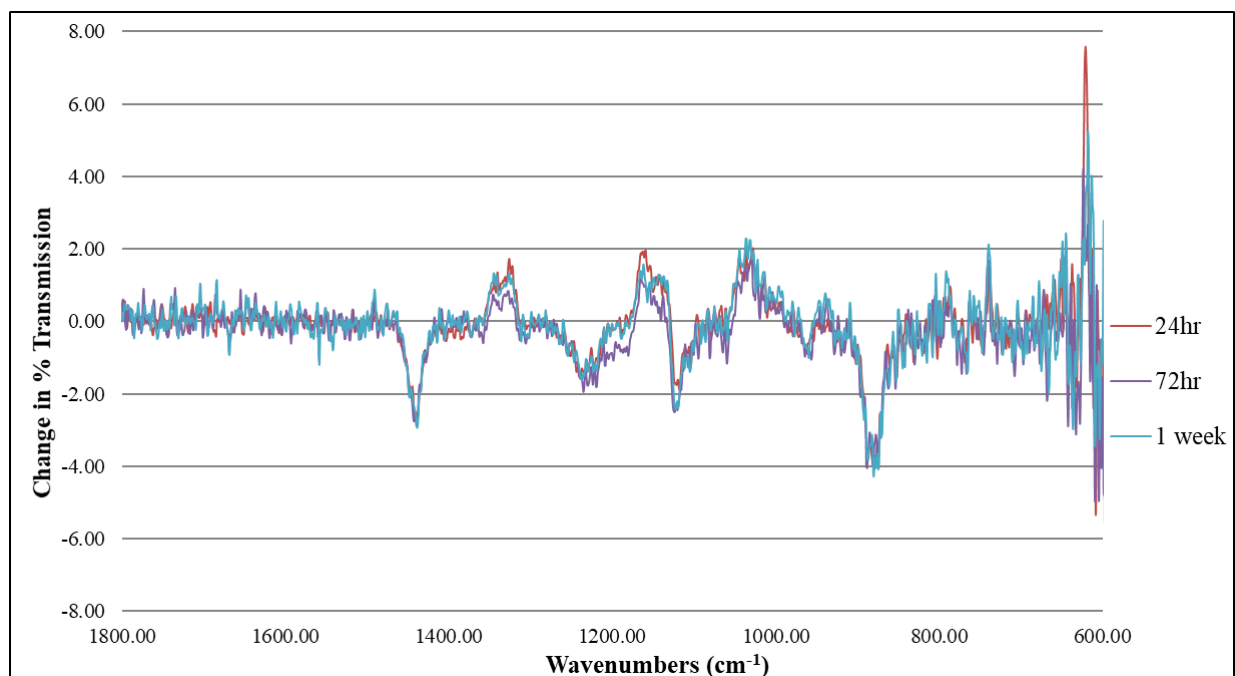


Figure 36: The difference in the spectra after subtracting the [MPPi][TFSI] from the aged UF_6 solutions.

In Figure 37 is the Raman spectra of pristine [MPPi][TFSI] and 0.5 M UF_6 in [MPPi][TFSI] at 1 week old. The solutions were sealed and collected under inert atmosphere. There are three new peaks between the two samples all in the 100 to 700 cm^{-1} range as shown in Figure 38. Two of these are the Raman active ν_1 and ν_5 vibrations of UF_6 at 610 and 197 cm^{-1} respectively.^{117,119} There is a third peak at 418 cm^{-1} that differs from the [MPPi][TFSI]. Based on literature assignments, the peaks at 399 and 406 cm^{-1} are due to wagging of the SO_2 in the [TFSI].^{122–124} Later in this chapter the mechanism for the reduction of the uranium is discussed. It is theorized the [TFSI] anion donates an electron and becomes a free radical. In the literature it is shown a fragmentation of TFSI^\bullet occurs to give $\text{CF}_3\text{SO}_2^\bullet$ (Equation 30).^{125,126} The author

proposes this new peak at 418 cm^{-1} in the Raman may be a change in the wag of the SO_2 due to the fragmentation of the [TFSI] radical.



Equation 30: Possible fragmentation of TFSI• radical¹²⁵

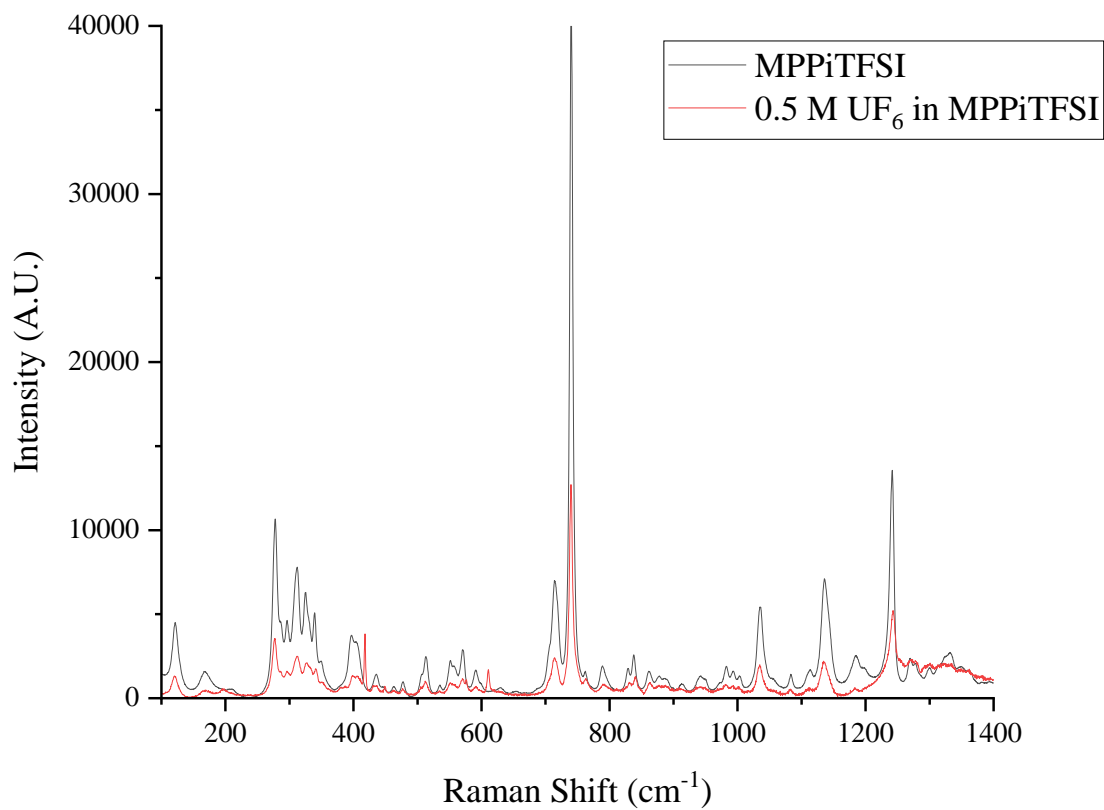


Figure 37: Raman spectra of [MPPi][TFSI] and 0.5 M UF_6 in [MPPi][TFSI] at 1 week old.

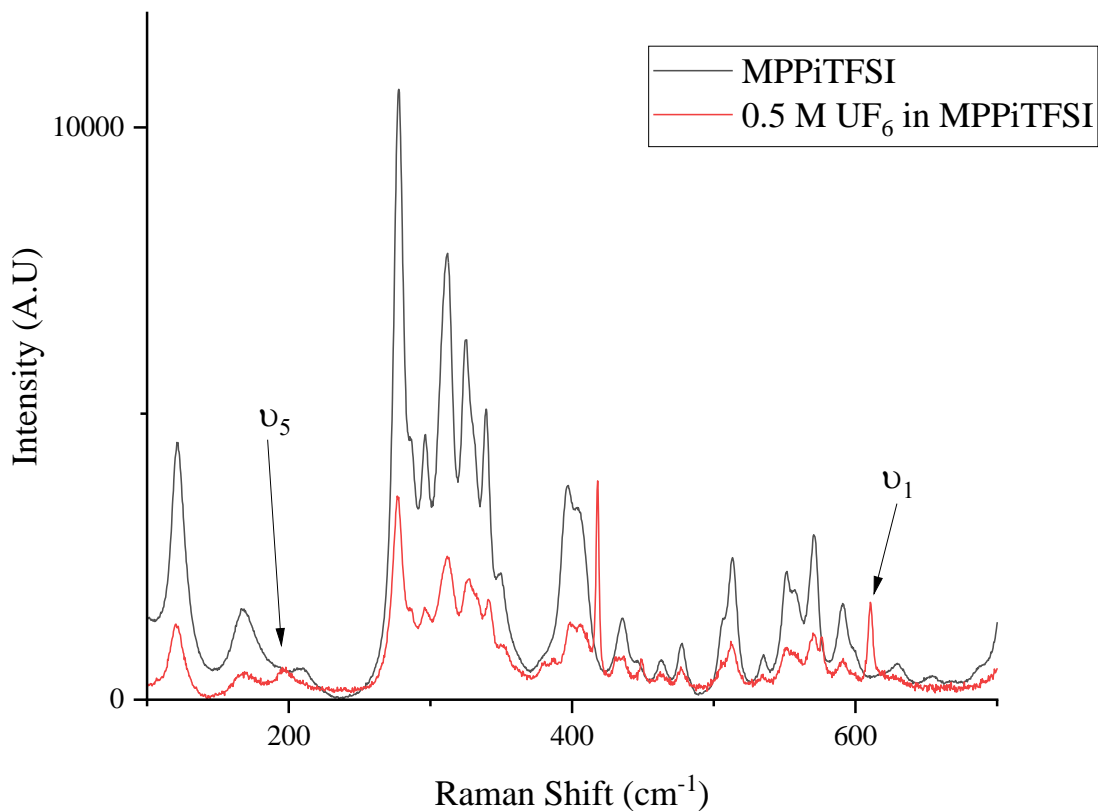


Figure 38: Raman Spectra with labeled U(V) vibrations

4.6 Electrochemical Characterization

Brief electrochemical studies have been completed with the UF_6 in $[\text{MPPi}][\text{TFSI}]$. In Figure 39 is the CV of the 0.096 M UF_6 in $[\text{MPPi}][\text{TFSI}]$ on a glassy carbon disc electrode. In the first scan there is one minor reduction peak at -1.21 V vs Ag/AgCl. Also shown in Figure 39 is the final scan of a 20 cycle CV. The reduction peaks are more distinct in the final scan. The ingrowth of the peak at -2.45 V vs Ag/AgCl is possibly the bulk deposition of the U(IV)

compound. This will be further discussed in Chapter 5. The peak at -1.02 V vs Ag/AgCl grows in over subsequent cycles along with a very small more positive peak at -0.58 V vs Ag/AgCl.

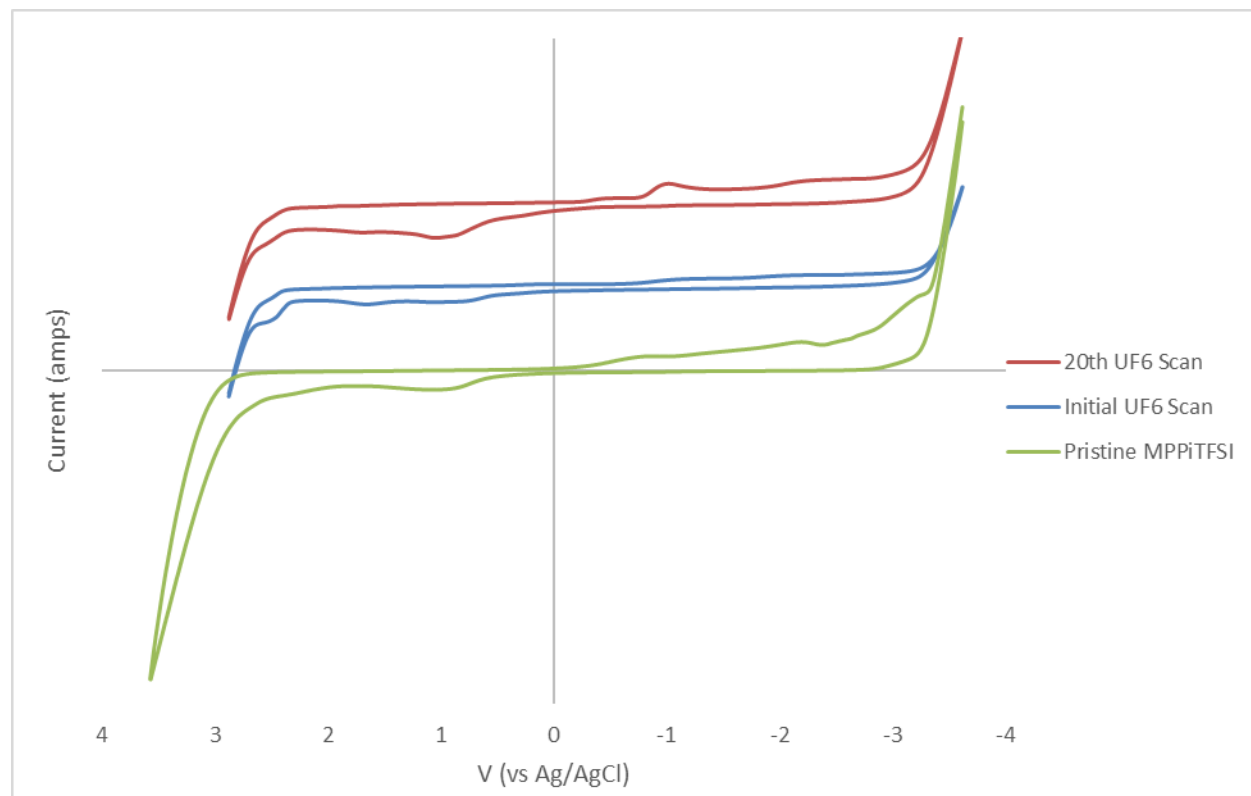


Figure 39: Cyclic voltammetry of the 0.096 M UF_6 in $[\text{MPPi}][\text{TFSI}]$ with a glassy carbon electrode.

Attempts were made to isolate the various reduction peaks. The only peaks that was successfully isolated is the suspected U(V) to U(IV) in Figure 40. In order to achieve this peak, larger electrochemical windows needed to first be scanned. If a fresh solution was just scanned from -0.02 to -1.62 V vs Ag/AgCl, no peaks were observed. More positive scans as shown in the blue scan in Figure 40 were needed to be completed first. In the blue scan there is a reduction peak at -0.35 V vs Ag/AgCl. Based on the previous evidence from XAFS and UV-Vis the initial

solution is all U(V). It is possible while scanning to more positive potentials some of the U(V) is oxidized back to U(VI). This -0.35 V vs Ag/AgCl peak is then the reduction of U(VI) to U(V). The resolved couple in red is the U(V)/U(IV) redox couple.

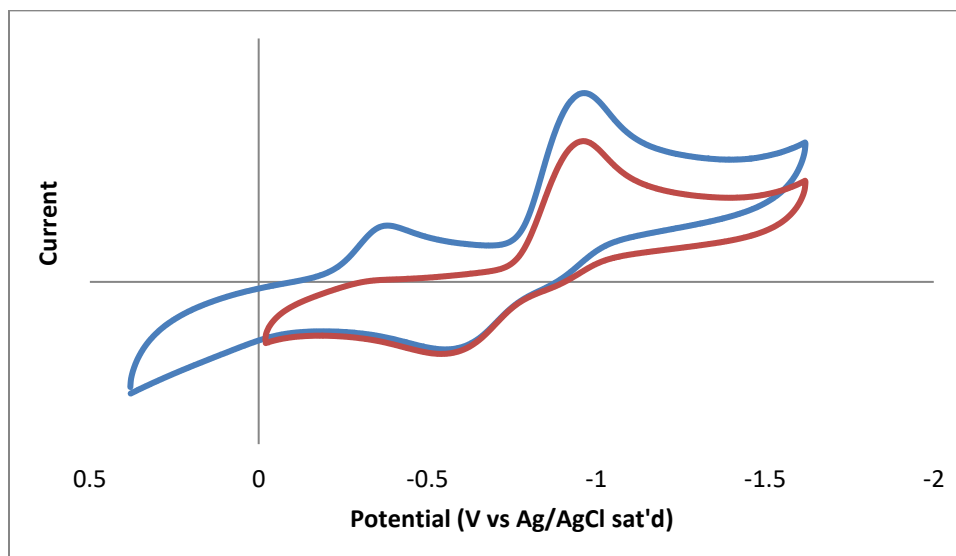


Figure 40: Isolated U(V) /U(IV) redox couple (in red) and coupled with the U(IV) to U(V) peak (in blue).

A scan rate study was completed from 5 mV/s to 100 mV/s in Figure 41. At the slower 5 and 10 mV/s scan rates the reduction peak at -0.35 V is still visible. In Figure 42 the cathodic peak current, i_{pc} , and anodic peak currents, i_{pa} are graphed as a function of the square root of scan rate. These relate back to the Randles-Sevcik equation for a fully reversible system at room temperature is shown in Equation 31 and quasi-reversible or irreversible system in Equation 32.⁵² As shown in Figure 42, both the i_{pc} and i_{pa} over the various scan rates are relatively linear. This mean the system follows the Randles-Sevcik equation and it can be used to determine the diffusion coefficient of the species of interest. By applying the Randles-Sevcik equation to Figure 42, the diffusion coefficient for the electroactive species can be calculated.

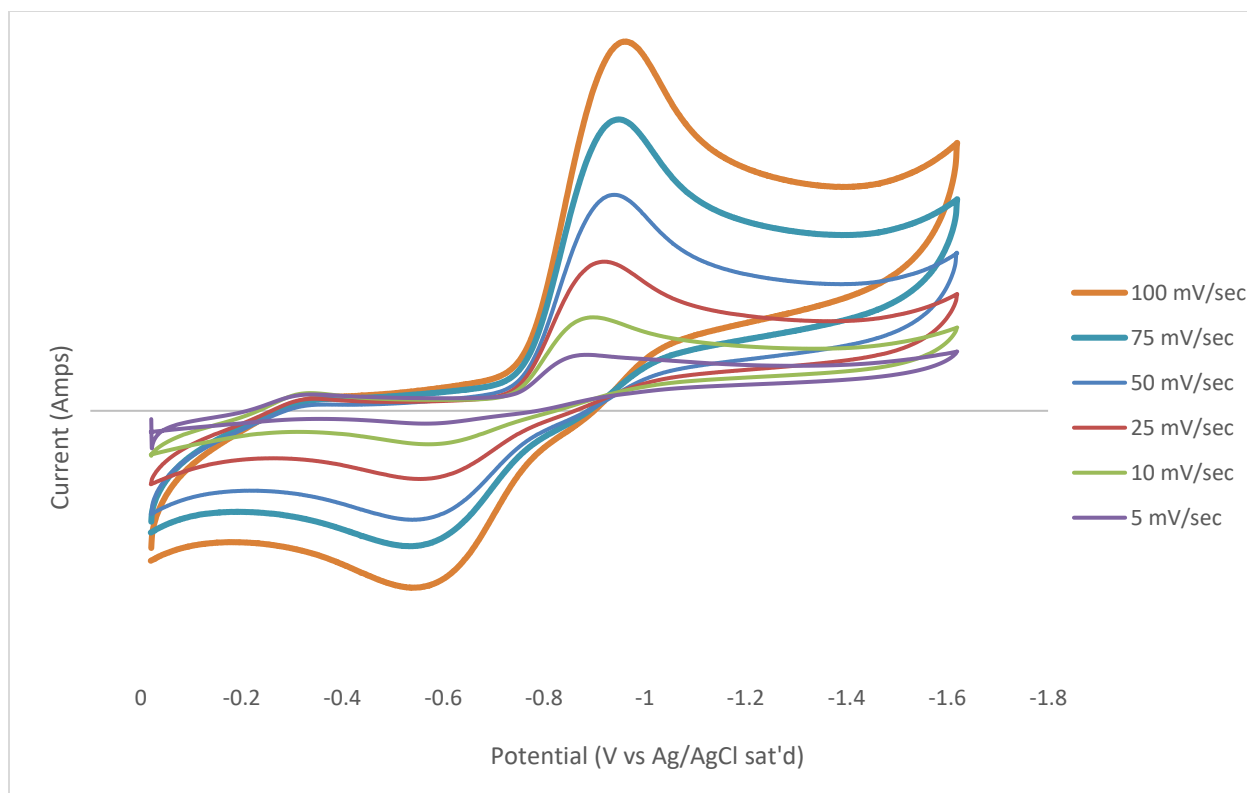


Figure 41: Scan rate study of U(V)/U(IV) couple with glassy carbon disc electrode.

$$i_p = 2.69 * 10^5 (n^{\frac{1}{2}} A D^{\frac{1}{2}} C v^{\frac{1}{2}})$$

Equation 31: Randles-Sevcik equation for a fully reversible system.

$$i_p = 2.99 * 10^5 (n^{\frac{3}{2}} \alpha^{\frac{1}{2}} A D^{\frac{1}{2}} C v^{\frac{1}{2}})$$

Equation 32: Randles-Sevcik equation for a quasi-reversible or irreversible system.

Where:

n= number of e⁻ transferred

A= Area of the electrode (cm²)

D= diffusion coefficient (cm²/s)

C= Concentration (mols/cm³)

v= scan rate (V/s)

α= correction factor dependent on E_p and E_{p/2}

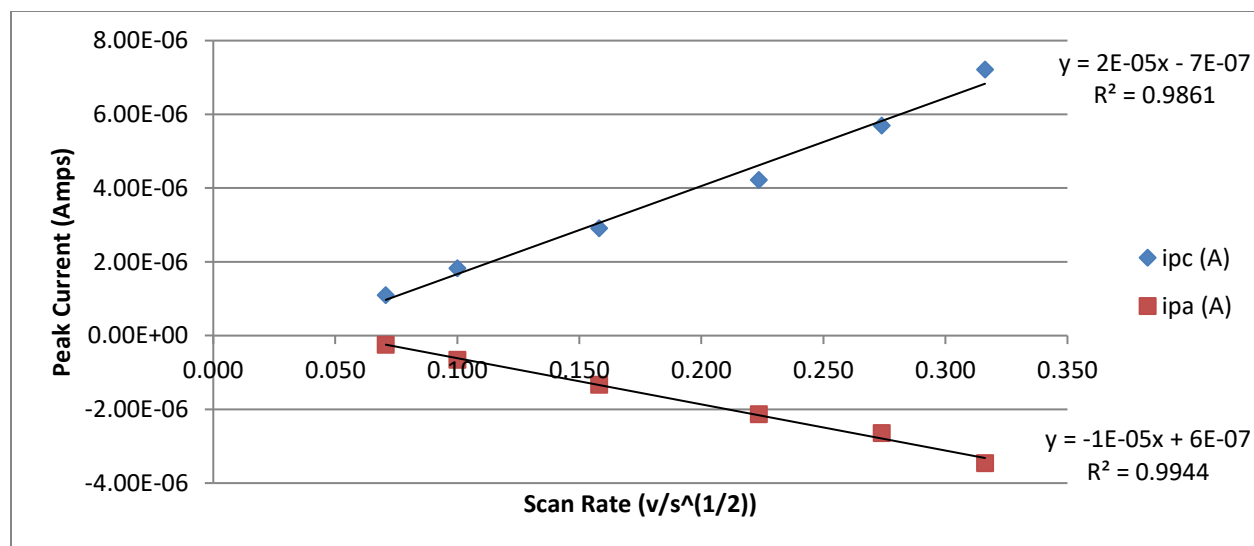


Figure 42: Peak currents graphed as a function of the square root of scan rate.

Table 3: Data from Scan Rate Study

Scan Rate (mV/s)	E_{pc} (V vs Ag/AgCl)	i_{pc} (A)	E_{pa} (V vs Ag/AgCl)	i_{pa} (A)	i_{pc}/i_{pa}	ΔE_p (V)	E° (V vs Ag/AgCl)
5	-0.88	1.09E-06	-0.56	-2.51E-07	4.36	0.32	-0.72
10	-0.90	1.83E-06	-0.57	-6.54E-07	2.79	0.33	-0.73
25	-0.92	2.92E-06	-0.54	-1.33E-06	2.19	0.38	-0.73
50	-0.94	4.22E-06	-0.54	-2.13E-06	1.98	0.40	-0.74
75	-0.95	5.70E-06	-0.54	-2.65E-06	2.15	0.41	-0.74
100	-0.96	7.21E-06	-0.54	-3.46E-06	2.09	0.42	-0.75

In Table 3 are the E_p and i_p for each scan rate along with the peak ratios, i_{pc}/i_{pa} , the peak separation, ΔE_p and formal reduction potential, E° . At all scan rates i_{pc}/i_{pa} is much greater than 1. The ΔE_p is also between 0.32 V and 0.42 V. It would be expected the i_{pc}/i_{pa} ratio was close to 1 and the ΔE_p is 0.059 V for a fully reversible system. With the utilization of the irreversible

Randles-Sevcik in Equation 32, the diffusion coefficient was calculated for the 50, 75 and 100 mV scan rate trials. The overall average diffusion coefficient was calculated to be $2.4 * 10^{-11} \pm 0.5 * 10^{-11} \text{ cm}^2/\text{s}$.

The formal reduction potential is average between E_{pc} and E_{pa} . In this system it was found to be $-0.74 \pm 0.01 \text{ V}$ vs Ag/AgCl. In Table 4 are the standard reduction potentials for uranium as listed in the CRC as V vs SHE and vs Ag/AgCl to simplify the comparison to this data. The standard reduction potential for the U(IV)/U(III) couple is -0.774 V vs Ag/AgCl.⁸⁹ However, this is unlikely the resolved couple as these reduction potentials are completed in aqueous solutions. In an electrochemical study of a UF_6^- anion in [BMIm][TFSI] found the reduction to occur at -1.2 V vs Ag^+/Ag and showed spectroscopically the ingrowth of U(IV).¹¹⁸ This further shows the resolved couple in this work is the U(V)/U(IV) redox couple.

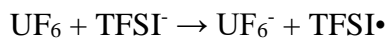
Table 4: Standard Uranium Reduction Potentials⁸⁹

Reaction	E° (V vs SHE)	E° (V vs Ag/AgCl)	U Oxidation Change
$\text{UO}_2^+ + 4\text{H}^+ + \text{e}^- \leftrightarrow \text{U}^{4+} + 2\text{H}_2\text{O}$	0.39	0.193	U(V) \leftrightarrow U(IV)
$\text{UO}_2^{2+} + 4\text{H}^+ + \text{e}^- \leftrightarrow \text{U}^{4+} + 2\text{H}_2\text{O}$	0.273	0.076	U(VI) \leftrightarrow U(IV)
$\text{UO}_2^{2+} + \text{e}^- \leftrightarrow \text{UO}_2^+$	0.16	-0.181	U(VI) \leftrightarrow U(V)
$\text{U}^{4+} + \text{e}^- \leftrightarrow \text{U}^{3+}$	-0.577	-0.774	U(IV) \leftrightarrow U(III)
$\text{U}^{3+} + \text{e}^- \leftrightarrow \text{U}_{(s)}$	-1.125	-1.322	U(III) \leftrightarrow U(0)

4.7 Proposed Mechanism for Reduction of U(VI) to U(V)

The reduction of U(VI) to U(V) during the dissolution of UF_6 into the $[\text{MPPi}][\text{TFSI}]$ is evident through the presented XAFS and UV-Vis data. The author proposes the mechanism for this reduction is through the oxidation of the $[\text{TFSI}]$ anion to a free radical. Previous work with CeCl_6^{3-} in 1-butyl-1-methylpyrrolidinium $[\text{TFSI}]$ showed it was possible to electrochemically produce CeCl_6^{2-} but the Ce(IV) was not stable in the IL.¹²⁷ Other studies have shown that the pulsed radiolysis of $[\text{MeBu}_3\text{N}][\text{TFSI}]$ with an accelerator resulted in solvated electrons through the formation of the TFSI^\bullet radical. The TFSI^\bullet did not readily recombine with the solvated electron but would often fragment further, allowing the solvated electron to be scavenged by other solutes in solution.¹²⁸ It has been theorized that radiolysis from spent nuclear fuel could result in solvated electrons from radicalized TFSI^\bullet or cation, $\text{MeBu}_3\text{N}^{2+\bullet}$ which could be further scavenged by dissolved species.¹²⁹ Finally, the oxidation of TFSI to form the radical TFSI^\bullet was also demonstrated electrochemically using a Pt electrode at 0.85 to 1.4 V vs Pt/Pt^{2+} . However, the exact potential was not determined using an internal standard for the quasi reference of Pt/Pt^{2+} . The study showed the radical TFSI^\bullet was relatively stable in the IL and that the system could be continued to be used for catalysis in its presence.¹³⁰

The current dissolution studies of UF_6 in ILs containing the $[\text{TFSI}]$ anion further confirm the species can be readily oxidized. It's proposed that the UF_6 is dissolved into neat $[\text{MPPi}][\text{TFSI}]$ in inert atmosphere through the reduction of U(VI) to U(V) by $[\text{TFSI}]$ to form the TFSI^\bullet . The data suggests that the limiting factor for dissolution will be based on the concentration of the $[\text{TFSI}]$ anion present in the IL. However, the stability of the radical may be sufficient to allow the system to be utilized further. The mechanism for the direct dissolution of UF_6 into IL to form the pentavalent UF_6^- species is provided in Equation 33.



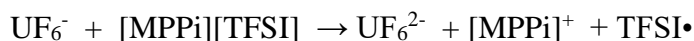
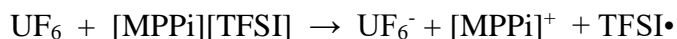
Equation 33: Proposed Mechanism for the Dissolution and Reduction of UF_6

4.7 Conclusions

This study is the first to evaluate the direct dissolution of UF_6 into an IL using the anion as a reducing agent. The dissolution occurs quickly through the reduction of the U(VI) to U(V) as UF_6 dissolves and forms UF_6^- . The UV-Vis and Raman prove the uranium is in the +5 state. The XAFS and UV-Vis data shows the U remains coordinated to six fluorides which is consistent with the formation of UF_6^- . The XAFS data shows the dissolved UF_6^- to be stable in the $[\text{MPPi}][\text{TFSI}]$ for up to 13 months.

Chapter 5. Recovery of Uranium Species from the IL

In the previous chapter the dissolution of UF_6 into $[\text{MPPi}][\text{TFSI}]$ was examined and the resulting products characterized. This chapter explores three different methods for recovery of the uranium species from the $[\text{MPPi}][\text{TFSI}]$. Recovery of the species through precipitation and electrochemical reduction are demonstrated. The dissolved uranium hexafluoride is precipitated from the $[\text{MPPi}][\text{TFSI}]$ over time as a salt of the UF_6^{2-} dianion that results from a second reduction of the initially produced UF_6^- . The following equations outline the direct precipitation through reaction and coordination with the IL cation. Specifically, the two-electron reduction of UF_6 and coordination with two cations occurs as the TFSI is oxidized to form the radical.



Or



The precipitation of uranium can also be accelerated with the addition of water and formation of hydrated uranium tetrafluoride. The processes is facilitated through the removal of two F^- into the aqueous phase which results in the precipitation and phase separation of the aqueous/solid/IL phases. These precipitates were characterized with PXRD and TGA. The heating of both of these precipitates in air results in the formation of uranium oxides.

The third method for recovery was electrochemical reduction of uranium to either metal or UF_4 depending on the IL utilized. This work was completed on a gold electrode. The deposits were examined by SEM-EDS.

5.1 Introduction

As mentioned previously in chapter 1, current methods for converting uranium hexafluoride to uranium oxides include the reaction of gaseous UF_6 with water vapor and H_2 to ultimately produce U_3O_8 and HF gas. In chapter 4, the dissolution and speciation of UF_6 dissolved in $[\text{MPPi}][\text{TFSI}]$ was characterized. Chapter 5 will examine the recovery of the uranium species from IL and previous literature for the same.

Several studies have shown ILs as effective extractants of uranium from aqueous solutions using traditional liquid-liquid extraction methods. In one study uranium was extracted from nitric acid solutions using 1-alkyl-3-methylimidazolium $[\text{TFSI}]$ ($[\text{C}_n\text{mim}][\text{TFSI}]$ where $n = 5-10$.) with TBP. It was found that at low acid concentrations (<0.1 M) $[\text{C}_5\text{mim}][\text{TFSI}]$ had a better distribution ratio, $D_u = [\text{U}]_{\text{org}}/[\text{U}]_{\text{aq}}$, by almost two orders of magnitude over $[\text{C}_{10}\text{mim}][\text{TFSI}]$. At high acid concentrations (>1 M) the two ILs behaved similarly. This shows the neutral $\text{UO}_2(\text{NO}_3)_2(\text{TBP})_2$ complex is easily extracted into the $[\text{C}_n\text{mim}][\text{TFSI}]$ regardless of alkyl length at high acid concentrations. However, the shorter alkyl chains make it easier for the ionic $\text{UO}_2(\text{TBP})_2^{2+}$ complex to be extracted into the IL at low acid concentrations with corresponding transfer of $[\text{C}_5\text{mim}]^+$ into the aqueous phase.¹³¹ Trihexyl(tetradecyl)phosphonium chloride was used for extracting $\text{UO}_2(\text{CO}_3)_2^{2-}$ from feed solutions of 1:5 $\text{UO}_2(\text{NO}_3)_2$ to Na_2CO_3 with a pH of 9.58. The uranium could then be stripped from the IL phase with 1M NaOH to produce a yellow precipitate.¹³² Another study compared the extraction of $\text{UO}_2(\text{NO}_3)_2$ from a nitric acid solution with the previously studied 1-butyl-3-methylimidazolium $[\text{TFSI}]$ ($[\text{BMIm}][\text{TFSI}]$) and 1.1 M TBP. They successfully extracted uranium into the organic phase and then completed electrodeposition of the uranium as UO_2 from the TBP/ $[\text{BMIm}][\text{TFSI}]$ mixture on a platinum electrode. This is possible because the TBP does not change the

electrochemical nature of the IL.^{133,134} A majority of work with uranium in ILs has been directed toward the potential use for the extraction of uranium oxides from spent nuclear fuel. Studies with uranium halides in ILs are limited.

Most of the work on uranium halide chemistry in ILs has been completed with UF₄ or UCl_x analogs. The fluorinated IL, [BMIm][PF₆], has been used to convert UO₂ to UF₄. The fluorination was completed by mixing 40 mg of UO₂ in 2 mL of [BMIm][PF₆] in a Teflon reaction cell and heating to 150 °C for 24 hours. This method could be used to replace the need for HF in the fluorination of uranium oxides, however, the oxidation state of uranium remains unchanged in this study.¹³⁵ The [BMIm][Cl] has been examined for use to decontaminate stainless steel used in UF₆ production. Initially UF₄ was dissolved in heated [BMIm][Cl]. UV-Vis showed the formation of UO₂Cl₄²⁻, indicating the oxidation of the U(IV) to U(VI) by O₂ present in the atmosphere. A stainless-steel sample was then exposed to the [BMIm][Cl] at 100 °C for three hours. XPS spectra showed UF₄, FeF₃ and Fe₂O₃ on the surface up to 25 µm of depth before treatment. After treatment the UF₄ and FeF₃ were no longer on the surface. In the dissolved solution the ratio of Fe³⁺ to F⁻ was 1:3 indicating only the fluorinated iron was dissolved. ILs could be an option for cleaning material contaminated with uranium fluorides and reduce the secondary waste stream produced in dissolving transition metals compared to acid treatments.¹³⁶ These studies did not outline a route for recovery of the uranium.

A handful of studies have been done with UX₆²⁻ salts where X is Cl or F. The [Cation]₂UCl₆ salts were made with both the [BMIm] and [MeBuN] cations. These complexes were made by dissolving U metal in 10 M HCl with a slight excess of [cation][Cl] and the uranium salt was precipitated. The salts were dissolved in their corresponding [cation][TFSI] ionic liquid. Spectroscopic data showed the stability of the U(IV) complex in their respective

ILs. With a glassy carbon working electrode both the oxidation and reduction of the U(IV) complex to the U(V) and U(III) were observed electrochemically.^{68,137}

In recent work, several [Cation][UF₆] ILs were synthesized ([EMIm], [BMIm], [BPy], and [BMPyr]). These were made by reacting an excess of anhydrous HF with [Cation][Cl] and removing the resulting HCl and excess HF with a vacuum. The resulting [cation](FH)_nF was reacted with β-UF₅ in a T-shaped PFA reactor. These reactions produced the green liquids identified as [Cation][UF₆] with the uranium in the +5 oxidation state. These compounds were characterized with Raman, FT-IR, electrochemically with cyclic voltammetry, and TGA/DSC.^{117,118} The initial step for the formation of these ILs was the production of the [Cation](FH)_nF ionic liquid. In more recent work the previously developed [EMIm][F(HF)_{2.3}] was tested for dissolution of UO₂ and UO₃. The dissolution was successful and initially ESI-MS and APCI-MS indicate the dissolved species to be UF₆⁻, suggesting the dissolved species to be U(V). Overtime the formation of UO₂F₂ is identified, likely due to oxygen slowly dissolving into the IL over time and oxidizing the UF₆⁻ anion.¹³⁸

Finally, some work has been done with the dissolution of uranium halides in ILs but not on the recovery of uranium halides from IL.^{68,116,137,139} In the previous chapter the dissolution of UF₆ in the IL was studied and the initial product characterized. In this chapter the recovery of uranium is carried out using three different methods of precipitation and electrochemically. The precipitates are characterized in this chapter.

5.2 Methods and Materials

5.2.1 Chemicals and Solutions

The 1-propyl-1-methylpiperidinium bis(trifluoromethylsulfonyl)imide 99% ([MPPi][TFSI]) purchased from IoLiTec. The UF₆ was natural uranium and supplied by

URENCO. Solutions were prepared utilizing the dissolution method outlined in Chapter 4. Water utilized during the precipitation was about 18.2 MΩ from a Barnstead E-Pure water filtration system.

5.2.2 Time Dependent Precipitation

The first recovery method was the time-dependent precipitation of a UF₆ salt. Higher concentration samples (>0.7 M UF₆) precipitated over a period of weeks. Lower concentration samples (<0.2 M UF₆) would precipitate over the course of several months. These samples were then collected through filtration using a simple paper filter, vacuum funnel, and filtration flask. The IL was collected from the flask and the precipitates were rinsed several times with acetone to remove the IL. The precipitates were then dried under vacuum in a desiccator overnight.

5.2.3 Water Driven Precipitation

The second recovery method was water-initiated precipitation. Approximately 3 mL of a 0.1 M UF₆ in [MPPi][TFSI] was placed in a 15 mL centrifuge vial. Then 3 mL of DI water was added to the centrifuge vial. The vial was capped and wrapped in parafilm. The vials were placed on a shaker table for 90 minutes to fully mix. They then were centrifuged for 5 minutes at 5000 RPM. Some precipitates were retained between the aqueous and IL phases and some were at the bottom of the IL. The aqueous and IL phases were removed separately using disposable pipettes. The remaining precipitates were filtered and rinsed with acetone as described previously.

5.2.4 Electrochemical Recovery

The electrochemical reduction was completed using a 760C Potentiostat by CH Instruments, Inc. Electrochemical deposition was completed with solutions of about 0.1 M UF₆. The counter electrode was a platinum sheet and the reference electrode was as described in chapter 2. The working electrode was a gold foil electrode. All electrochemical studies were

completed in a double wide MBraun glove box in dry inert atmosphere. The electrode was first cycled 20 times from 2 to -4 V at 100 mV/sec. This step is intended to create nucleation sites for deposits. Then deposition was completed by holding the electrode at -3.5 V for 20 to 40 hours.

5.2.5 Analysis Instrumentation

The SEM images of the uranium deposits were taken on a JEOL JSM6700F Field Emission SEM instrument without any additional surface pretreatment. The magnification range of 35 to 1200 times was imaged. The imaging conditions used a 15 kV accelerating voltage and a working distance of 22 mm. The gold electrode with deposits was dipped in acetone before being placed on the stage to remove the [MPPi][TFSI] from the electrode surface.

The PXRD patterns were collected using a Bruker D8 Advance powder x-ray diffractometer. The samples were ground using a mortar and pestle. Then sample was placed on a silicon low background stage. Sample was dispersed and adhered to the stage using methanol. The sample was then domed to prevent loss of loose material.

Thermal gravimetric data was collected with a Netzsch F1 Jupiter 43 simultaneous Thermogravimetric analysis and Differential Scanning Calorimetry (TGA/DSC) instrument. TGA was run on the precipitate from 20 to 1300 °C at 5 °C /min. There was also an Ar stream over the sample. The rate was reduced to a flow of 20 mL/min due to the precipitate being a powder. Measurements were carried out in an Al₂O₃ crucible with a lid. Sample masses were typically between 15 and 30 mg. The powders were placed into the crucibles and then were pressed into the bottom of the crucible to create a flat, packed sample.

UV-Vis spectra were obtained at room temperature with a Cary 6000i double beam spectrometer. The solid precipitates were mixed with mineral oil in a mortar and pestle.

FT-IR spectra were collected on a Varian 3100 FT-IR Excalibur series spectrometer with the Varian Resolutions Pro, version 5.04.009 software. IL solutions were measured by placing a small amount directly on the sample stage. Samples were disposed of afterwards due to their exposure to atmosphere.

Raman spectroscopy was completed in an inhouse sample holder with a sapphire window. The samples were sealed in inert atmosphere. The measurements were completed using 514.5 nm excitation line. The data was collected on a Princeton Instruments SP2750i spectrometer with a 1800 groove/mm holographic grating and a PIXIS 400 camera.

5.3 Time Dependent Precipitation of Uranium from IL

A 1 M high concentration solution was made to test the solubility limits of UF_6 into the $[\text{MPPi}][\text{TFSI}]$. It was noticed over time that dark precipitates were forming on the bottom of the vial which can be noted in Figure 43. UV-Vis of the same 0.1 M UF_6 solution presented in chapter 4 was taken at 156 days shown in

Figure 44. Over a short period of time as examined in chapter 4, the changes in the UV-Vis bands were minimal. However over extended periods the UV-Vis changes extensively over a broad spectral range. In the first week there were minimal changes, the maximum of the 1350 nm peak decreases over time. The shoulder of the absorption in the ultraviolet region shifts. The peak that at 600 to 800 nm remains relatively unchanged over the course of a week but changes greatly in intensity and peak shape over the course of months. The peak at 980 nm remains unchanged in the short term, but a new peak at 1110 nm grows over months. These changes indicate the likely change of oxidation state of the uranium from V to IV and the formation over time of the solid $[\text{MPPi}]_2[\text{UF}_6]$.

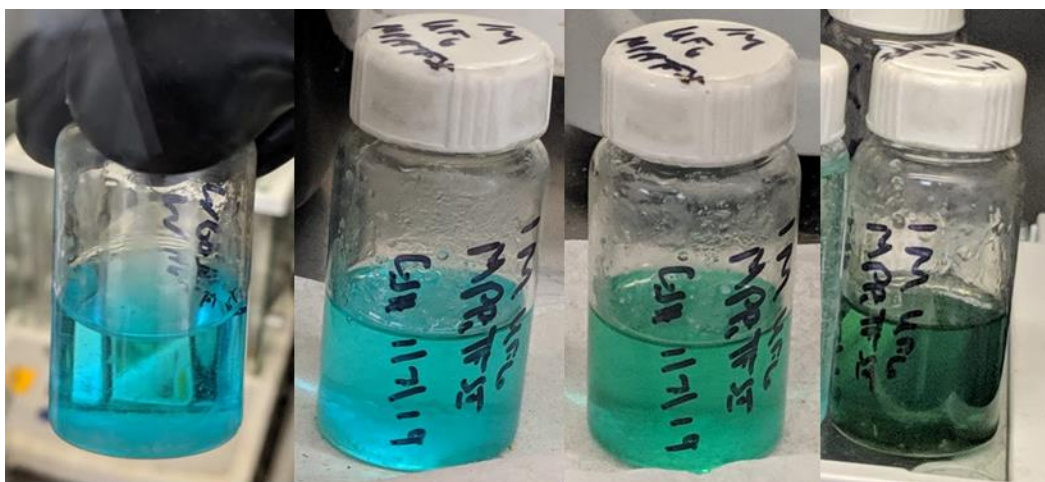


Figure 43: A 0.95 M UF_6 in IL freshly made, after 1 day, 8 days, and 49 days.

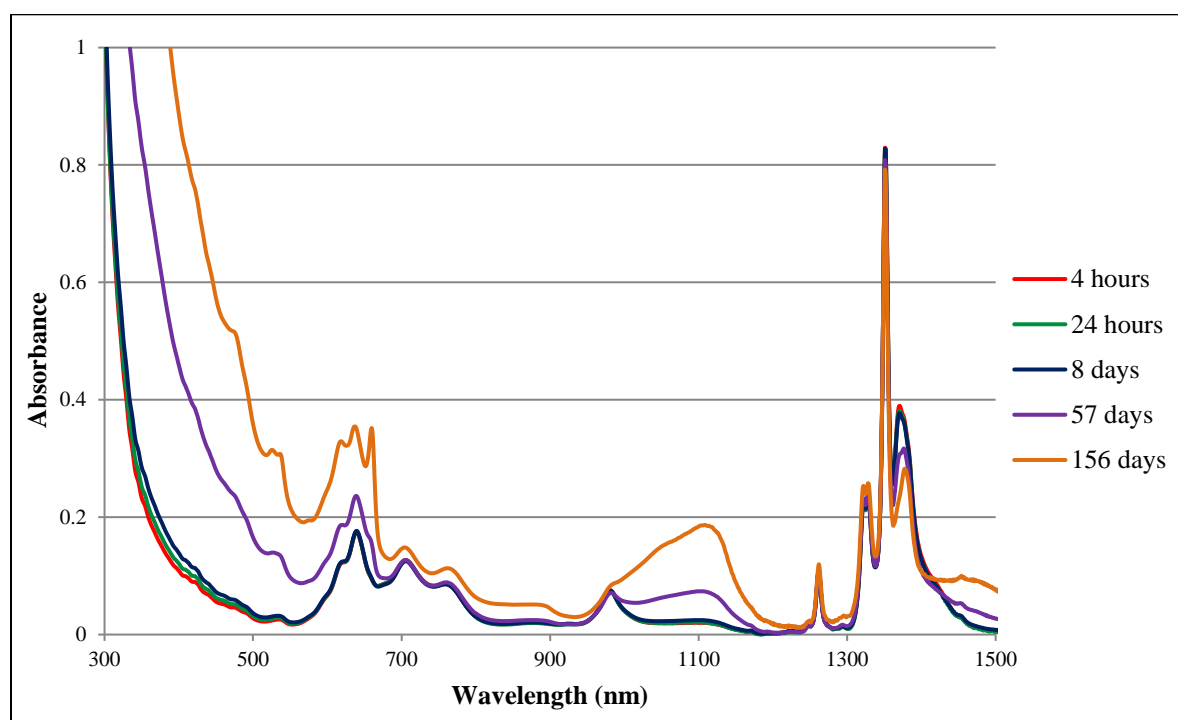


Figure 44: Changes in UV-Vis of 0.1 M UF_6 in $[\text{MPPi}][\text{TFSI}]$ over extended time.

Additionally, FT-IR was completed on solutions of various ages (Figure 45). In the short term of a week the FT-IR spectrum of a 0.1 M UF_6 solution looks similar to that of pristine $[\text{MPPi}][\text{TFSI}]$. When a 136-day 0.6 M UF_6 solution is measured there are two significant changes in peak shapes. A FT-IR peak around 1500 cm^{-1} corresponds to the C-H stretch in piperazine, a six-member ring with two NH groups in the 1 and 4 position. The peak at about 1475 cm^{-1} is likely the CH_2 groups adjacent to the N in the $[\text{MPPi}]$ cation. The peak at 900 cm^{-1} corresponds to the rocking of the methyl group attached to nitrogen. These changes are consistent with the slow precipitation of the UF_6 with the cation in solution. The results suggest that precipitation occurs slowly as the second reduction occurs forming $[\text{MPPi}]_2[\text{UF}_6]$. $[\text{MPPi}][\text{TFSI}]$ absorbs heavily in the UV range. The coordination results in the shift of the UV shoulder in the UV-Vis consistent with the interaction between the $\text{UF}_6^{\text{n-}}$ and $[\text{MPPi}][\text{TFSI}]$.

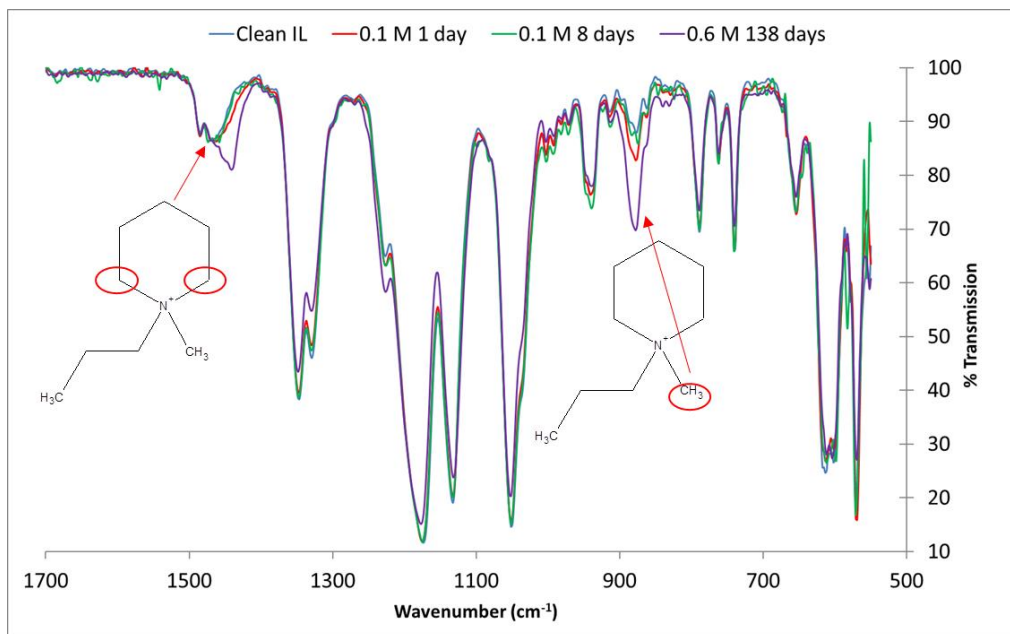


Figure 45: Changes in the FT-IR of a 0.1 M UF_6 solution over a week and a 0.6 M UF_6 solution at 138 days.

The long-term changes in the UV-Vis and FT-IR are indications of interactions between the $\text{UF}_6^{\text{n-}}$ anion and $[\text{MPPi}][\text{TFSI}]$ over time. These interactions are kinetically very slow, likely due to the bulkiness and asymmetry of the $[\text{MPPi}]$ cation and the viscosity of the solution. In chapter 4 the mechanism for a single electron transfer is shown. The following evidence shows a second electron transfer occurs to reduce the U(V) to U(IV). As the cations and the UF_6^{2-} interact, the bulky ionic compound precipitates out of solution. Allowing it to be filtered out and rinsed with acetone to remove the remain $[\text{MPPi}][\text{TFSI}]$. The dried precipitates are shown in Figure 46.

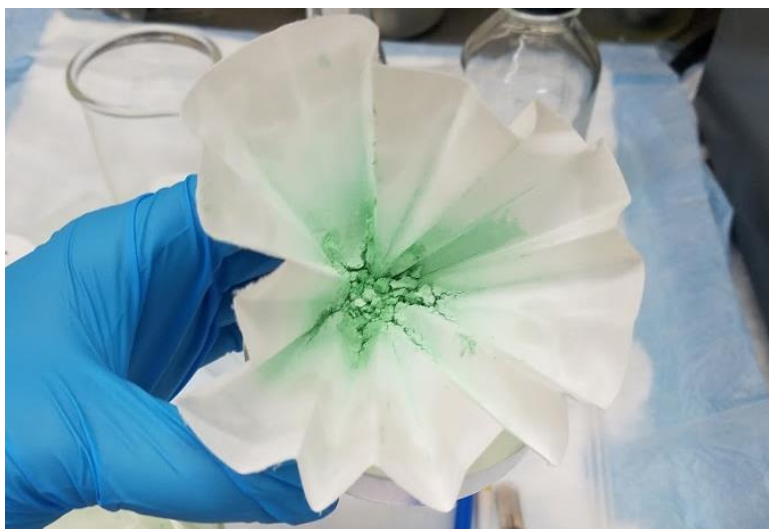


Figure 46: Solid precipitates collected from a 0.7 M UF_6 solution.

The first method of characterization completed with these precipitates was PXRD. The pattern has several peaks, but counts were very low, indicating the precipitates were not crystalline. Further analysis was completed using TGA (Figure 48). There are two major mass losses at 400 °C and 1100 °C. The initial mass loss at 400 °C was 42 to 44% for the samples. This corresponds to the loss of the 2 $[\text{MPPi}]$ cations equivalents to 44.7% mass loss. The second

mass loss at 1100 °C is 56 to 59% for the samples. The loss correlates with the removal of 6 fluorides and the addition of O₂ which has a mass equivalent to 57.6%. After running TGA/DSC, the sample was a black powder. PXRD of the powder shows it to be primarily UO₂ with some UOS as shown in Figure 49. In a tube furnace, larger samples have been heated with an argon stream to 1100 °C. Pure UO₂ has been collected from these samples and confirmed with PXRD (Figure 50).

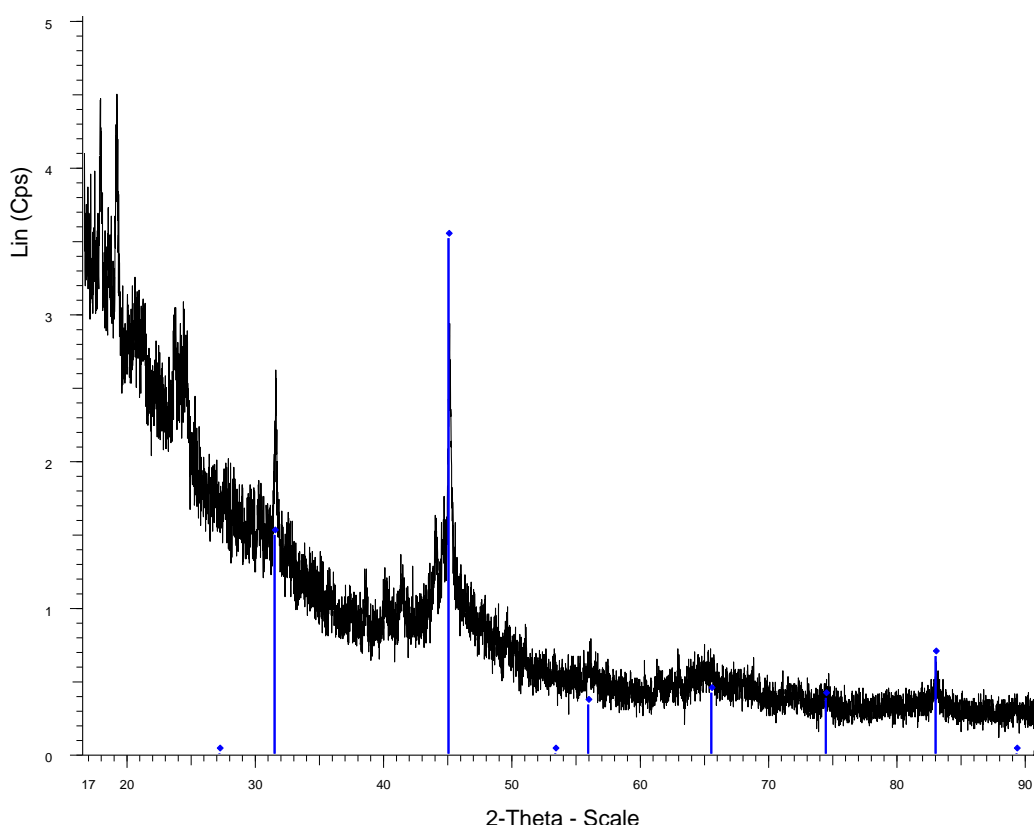


Figure 47: PXRD of UF₆ precipitate. In blue is the pattern for UF₄(H₂O)₂

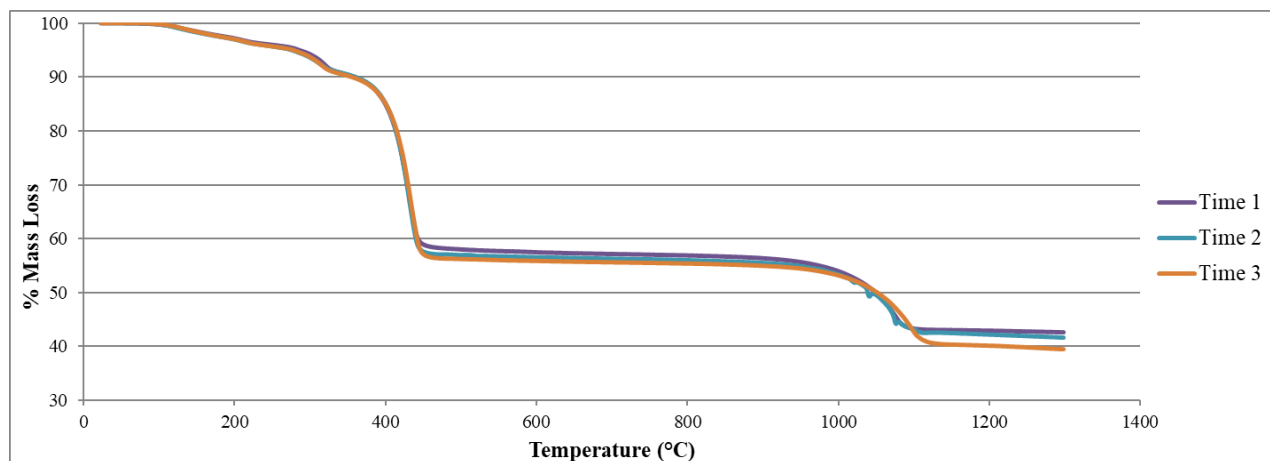


Figure 48: TGA of three separate samples of the precipitates that form over time.

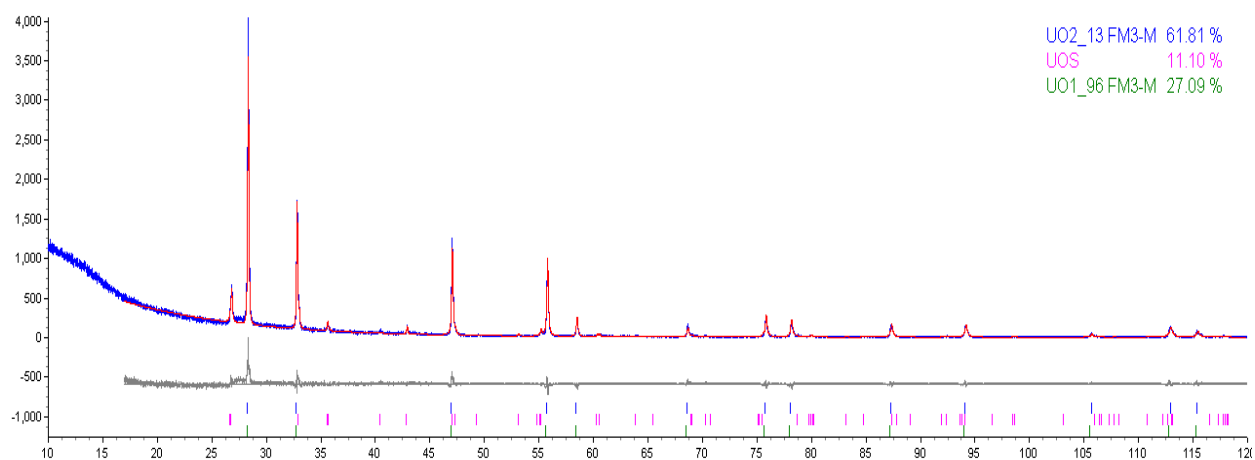


Figure 49: PXRD of time dependent precipitate after running TGA/DSC

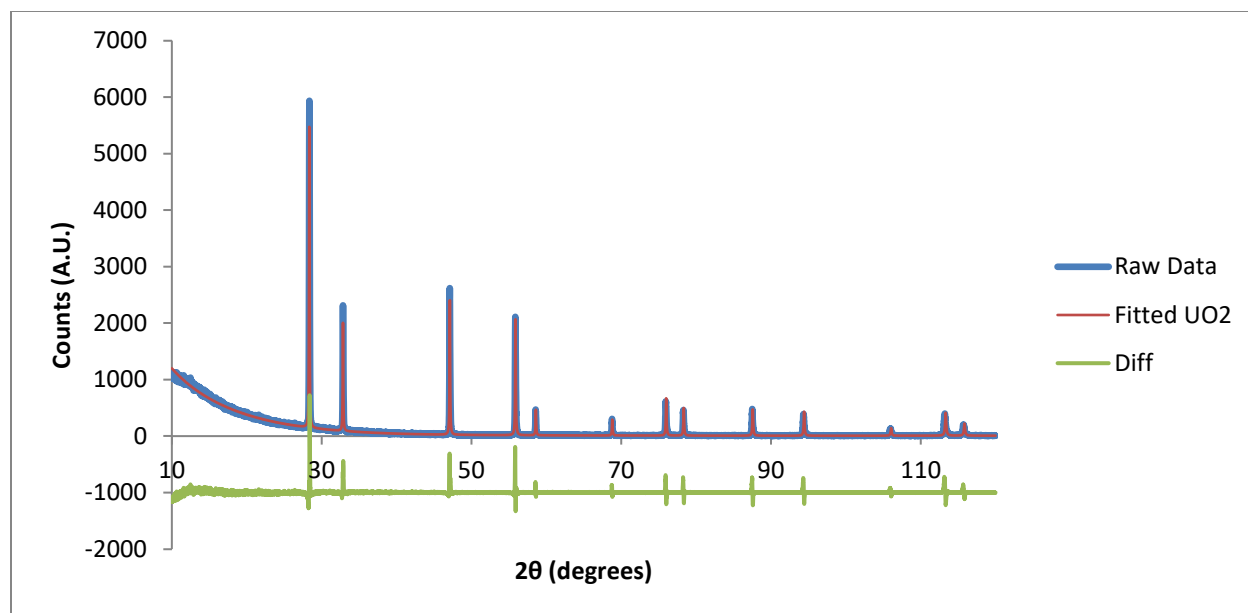


Figure 50: PXRD of sample after heating time dependent precipitate in tube furnace.

5.4 Water Driven Precipitation of Uranium from IL

It was discovered adding water to a low concentration UF_6 solution accelerated the formation of a precipitate. In a 15 mL centrifuge vial, 5.6 mL of the 0.0386 M UF_6 solution was combined with 4.4 mL of DI H_2O . The centrifuge was placed on a microplate genie and mixed for 1 hour. The mixture was then centrifuged for 15 minutes at 5500 rpm. A green solid precipitate was observed primarily at the bottom of the vial. There was a small amount of precipitate stuck in the layer between the water and $[\text{MPPi}][\text{TFSI}]$. The centrifuge tube before and after certification is shown in Figure 51.

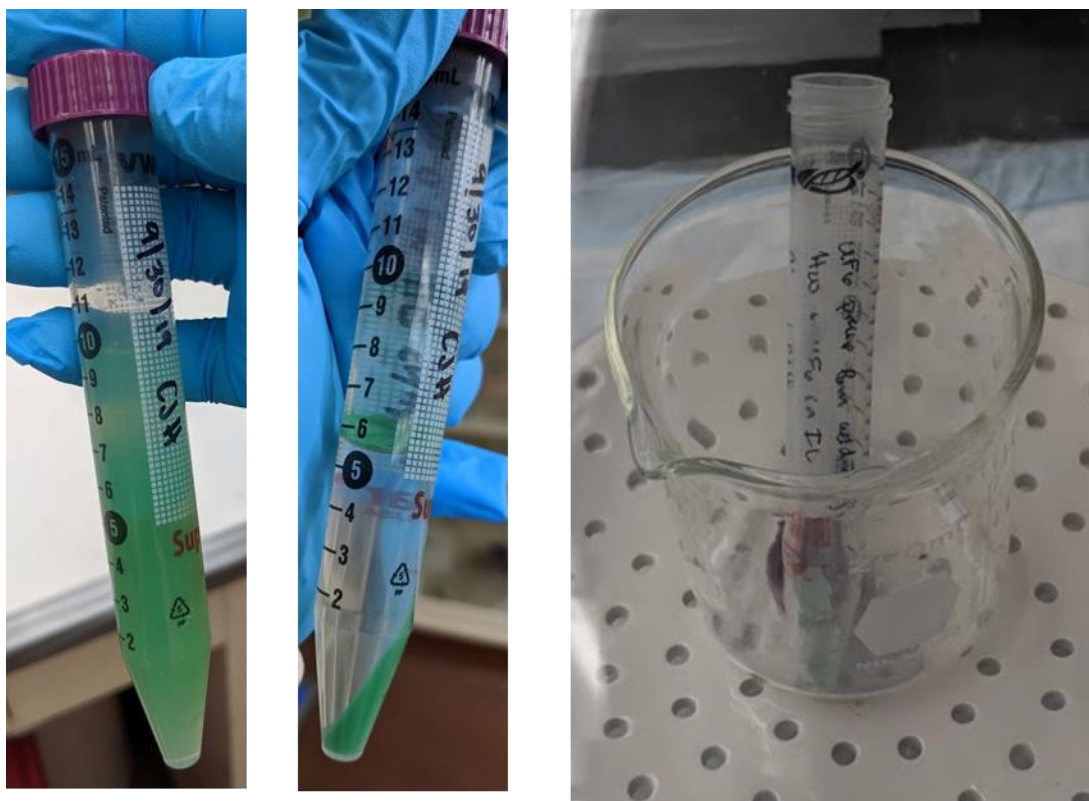


Figure 51: 5.6 mL of 0.04 M solution of UF_6 in $[\text{MPPi}][\text{TFSI}]$ with 4.4 mL of DI H_2O shaken by hand, centrifuged, solid filtered from solution.

The water layer and a majority of the $[\text{MPPi}][\text{TFSI}]$ was decanted from the precipitate at the bottom. The precipitate between the water and $[\text{MPPi}][\text{TFSI}]$ layers was lost. The precipitate was rinsed twice with hexane to remove the bulk of the $[\text{MPPi}][\text{TFSI}]$. Then the solid was mixed thoroughly with acetone and centrifuged three times to further remove any remaining $[\text{MPPi}][\text{TFSI}]$. The vial was placed overnight in the fume hood to dry. The mass of recovered precipitate was 0.2582 g. The vial and precipitate were further dried under vacuum in a desiccator, reducing the precipitate mass to 0.1183 g. The precipitate changed from a dark green to light green color when dried as shown in Figure 51.

The PXRD of the green precipitate shows the solid to be $\text{UF}_4 \cdot 1.5 \text{H}_2\text{O}$ (Figure 52). Using the initial solution concentration and volume there should have been 0.00022 mols of U available for recovery. Using the 0.1183 g and molar mass of $\text{UF}_4 \cdot 1.5 \text{H}_2\text{O}$, it was calculated that 0.00035 mols of U was recovered. Since this is 160% recovery, there is likely $[\text{MPPi}][\text{TFSI}]$ remaining in the precipitate. This will be shown later to be likely true through the Raman and FT-IR data of the two solid precipitates.

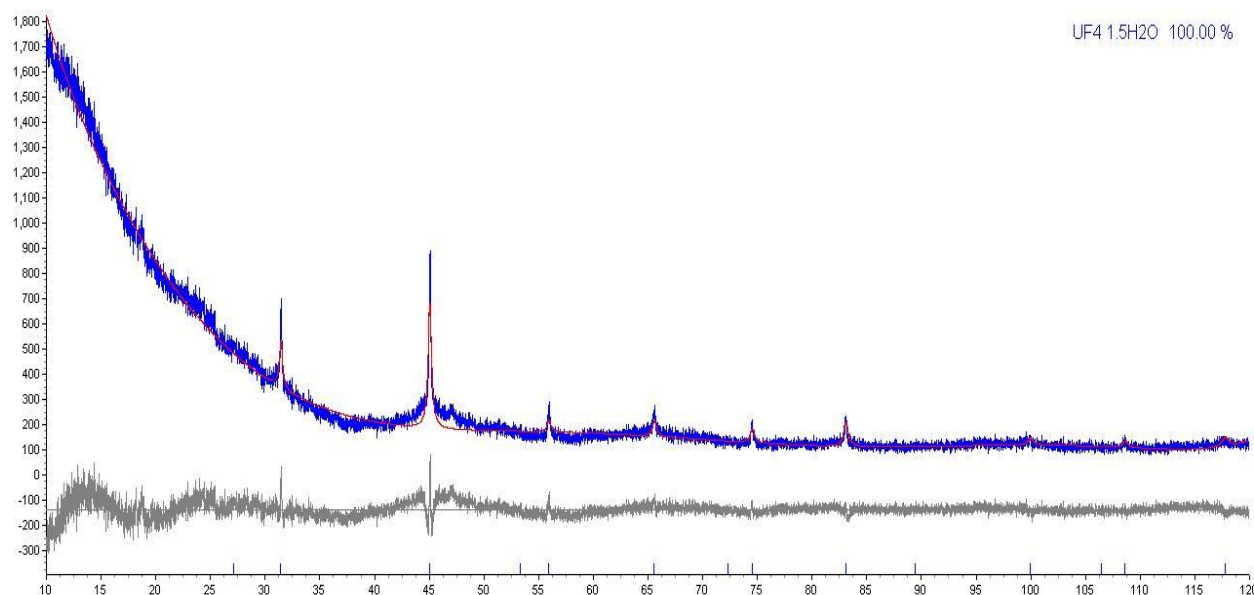


Figure 52: PXRD of UF_6 water driven precipitates fitted to $\text{UF}_4 \cdot 1.5(\text{H}_2\text{O})$

The TGA was completed on the water driven precipitates and is presented in Figure 53. The time precipitates experienced a total mass loss of about 55%. The water precipitates only experience a mass loss of about 24.5% over the same temperature range. As presented earlier in this chapter the time dependent precipitates' mass loss was equivalent to the loss of two of the $[\text{MPPi}]^+$ cations from the $[\text{MPPi}][\text{TFSI}]$ at 400°C and the exchange of 6 F with 2 O at 1100°C .

The PXRD of the water driven precipitates after TGA resulted in the production of U_3O_8 (Figure 54) instead of UO_2 . A more in-depth analysis of the TGA is present in section 5.5.

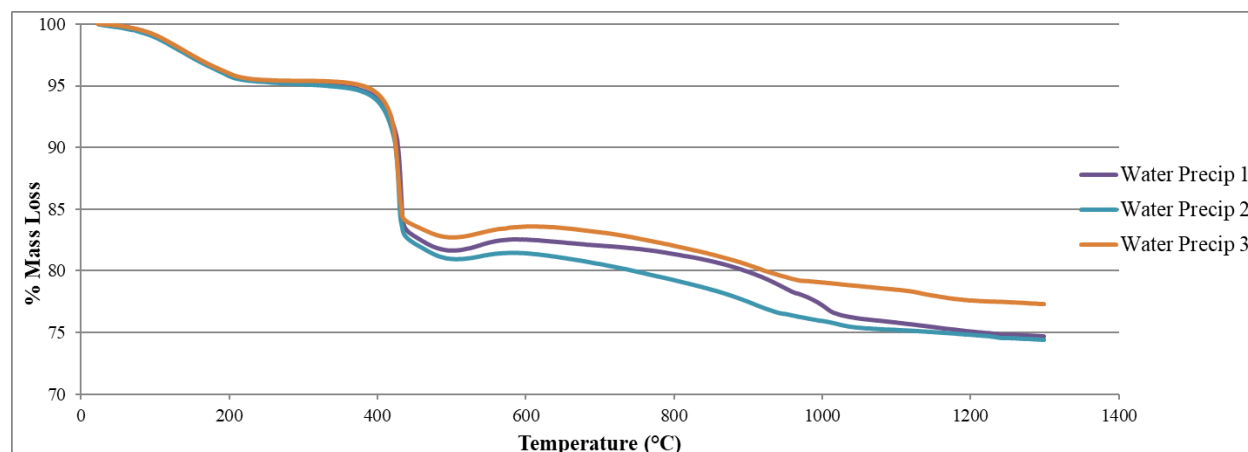


Figure 53: TGA results of the water-induced.

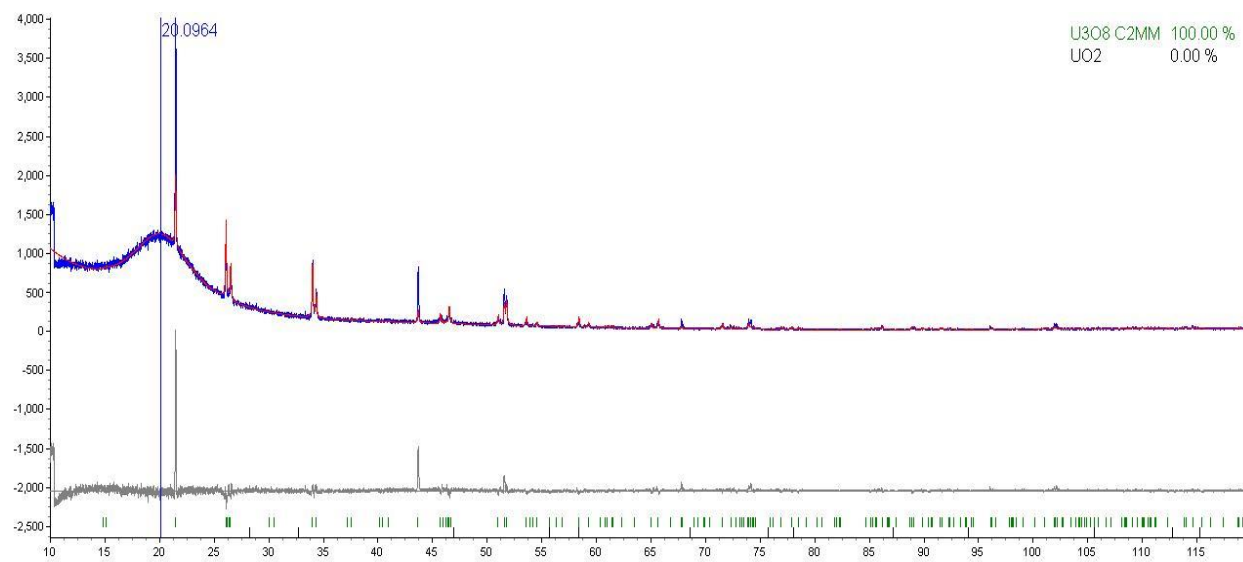


Figure 54: PXRD of water driven precipitates after running TGA/DSC

5.4.1 Mass Balance Studies for Uranium Recovery Utilizing Water

A mass balance was completed with two concentrations of solution, a lower 0.08 M and higher 0.26 M solution. Water extractions were also completed at 4 hours and 1 week after dissolution. The two concentrations and time periods were completed in duplicate. These time points were selected to see if the uranium could be recovered immediately after dissolution and at later dates if a sample was to be shipped and extracted at a different location. The longer aged solutions have more opportunity for the UF_6^- cation to be reduced and form a solid with the $[\text{MPPi}][\text{TFSI}]$.

The extraction was completed using 3 mL of UF_6 solution in $[\text{MPPi}][\text{TFSI}]$ and 3 mL of water. The mixture was shaken by hand vigorously for 2 minutes and then centrifuged. A majority of the IL and water was removed from the precipitate using a pipette. The aqueous phase was further diluted for ICP-AES analysis. The water phase changed to a yellow tint as previously reported. The UV-Vis was completed on one of the aqueous phases and presented the characteristic UO_2^{2+} five peak signature (Figure 55). The most likely species is $\text{UO}_2\text{F}_n^{(n-2)}$.

A second extraction was completed with water and the IL to evaluate U remaining in IL. A 3 mL sample of water was added to the 1.5 to 2 mL of IL that was separated using the pipette. The two phases were mixed on a shaker table for 90 minutes to complete the second extraction. This water was collected and evaluated on ICP-AES.

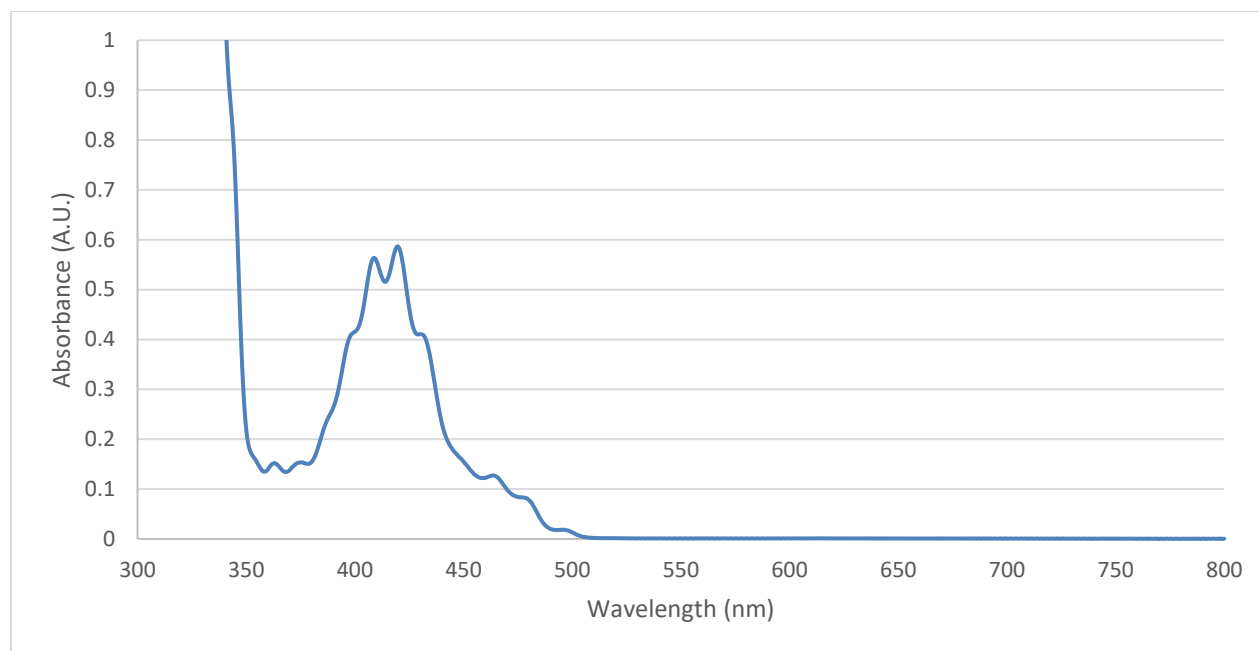


Figure 55: UV-Vis of aqueous phase after extraction of uranium

Table 5: Mass Work Up for Uranium Recovery for 0.26 M and 0.08 M Uranium at 4 hours and 1 week after addition to the [MPPi][TFSI].

Sample	% U in Aqueous Phase	% U in IL	% U Solid Precipitate
A) 0.26 M UF ₆ 4 hours	23.7%	0.2%	76.1%
B) 0.26 M UF ₆ 4 hours	25.4%	0.1%	74.4%
C) 0.26 M UF ₆ 1 week	28.7%	0.4%	70.9%
D) 0.26 M UF ₆ 1 week	26.3%	0.2%	73.5%
E) 0.08 M UF ₆ 4 hours	23.8%	0.2%	76.1%
F) 0.08 M UF ₆ 4 hours	26.8%	0.2%	73.0%
G) 0.08 M UF ₆ 1 week	27.9%	0.2%	71.9%
H) 0.08 M UF ₆ 1 week	28.0%	0.3%	71.7%

The results of the extraction in the phases are shown in

Table 5. It was found across all samples that about a quarter of the uranium was dissolved into the water during the extraction. There was little difference between the samples in concentration or in age of the sample. The aged 1-week samples had slightly higher percentages of U lost to the aqueous phase, $27.7 \pm 1.0\%$ vs $24.9 \pm 1.5\%$. The small sample sets overall make this a rather insignificant difference. It was also found that very little of the U ($< 0.5\%$) remains in the [MPPi][TFSI] after extraction but there were trace amounts found.

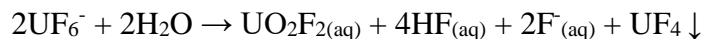
This study was repeated with 4 samples of 0.1 M solution aged 4 days after dissolution. In this set up about 3.5 mL of UF_6 solution was mixed with 4 mL of DI H_2O . The same procedure for mixing was repeated. The secondary extraction was not completed on the [MPPi][TFSI] because it was shown to be $< 0.4\%$ U remained in the [MPPi][TFSI]. This study presented similar results to the previous shown in Table 6. Similarly, about $25.3 \pm 2.6\%$ of the uranium was lost to the aqueous phase.

Table 6: Uranium Recovery for 0.11 M UF_6 at 4 days after addition to the [MPPi][TFSI].

Sample	% U in Aqueous Phase	% U Solid Precipitate
I	24.6%	75.4%
J	23.2%	76.8%
K	24.2%	75.8%
L	29.0%	71.0%
Average	25.3%	74.7%
Standard Deviation	2.6%	2.6%

The most likely chemical reaction for the water driven precipitation is shown in Equation 34. However, this reaction would produce a 1:1 ratio of uranium in the aqueous phase and the precipitate. Since we know this ratio is more heavily leaned toward the precipitate, the reduction

of the precipitated uranium is shared between the oxidation of the uranyl uranium and electrons further donated by the [TFSI] anion.



Equation 34: Chemical reaction for the water driven precipitation.

5.4.2 Optimization Study for Uranium Recovery Utilizing Water

In previous studies the volume of water and solutions were a similar 1:1 ratio with solutions varying from concentration of 0.07 to 0.26 M UF_6 . It was investigated if the amount of water used to perform the precipitation could be minimized to reduce the amount of uranium lost to the aqueous phase (previous reported to be about 25%). In this study water spikes of volumes of 3 μL , 30 μL and 300 μL were added to 3 mL of 0.23 M UF_6 in [MPPi][TFSI] in duplicates. The samples were on a shaker plate for 90 minutes and then centrifuged. All samples have precipitates (Figure 56), but the 3 and 30 μL spikes had a green tinge remaining in the [MPPi][TFSI].



Figure 56: The two tubes on the left received a 3 μL spike of water, the middle two received a 30 μL spike of water and the right two received a 300 μL spike of water.

The $[\text{MPPi}][\text{TFSI}]$ was removed from the precipitate and rinsed with acetone, a gelatinous material remained instead of a powder (Figure 57). The gel also appeared to be slightly soluble in acetone as the color of the filtrate was green. Once dried overnight in a desiccator under vacuum the gel turned to a dark green color and is more solid. These vials are shown to the left side of the photo in Figure 58.



Figure 57: Gelatinous material produced from 3 and 30 μL spikes. Pictured is a 3 μL sample.



Figure 58: On the left are the vials of dried gel from the two 3 μL (top) and two 30 μL (bottom).

A secondary extraction was completed on the [MPPi][TFSI] phase removed from the precipitate. In this extraction 3 mL of DI H₂O were added to each sample. The samples were mixed on the shaker table for an additional 90 minutes and then centrifuged. The resulting samples are shown in Figure 59. There was a small amount of additional precipitate in the bottom of the 3 and 30 μ L spiked samples and no additional precipitate in the 300 μ L sample. The water of the first two sets of samples were also a yellow/green color. The extraction method for uranium from [MPPi][TFSI] up to at least 0.23 M UF₆ can be completed with a 1:100 ratio of volumes of aqueous to IL phase. However, ratios at 1:100 and below are not sufficient for fully converting the UF₆⁻ to UF₄.



Figure 59: On the right are the [MPPi][TFSI] samples after the secondary 3 mL water extraction with the samples from top to bottom in sets of two, 3 μ L, 30 μ L, and 300 μ L initial water spikes.

5.5 Spectral Characterization of Precipitates

UV-Vis of the two precipitates were taken in mineral oil. The samples were placed between two quartz slides and loaded into the solid sample holder. UV-Vis of [MPPi][Cl] was also taken as reference for the [MPPi]₂UF₆. The UV-Vis of all three are shown in Figure 60. The cation has no significant absorbance bands between 300 and 1800 nm. All absorbance bands from the precipitates are from the uranium. The water driven precipitates, hydrated UF₄, has more defined absorbance bands than those of the [MPPi]₂UF₆, but they have the same peaks. The main peaks are at 421, 475, 536, 637, 660, 806, 1060, 1106, and 1455 nm. The absorbances in the 421 to 660 nm range are from the $5f^2 \rightarrow 5f^16d^1$ excitations.^{140,141} The lower energy transitions are the excitations from the ³H₄ ground state to excited states.¹⁴¹ Based on literature assignments for UX₆²⁻ (X=Cl, Br, I) these include the $\Gamma_7 \rightarrow \Gamma_6$ at 806 nm, $\Gamma_7 \rightarrow \Gamma_8'$ at 1060 and 1106 nm, and the $\Gamma_7 \rightarrow \Gamma_7'$ at 1455 nm. The splitting of the $\Gamma_7 \rightarrow \Gamma_8'$ is an indication of the deviation from octahedral conformation.¹⁴² Because the hydrated UF₄ ranges from 1.5 to 2 H₂O per U it makes sense that this sample exhibits more splitting than the ionic [MPPi]₂UF₆ complex.

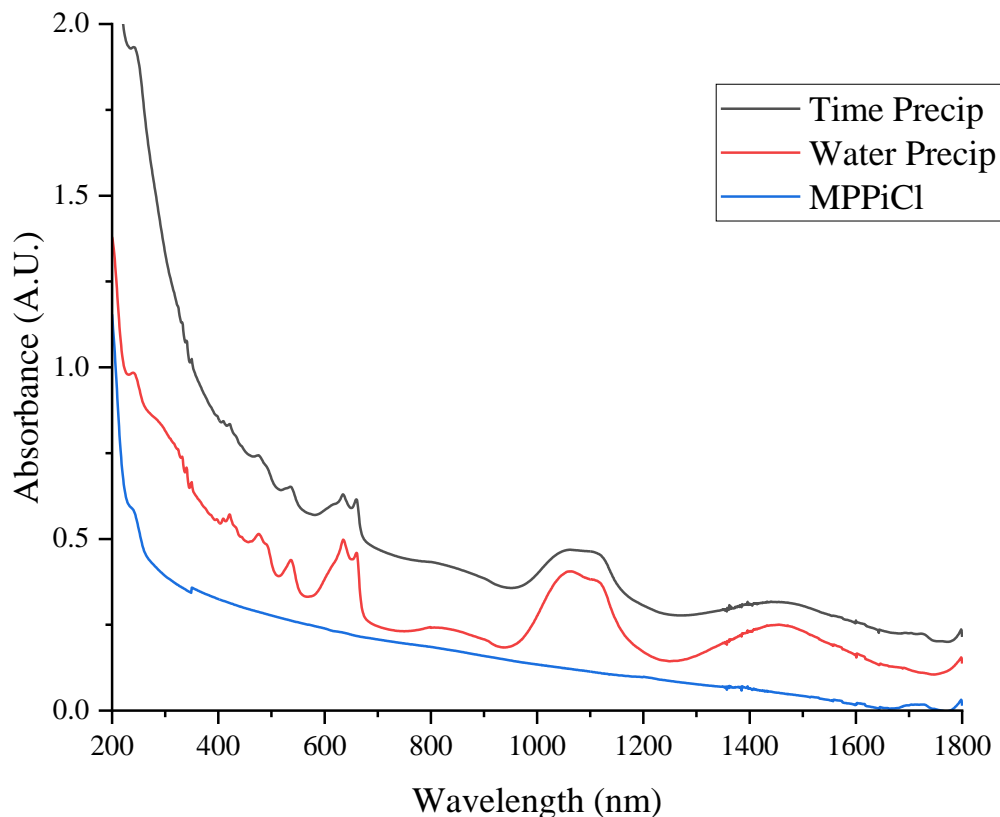


Figure 60: UV-Vis of the time dependent, water driven precipitates and [MPPi][Cl].

In Figure 61 is the FT-IR spectra of the two precipitates and [MPPi][Cl]. Both precipitates have a peak at 3300 and 1600 cm^{-1} indicating both precipitates are hydrated.¹⁴³ Compared to literature of UCl_6^{2-} complexes with several common IL cations, the signature between 2600 to 3000 cm^{-1} is from the piperidinium ring.¹³⁷ This signature region is found in both precipitates, indicating some of the IL remains as an impurity in the water driven precipitates. All vibrational frequencies for uranium in UF_6^{2-} are below the limits of the FT-IR used in this work.¹⁴⁴ In Table 5 is a comparison of the highest intensity peaks from the precipitates with [MPPi][Cl] and HTFSI. The peaks of interests are also labeled in Figure 61. The resolution of the instrument was 4 cm^{-1} to improve signal when collecting the spectra. Only the doublet D in the precipitates may be present in the HTFSI spectra. The separation between

these two peaks in the precipitate is 50 cm^{-1} and in HTFSI it is 85 cm^{-1} . With the 4 cm^{-1} resolution the only significant peak shifts for the vibrations labeled B and F. At vibration B both precipitates were at 1465.9 cm^{-1} while [MPPi][Cl] was at 1456.3 cm^{-1} . This peak is likely a contribution of the C-H adjacent to the nitrogen of the piperidinium ring as shown to change in the solution FT-IR in section 5.3. The doublet at F had one peak at 943.2 cm^{-1} for the precipitates and 939.3 cm^{-1} which is within the resolution of the instrument. The second peak is at 968.3 cm^{-1} for the time dependent precipitates, 964.4 cm^{-1} for the water driven precipitates, and 977.9 cm^{-1} for [MPPi][Cl]. These vibrations are likely from the methyl group off the nitrogen of the piperidinium, similar to the changes noted in the solution FT-IR. Because these shifts happen in both the time dependent and water driven precipitates, there is likely some [MPPi] associated with the uranium in the water precipitates as well as UF_4 present.

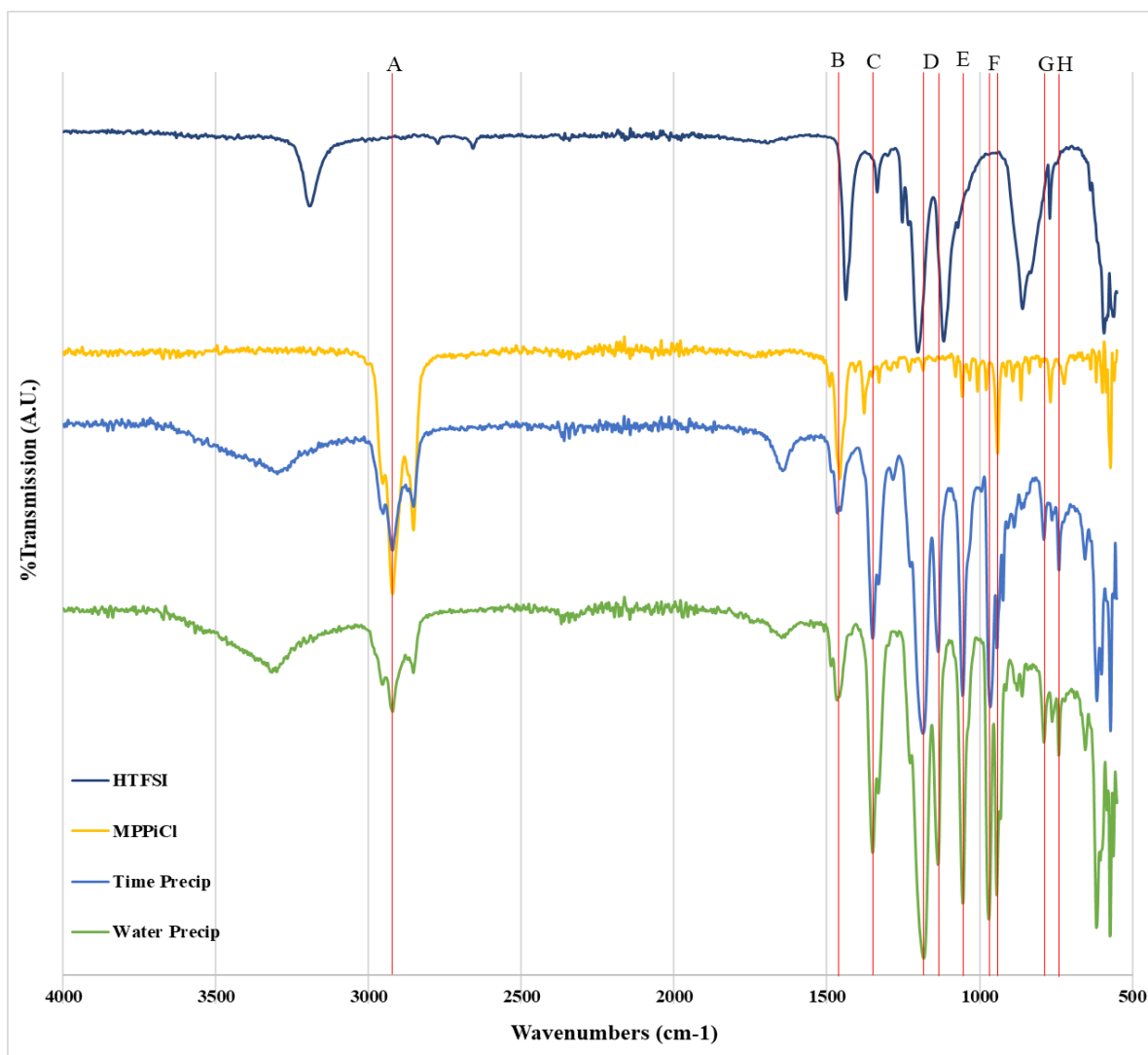


Figure 61: FT-IR Spectra of HTFSI, [MPPi][Cl], time dependent and water driven precipitates.

Table 7: Comparison of FT-IR peaks marked in red in Figure 61. All peaks are in cm^{-1} .

Instrument resolution was 4 cm^{-1} .

Peak	HTFSI	[MPPi][Cl]	Time Precip	Water Precip
A	-	2920.2	2922.1	2920.2
B	-	1456.3	1465.9	1465.9
C	-	1352.1	1350.2	1350.2
D	1201.6	-	1184.3	1182.4
	1116.8	-	1134.1	1136
E	-	1057	1055.1	1055.1
F	-	977.9	968.3	964.4
	-	939.3	943.2	943.2
G	-	-	788.9	788.9
H	-	-	738.7	740.7

Raman of the solid time dependent and water driven precipitates were collected from 100 to 1500 cm^{-1} (Figure 62). The solids were loaded into the sample holder as the solutions in chapter 4. There was no mineral oil added. Also plotted on Figure 62 is the [MPPi][TFSI] normalized to the 740 nm peak of the [MPPi][TFSI] with the 742 peaks of the time dependent and water driven precipitates. There are three main features in the precipitates that are not in the [MPPi][TFSI] at 188, 248, and doublet at 858 and 872 cm^{-1} for the time dependent precipitates and 181, 248, 858 and 872 cm^{-1} . The Raman active vibrations for UCl_6^{2-} has been reported for Cs_2UCl_6 and $[(\text{CH}_3)_4\text{N}]_2\text{UCl}_6$.¹⁴⁵ These are listed in Table 8. The 188/181 cm^{-1} peak is tentatively assigned to the ν_2 mode and the 248 cm^{-1} peak is assigned to the ν_1 mode. The 858 and 872 cm^{-1} doublet was not identified in the literature. In another study, the larger Br compound had a higher vibrational frequency than the Cl compound.¹⁴⁴ Therefore it can be inferred that the even smaller F compound would have an even lower vibrational frequency. The ν_5 mode was not observed in this work possibly because Raman data was not collected below 100 cm^{-1} .

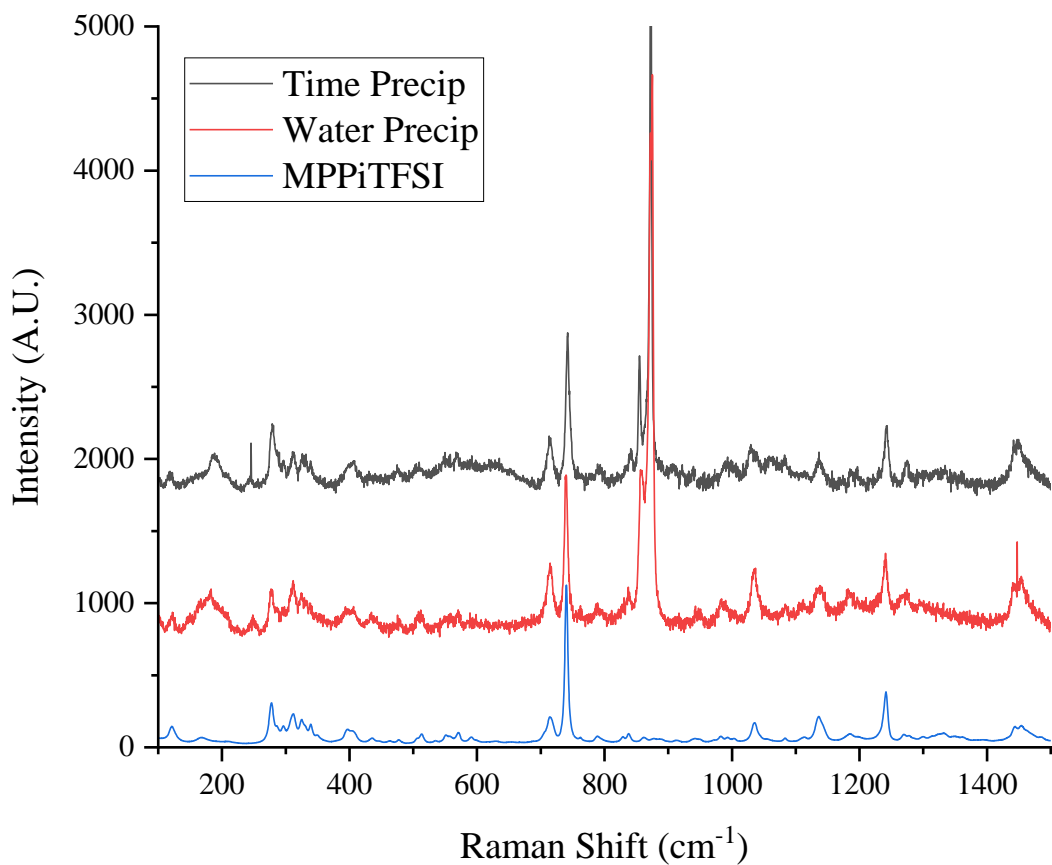


Figure 62: Raman of the time dependent and water driven precipitates with [MPPi][TFSI].

Table 8: Possible vibrational frequency assignments for the time and water driven precipitates compared to UCl_6^{2-} compounds in literature. All values are in cm^{-1} .

Designation	$\text{Cs}_2\text{UCl}_6^{145}$	$[(\text{CH}_3)_4\text{N}]_2\text{UCl}_6^{145}$	$\text{UCl}_6^{2- 144}$	$\text{UBr}_6^{2- 144}$	Time Precip	Water Precip
ν_1	308	296	404	371	248	248
ν_2	230	230		308	188	181
ν_5	126	124	162	170		

The FT-IR and Raman data suggest there is remaining cation in the water driven precipitate as well as likely some TFSI anion. It was also shown that both samples contain water.

Here we go into a more in-depth analysis of the TGA after knowing this data. In Figure 63 the average TGA of the two precipitates. The time dependent precipitates are shifted down by 10% on the y-axis to separate the two sets of data. Different temperature ranges are listed for each dataset. The final mols of U were calculated for each dataset using the final masses and the compound formulas of UOS for the time precipitates and U_3O_8 for the water precipitates.

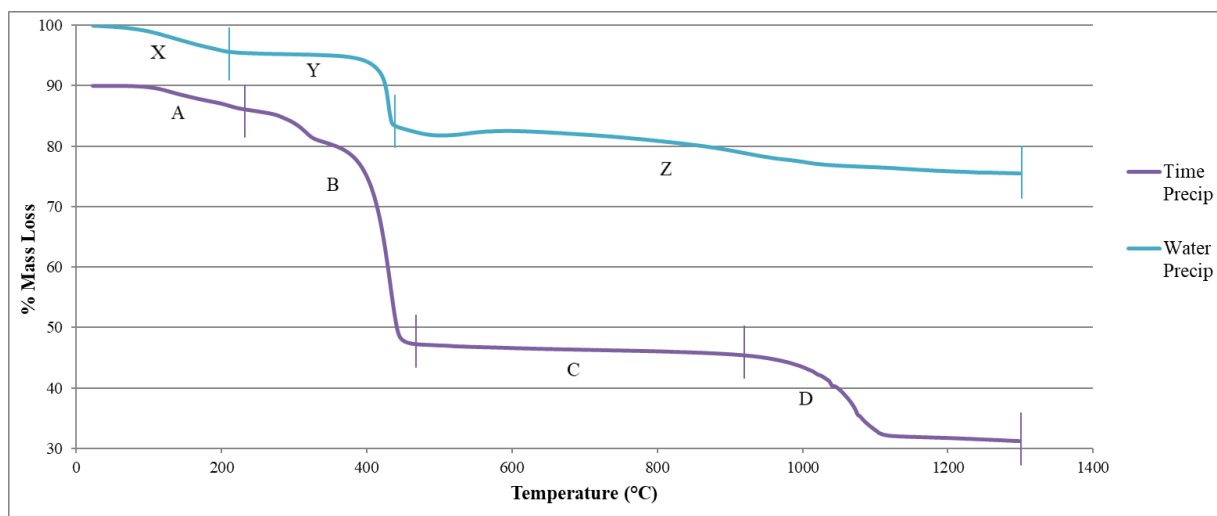


Figure 63: Averaged TGA mass losses for the time and water precipitates with labeled temperature ranges.

The first mass loss in the time precipitates is 4.05 % over the range of 23 to 240 °C, marked as region A. This is attributed to water and results in a 1:1.56 U to H_2O ratio. The mass loss from 240 to 470 °C shown as range B is 38.71 % with a U:[MPPi] ratio of 1.89. A mass loss of 1.88 % continues to occur from 470 to 925 °C. The last major mass loss in range D is 14.12 %. The melting point of UF_4 is 1036 °C. When the melting occurs is likely when the F to O exchange occurred. In the PXRD of the post TGA samples showed UOS with S from likely

remaining TFSI. When completed in a flowing air system of the clam furnace, UO_2 was produced. Based on the moles of U calculated in the final mass and original mass, a mass loss of 9.46 % would be expected in range D. This value is considerably less than 14.12 % mass loss. More work is necessary in cleaning up the precipitates and determination of impurities.

A mass loss of 4.47% over range X of the water precipitates from 23 to 220 °C is contributed to the water in the sample. This calculated out to a 1:0.92 ratio of U:H₂O for these samples. The mass loss of 12.23 % over range Y to 440 °C is attributed to any remaining cation or [MPPi][TFSI] remaining in sample. This is inferred since [MPPi][TFSI] was reported by Io-Li-Tec that thermal degradation occurs over 250 °C. The mass loss of 7.85 % over range Z is the conversion of UF_4 to U_3O_8 . Based on the final mols of U in the samples it was calculated this mass loss would be 8.96 %. The actual change was less than that of the calculated change. This could be explained if some of the water precipitates were still $[\text{MPPi}]_2[\text{UF}_6]$ instead of hydrated UF_4 or a mixture of F and [MPPi].

5.6 Electrochemical Recovery of Uranium from IL

In previous sections it was shown that the precipitates collected could be easily converted to uranium oxides by heating in air. A possible route for recovery of uranium metal is through the reduction of the uranium electrochemically. In chapter 4 the UF_6 in [MPPi][TFSI] was evaluated using a glassy carbon disc electrode to reduce the interactions between the electrode and the [MPPi][TFSI]. A gold foil electrode was used during the deposition due to the improved electron transfer kinetics between the electrode and uranium species.

Deposition exhibited here was of a 1-week-old 0.082M UF_6 in the [MPPi][TFSI]. The CV from 2 to -4 V on gold foil prior to deposition is shown below in Figure 64. Several peaks grow in overtime as observed on the glassy carbon electrode in chapter 4. After running CV,

deposition was run at -3.5 V for a total of 40 hours. Before and after photos of the cell are shown in Figure 65. There is a clear view of darker deposits forming during the deposition and in the final photos of deposition at 40 hours.

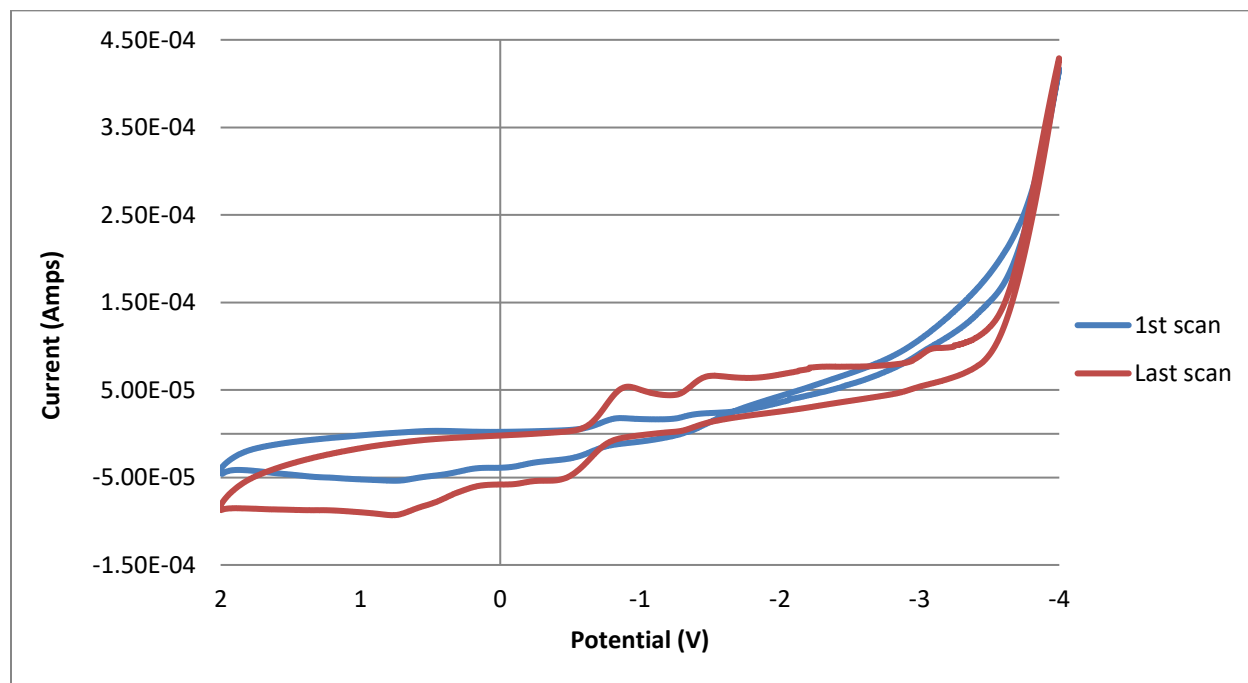


Figure 64: Cyclic voltammetry of the 0.082 M UF_6 in $[\text{MPPi}][\text{TFSI}]$ on gold foil electrode.

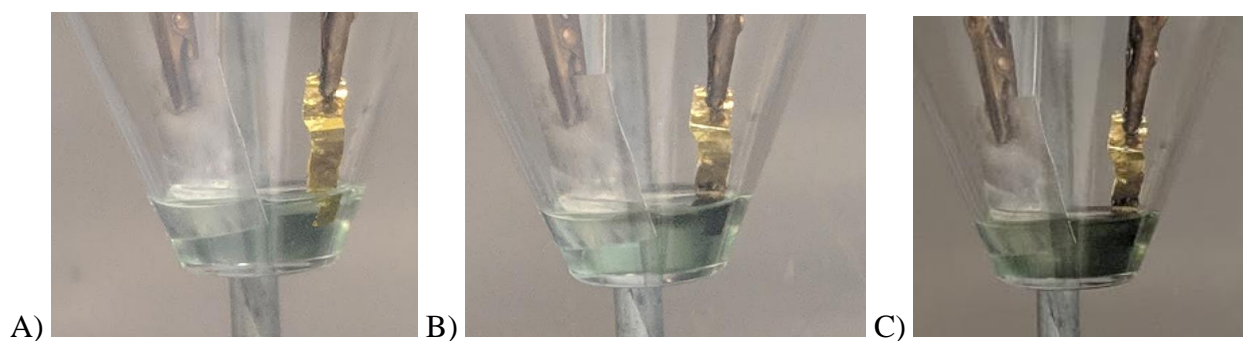


Figure 65: A) A photo of the cell before deposition began, B) after 20 hours of deposition, and C) is after the final 40 hours of deposition at -3.5 V.

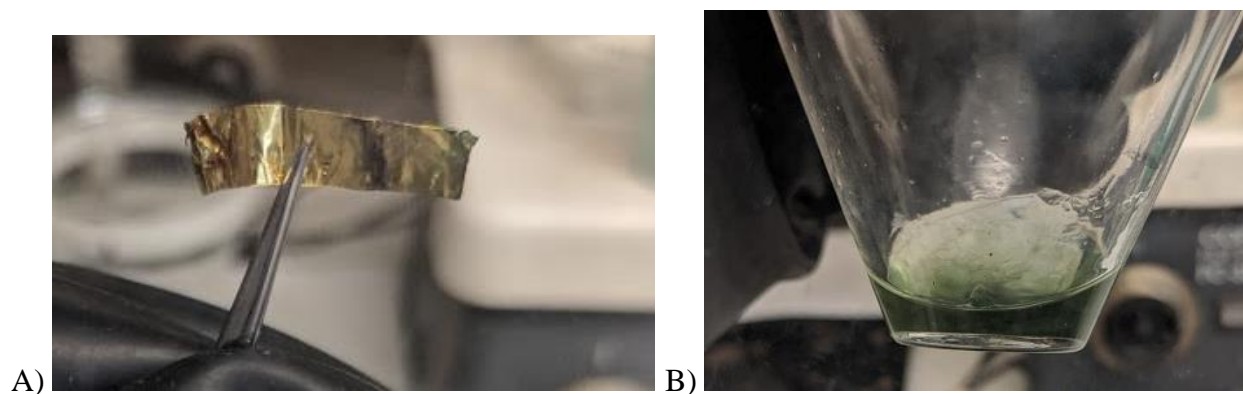


Figure 66: A) the electrode after being removed from the IL. B) the solution remaining in the cell with the deposits.

Following the deposition, the electrode was removed to complete SEM-EDS to look for U-metal deposits. A bulk of the deposits were not adhered well to the gold foil and remained in the IL once the cell was removed from the stand as shown in Figure 66. SEM images were initially taken of the gold electrode with IL on the electrode but the IL made it difficult to take images as it tended to move under the electron beam. The electrode was dipped in acetone four times and allowed to dry. Figure 67 are some of the images collected on the electrode after being dipped at 1500x magnification. In Figure 68 is an image of a site on the electrode where point EDS was completed to identify the deposits. The x-ray emissions indicate the presence of uranium, fluoride, and some sulfur. The sulfur, and potentially some fluoride, is likely from residual IL on the electrode. Atomic percentage of F:U was compared from the four point EDS spectra in Figure 68 and was found to be 4.8 ± 1.3 . If spectrum 2 was excluded it was found to be 4.2 ± 0.5 F per U. Accounting for residual [MPPi][TFSI] on the electrode as shown with the S present in the spectra, this ratio would indicate the deposition of UF_4 and not uranium metal.

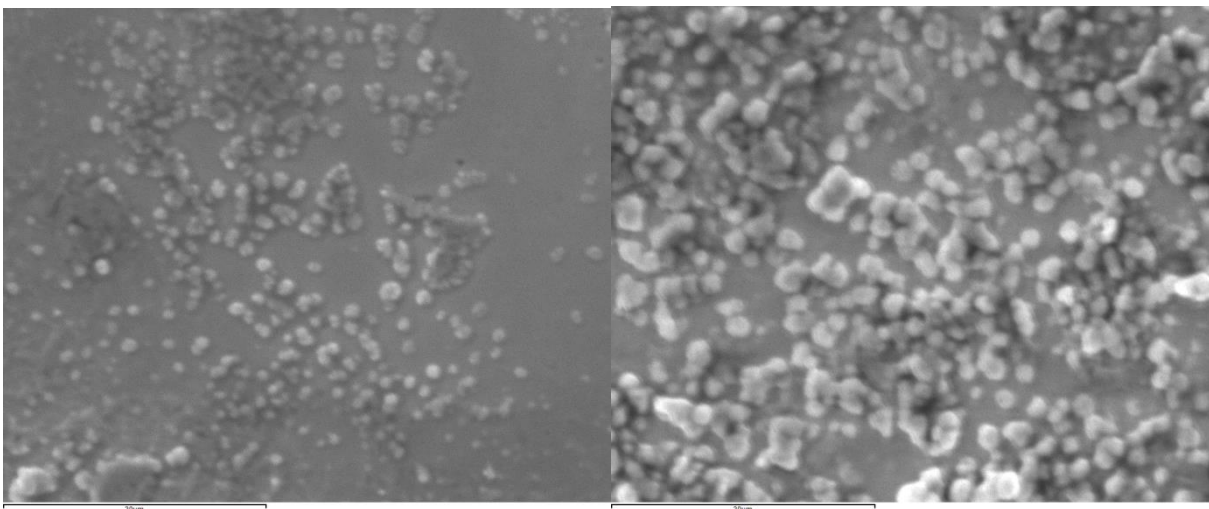


Figure 67: SEM images of gold electrode after UF_6 deposition.

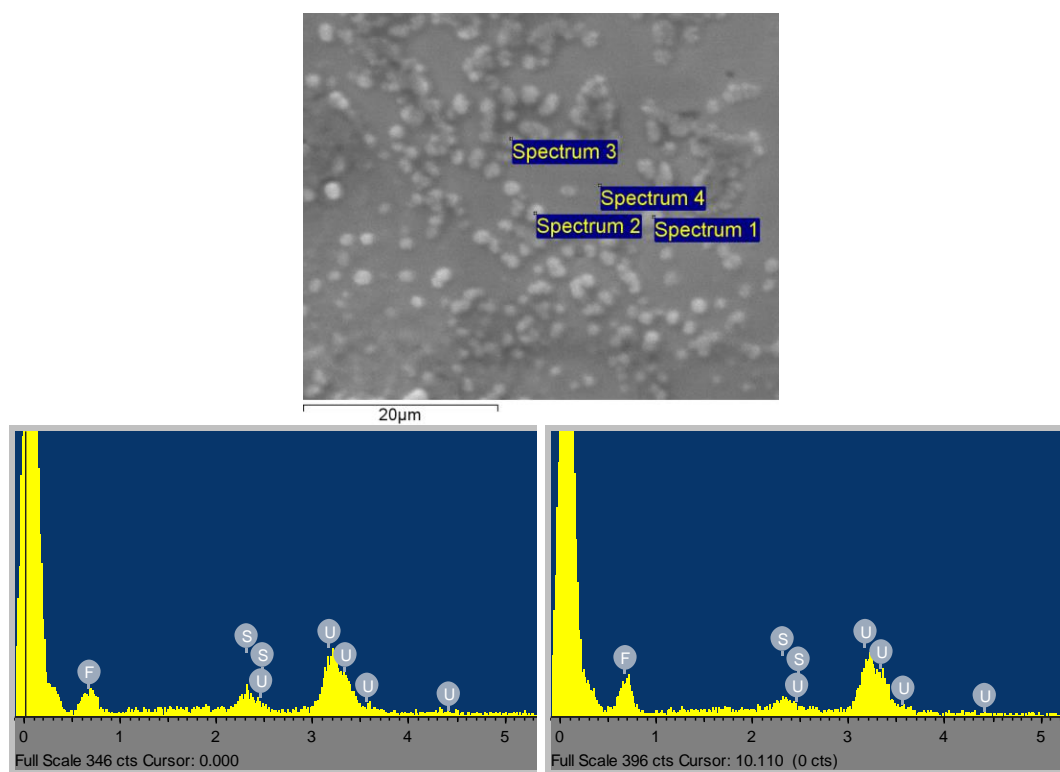


Figure 68: SEM image where point EDS was completed showing the deposits to be uranium. The EDS for spectrum 1 and 2 are shown below.

Initially it was thought that there was water in the IL that was causing the deposition of UF_4 rather than U-metal. These depositions were repeated several times after drying the $[\text{MPPi}][\text{TFSI}]$ before dissolutions, but similar results were achieved with the deposition of what appears to be UF_4 . In previous work by Katherine Lubke, uranium deposits were achieved out of UF_6 in 1-butyl-1-methylpiperidinium $[\text{TFSI}]$ ($[\text{BMPI}][\text{TFSI}]$) on gold foil in atmosphere. These deposits appeared to be uranium metal from their geometric crystalline shape on the electrode surface. The EDS mapping also indicated the deposits as uranium with no correlation to fluoride.¹⁴⁶ It is possible that the change in cation resulted in the difference in the deposits produced. It could also be the change in atmosphere. As shown with the water driven precipitates, the addition of water to the IL changes the precipitation of the uranium. It's possible the few hundred of ppms of water scavenged by the IL when exposed to atmosphere facilitates the reduction of the U from U(VI) to U(III) to U(0) through the collection of the F^- as the uranium is reduced.

5.7 Conclusions

In this chapter three routes for the recovery of uranium were explored. Over time high concentration solutions result in the precipitation of $[\text{MPPi}]_2\text{UF}_6$ as shown by TGA. UV-Vis further shows the time dependent precipitates are from a second reduction of the uranium, from U(V) in the dissolved species to U(IV) in the precipitated species. After the second reduction the uranium precipitates with two $[\text{MPPi}]$ cations.

The second and accelerated route for recovery is the water driven precipitates. These are produced by a minimum 1:10 ratio of aqueous to IL to minimize the loss of uranium to the aqueous phase. These precipitates are primarily hydrated UF_4 as shown by PXRD and TGA. However, there's likely some residual $[\text{MPPi}][\text{TFSI}]$ in the solid based on the Raman and IR

spectra. This system could be optimized further to reduce the loss of uranium to the aqueous phase. The gel-like precipitates from the 1:100 and 1:1000 aqueous to IL phase ratios still needs to be evaluated.

The final route to recovery is the electrochemical reduction. As previously shown in chapter 4, the reduction of U(V) to U(IV) is achieved relatively easily. However, in this system the reduction of U(IV) to U(III) and ultimately U(0) was not achieved. Based on SEM-EDS, it was shown that UF_4 was deposited on the gold electrodes. It was previously shown that U metal deposits were achieved in a closely related IL on the bench top. Further investigation is needed to evaluate whether the IL or the atmospheric environment is the reason for the difference in deposits.

Chapter 6. Conclusions and Future Work

6.1 Conclusions:

Recovery of critical material materials such as lithium and uranium are a matter of national importance. As our vehicles and power grids increasingly use LIBs, the demand for lithium will continue to increase. It is necessary to recover lithium from LIBs at their end of life to reduce our dependence on lithium mining in foreign states and the environmental impact of lithium mining. Depleted uranium (DU) is a valuable resource for military and commercial applications. Depleted uranium can be added to concrete mixture to produce high density concrete which can be used in spent fuel storage silos. It can be used as shielding material for tanks when mixed with molten polyethylene. In terms of spent nuclear fuel waste storage, the DU can be used as a backfill component in a repository or as package fills in waste packages of spent or high-level waste. If in the future fast reactors are utilized in the U.S., DU can be used as a fuel source as well and there will be no need to further mine uranium ore.¹⁴⁷

In chapter 3 two pathways for dissolution of lithium in ILs was demonstrated. In this study Li_2CO_3 was dissolved directly or indirectly into the $[\text{MPPi}][\text{TFSI}]$. LiH was shown to be recovered in inert atmospheres and LiOH was recovered on bench top. In theory, the dissolution on LiOH into $[\text{MPPi}][\text{TFSI}]$ could easily be facilitated with HTFSI in the same manner. Direct dissolution of LiOH into an IL would close the lifecycle loop for lithium in LIBs.

Two methods for electrochemical recovery were exhibited with steady state and differential pulse deposition. Both methods achieved macroscale deposition. However, the differential pulse deposition produced deposits that adhered to the electrode and reduced the discoloration of the $[\text{MPPi}][\text{TFSI}]$ that is indicative of damage to the IL. It was also shown that the initial CV cycle was imperative to the adherence of deposits to the electrode. Deposition was

also exhibited on both gold and carbon electrodes. Gold electrodes typically visually produced more deposits than the carbon electrodes, but graphite electrodes are significantly cheaper and will likely be the electrodes utilized in batteries.

In chapter 4 the direct dissolution of UF_6 into $[\text{MPPi}][\text{TFSI}]$ was studied. The dissolution was exothermic as indicated by the observation that high concentration solutions were warm to the touch even through the glovebox gloves. The UF_6 readily dissolved into the $[\text{MPPi}][\text{TFSI}]$. Characterization of the solution via XAFS showed that 6 fluorides remained coordinated to the uranium. UV-Vis spectroscopy and XFAS bond lengths show the uranium to be reduced from U(VI) to U(V). It was concluded that the mechanism for the dissolution and reduction was due to the donation of an electron from the $[\text{TFSI}]$ anion to produce TFSI^\bullet . The U(V)/U(IV) redox couple was isolated electrochemically. The couple was primarily irreversible to the reduction of U(IV).

After the dissolution, three routes for recovery were explored. In high concentration solutions, precipitation of uranium was observed over time. Heating these time induced precipitates to 1400 °C in the TGA resulted in UO_2 . The mass loss was indicative of the time induced precipitates being $[\text{MPPi}]_2\text{UF}_6$. This would indicate that a second electron transfer from a $[\text{TFSI}]$ anion to the dissolved UF_6^- species occurs. The UF_6^{2-} can then form a solid precipitate with two of the $[\text{MPPi}]$ cations. This second electron transfer is kinetically much slower than the first. In low concentration solutions ($< 0.1 \text{ M}$) uranium was shown to remain primarily in the U(V) state when examined after one year by XAFS.

A second precipitation route was identified by adding water to the UF_6 solution. This prompted the immediate precipitation of hydrated UF_4 as shown with PXRD and TGA. When using 1:1 ratio of UF_6 solution to aqueous phase, about one fourth of the uranium was lost to the

aqueous phase in the likely form $\text{UO}_2\text{F}_n^{(n-2)}$ complexes based on the five band signature of uranyl in UV-Vis.

The final method for recovery was electrochemically driven. It was shown deposits of likely UF_4 were achieved using the same steady state method as used in chapter 3 with the lithium. SEM-EDS was completed on the electrode showing small deposits on the electrode surface. Most of the deposits did not adhere to the electrode and remained in the IL once the electrode was removed from the solution.

While not presented in this work, a sample of both the time induced $[\text{MPPi}]_2\text{UF}_6$ and the water induced hydrated UF_4 were sent to Los Alamos National Lab (LANL). At LANL the solids were dissolved in nitric acid and analyzed using a Thermal Ionization Mass Spectrometer (TIMS) to measure the isotopic ratios of the uranium. The original UF_6 was natural uranium. The resulting $^{235}\text{U}/^{238}\text{U}$ from the TIMS measurements were very close to those of the natural uranium. This is promising initial evidence that the methods presented here could be developed into an important technique for IAEA inspectors to use in the field for validation of non-proliferation treaties.

6.2 Future Work:

The lithium work has resulted in an international patent.¹⁴⁸ The next steps for this work would be in the scale up from bench top to industrial scale. The reusability and efficiency of deposition was not evaluated or the percent recovery of lithium. These are all aspects requiring evaluations before the technology could be used in industry. This work does exhibit the proof of principle for the lithium recovery from ILs by electrochemical means.

More work needs to be done to optimize the recovery of uranium from IL. It was shown reduced volumes of water could be used to precipitate the uranium but evaluation is not complete

in determining the amount of uranium lost to the aqueous phase. The precipitated UF_4 also appears to have IL that is not completely removed based on FTIR and Raman measurements of the two solids. In previous work on uranium recovery from a similar but different IL SEM images showed geometric uranium crystals on a gold foil electrode. With EDS analysis and due to the crystalline shape, it was assumed those deposits were metallic. Metallic deposits were not achieved in this work. It could be due to the IL used or potentially some water in solution is necessary to facilitate the deposition of U metal since this previous work was completed on the bench top.

Future studies will investigate the mechanism and possible pathways for the regeneration of the oxidized the [TFSI] anion in the IL using electrochemical methods. The vast majority of studies examining the TFSI anion and radical have utilized shifts in the ^{13}F NMR spectra. We are currently unable to perform these measurements to validate the reductive dissolution of UF_6 and the reduction of the TFSI radical. Future studies are also underway to identify pathways for the recovery of uranium from the dissolution of UF_6 in IL. The goal would be to identify pathways for recovery that could result in a high throughput process for converting UF_6 to more useful uranium materials without using H_2 or producing gaseous HF.

References

- (1) Chu, S. *Critical Materials Strategy*; Diane Publishing Co, 2010.
- (2) Scrosati, B. History of Lithium Batteries. *J. Solid State Electrochem.* **2011**, *15* (7–8), 1623–1630. <https://doi.org/10.1007/s10008-011-1386-8>.
- (3) Mohr, S. H.; Mudd, G. M.; Giurco, D. Lithium Resources and Production: Critical Assessment and Global Projections. *Minerals* **2012**, *2* (1), 65–84. <https://doi.org/10.3390/min2010065>.
- (4) Ziemann, S.; Müller, D. B.; Schebek, L.; Weil, M. Modeling the Potential Impact of Lithium Recycling from EV Batteries on Lithium Demand: A Dynamic MFA Approach. *Resour. Conserv. Recycl.* **2018**, *133*, 76–85. <https://doi.org/10.1016/j.resconrec.2018.01.031>.
- (5) Leader, A.; Gaustad, G.; Babbitt, C. The Effect of Critical Material Prices on the Competitiveness of Clean Energy Technologies. *Mater. Renew. Sustain. Energy* **2019**, *8* (2), 1–17. <https://doi.org/10.1007/s40243-019-0146-z>.
- (6) Prior, T.; Wäger, P. A.; Stamp, A.; Widmer, R.; Giurco, D. Sustainable Governance of Scarce Metals: The Case of Lithium. *Sci. Total Environ.* **2013**. <https://doi.org/10.1016/j.scitotenv.2013.05.042>.
- (7) Dolotko, O.; Senyshyn, A.; Mühlbauer, M. J.; Nikolowski, K.; Ehrenberg, H. Understanding Structural Changes in NMC Li-Ion Cells by in Situ Neutron Diffraction. *J. Power Sources* **2014**, *255*, 197–203. <https://doi.org/10.1016/j.jpowsour.2014.01.010>.
- (8) Yoshimatsu, I. Lithium Electrode Morphology during Cycling in Lithium Cells. *J. Electrochem. Soc.* **1988**, *135* (10), 2422. <https://doi.org/10.1149/1.2095351>.
- (9) Liang, Z.; Zheng, G.; Liu, C.; Liu, N.; Li, W.; Yan, K.; Yao, H.; Hsu, P.-C.; Chu, S.; Cui,

- Y. Polymer Nanofiber-Guided Uniform Lithium Deposition for Battery Electrodes. *Nano Lett.* **2015**, *15* (5), 2910–2916. <https://doi.org/10.1021/nl5046318>.
- (10) Kim, H.; Jeong, G.; Kim, Y.; Kim, J.; Park, C.; Sohn, H. Metallic Anodes for next Generation Secondary Batteries. *Chem. Soc. Rev.* **2013**, *42* (23), 9011–9034. <https://doi.org/10.1039/C3CS60177C>.
- (11) Li, Z.; Huang, J.; Yann Liaw, B.; Metzler, V.; Zhang, J. A Review of Lithium Deposition in Lithium-Ion and Lithium Metal Secondary Batteries. *J. Power Sources* **2014**, *254*, 168–182. <https://doi.org/10.1016/j.jpowsour.2013.12.099>.
- (12) Saloojee, F.; Lloyd, J. Lithium Battery Recycling Process. Department of Environmental Affairs Development Bank of South Africa (Project No. DB-074 (RW1/1016)). **2015**, 27 (0).
- (13) Gaines, L.; Sullivan, J.; Burnham, A.; Belharouak, I. Life-Cycle Analysis of Production and Recycling of Lithium Ion Batteries. *Transp. Res. Rec.* **2011**, No. 2252, 57–65. <https://doi.org/10.3141/2252-08>.
- (14) McLaughlin, W.; Adams, T. S. Li Reclamation Process. 5,888,463, March 30, 1999.
- (15) Dolotko, O.; Hlova, I. Z.; Mudryk, Y.; Gupta, S.; Balema, V. P. Mechanochemical Recovery of Co and Li from LCO Cathode of Lithium-Ion Battery. *J. Alloys Compd.* **2020**, *824*, 153876. <https://doi.org/10.1016/j.jallcom.2020.153876>.
- (16) Ren, G.; Xiao, S.; Xie, M.; Pan, B.; Chen, J.; Wang, F.; Xia, X. Recovery of Valuable Metals from Spent Lithium Ion Batteries by Smelting Reduction Process Based on FeO–SiO₂–Al₂O₃ Slag System. *Trans. Nonferrous Met. Soc. China* **2017**, *27* (2), 450–456. [https://doi.org/10.1016/s1003-6326\(17\)60051-7](https://doi.org/10.1016/s1003-6326(17)60051-7).
- (17) U.S. Nuclear Regulatory Commission Information Digest. Washington, DC 2020, p 58.

- (18) Energy, U. D. of. *Disposition of DOE Excess Depleted Uranium, Natural Uranium, and Low-Enriched Uranium*; 2006.
- (19) Gosling, F. G. The Manhattan Project: Making the Atomic Bomb. 1999 Edition. USDOE Office of Human Resources and Administration, Washington, DC (United States) 1999. <https://doi.org/10.2172/303853>.
- (20) Blanpain, P.; Capus, G.; Palussiere, J.-C. Nuclear Fuel Cycle Front End Chemistry. *Chim.* **2005**, 59 (12), 894–897.
- (21) Krass, A. S.; Boskma, P.; Elzen, B.; Smit, W. A. *Uranium Enrichment and Nuclear Weapon Proliferation*; Taylor & Francis Ltd: London, 1983.
- (22) Katz, J. J.; Rabinowitch, E. *Chemistry of Uranium*, 2nd ed.; Smith, P., Ed.; Dover Publications, Inc.: New York, 1961.
- (23) Barber, E. J. The Physical and Chemical Properties of Uranium Hexafluoride. In *Uranium Hexafluoride-Safe Handling, Processing, and Transporting*; 1988; pp 1–6.
- (24) Massignon, D. Uranium Enrichment. In *Topics in Applied Physics*; Villani, S., Ed.; Springer-Verlag: New York, 1979; pp 55–182.
- (25) Lawrence Livermore National Lab. *Final Plan for the Conversion of Depleted Uranium Hexafluoride As Required by Public Law 105-204*; 1999.
- (26) US Office of Environmental Management. *Officials Highlight Cleanup Progress at Portsmouth, Paducah*; 2018.
- (27) World Nuclear Association. *The Nuclear Fuel Report 2019*; 2019.
- (28) Edwards, C. R.; Oliver, A. J. Uranium Processing: A Review of Current Methods and Technology. *JOM* **2000**, 52 (9), 12–20. <https://doi.org/10.1007/s11837-000-0181-2>.
- (29) Elert, M.; Skagius, K. Estimates of Health Risks Associated with Uranium Hexafluoride

- Transport by Air. *Int. J. Radioact. Mater. Transp.* **1990**, *1* (3), 151–161.
- (30) Mohsendokht, M. Risk Assessment of Uranium Hexafluoride Release from a Uranium Conversion Facility by Using a Fuzzy Approach. *J. Loss Prev. Process Ind.* **2017**, *45*, 217–228. <https://doi.org/10.1016/j.jlp.2017.01.004>.
- (31) World Nuclear Association. Conversion and Deconversion <https://world-nuclear.org/information-library/nuclear-fuel-cycle/conversion-enrichment-and-fabrication/conversion-and-deconversion.aspx> (accessed Jul 29, 2019).
- (32) Morel, B.; Duperret, B. Uranium and Fluorine Cycles in the Nuclear Industry. *J. Fluor. Chem.* **2009**, *130* (1), 7–10. <https://doi.org/10.1016/j.jfluchem.2008.05.022>.
- (33) Borgard, J. M.; Herbelet, F.; Gwinner, B.; Fleche, J. L. Thermodynamics Analysis of the Current Defluorination Process of UF₆ and Its Application for Efficient Recycling of Fluorine in the French Nuclear Fuel Cycle. In *GLOBAL 2015-International Conference on Advanced Nuclear Fuel Cycle and Related Nuclear Systems*; 2015.
- (34) Council, N. R. Nuclear Wastes: Technologies for Separations and Transmutation. **1996**.
- (35) Aspinall, H. C. *Chemistry of the F-Block Elements*; Gordon and Breach Science Publishers: Amsterdam, 2018.
- (36) Kumari, I.; Kumar, B. V. R.; Khanna, A. A Review on UREX Processes for Nuclear Spent Fuel Reprocessing. *Nucl. Eng. Des.* **2020**, *358*, 110410. <https://doi.org/10.1016/J.NUCENGDES.2019.110410>.
- (37) Manson Benedict, P. D.; Thomas H. Pigford, P. D.; Levi, P. D. H. W. FUEL REPROCESSING; McGraw-Hill Education: New York, 1981.
- (38) Koppmann, R. *Volatile Organic Compounds in the Atmosphere*; John Wiley & Sons, 2008.

- (39) Reichardt, C. Solvents and Solvent Effects: An Introduction. *Org. Process Res. Dev.* **2007**, *11* (1), 105–113.
- (40) Sundermeyer, W. Fused Salts and Their Use as Reaction Media. *Angew. Chemie Int. Ed. English* **1965**, *4* (3), 222–238.
- (41) Chum, H. L.; Koch, V. R.; Miller, L. L.; Osteryoung, R. A. Electrochemical Scrutiny of Organometallic Iron Complexes and Hexamethylbenzene in a Room Temperature Molten Salt. *J. Am. Chem. Soc.* **1975**, *97* (11), 3264–3265.
- (42) Wilkes, J. S.; Zaworotko, M. J. Air and Water Stable 1-Ethyl-3-Methylimidazolium Based Ionic Liquids. *J. Chem. Soc. Chem. Commun.* **1992**, No. 13, 965–967.
- (43) Hapiot, P.; Lagrost, C. Electrochemical Reactivity in Room-Temperature Ionic Liquids. *Chem. Rev.* **2008**, *108* (7), 2238–2264. <https://doi.org/10.1021/cr0680686>.
- (44) MacFarlane, D. R.; Seddon, K. R. Ionic Liquids—Progress on the Fundamental Issues. *Aust. J. Chem.* **2007**, *60* (1), 3–5.
- (45) Chatel, G.; Pflieger, R.; Naffrechoux, E.; I. Nikitenko, S.; Suptil, J.; Goux-Henry, C.; Kardos, N.; Andrioletti, B.; Draye, M. Hydrophobic Bis(Trifluoromethylsulfonyl)Imide-Based Ionic Liquids Pyrolysis: Through the Window of the Ultrasonic Reactor. *ACS Sustain. Chem. & Eng.* **2012**, *1* (1), 137–143. <https://doi.org/10.1021/sc300068d>.
- (46) Binnemans, K. Lanthanides and Actinides in Ionic Liquids. *Chem. Rev.* **2007**, *107* (6), 2592–2614. <https://doi.org/10.1021/cr050979c>.
- (47) Dzyuba, S. V; Bartsch, R. A. Influence of Structural Variations in 1-alkyl (Aalkyl)-3-methylimidazolium Hexafluorophosphates and Bis (Trifluoromethylsulfonyl) Imides on Physical Properties of the Ionic Liquids. *ChemPhysChem* **2002**, *3* (2), 161–166.
- (48) Tokuda, H.; Hayamizu, K.; Ishii, K.; Susan, M. A. B. H.; Watanabe, M. Physicochemical

- Properties and Structures of Room Temperature Ionic Liquids. 2. Variation of Alkyl Chain Length in Imidazolium Cation. *J. Phys. Chem. B* **2005**, *109* (13), 6103–6110.
- (49) Bonhote, P.; Dias, A.-P.; Papageorgiou, N.; Kalyanasundaram, K.; Grätzel, M. Hydrophobic, Highly Conductive Ambient-Temperature Molten Salts. *Inorg. Chem.* **1996**, *35* (5), 1168–1178.
- (50) Papaiconomou, N.; Salminen, J.; Lee, J.-M.; Prausnitz, J. M. Physicochemical Properties of Hydrophobic Ionic Liquids Containing 1-Octylpyridinium, 1-Octyl-2-Methylpyridinium, or 1-Octyl-4-Methylpyridinium Cations. *J. Chem. Eng. Data* **2007**, *52* (3), 833–840.
- (51) Hunt, P. A. Why Does a Reduction in Hydrogen Bonding Lead to an Increase in Viscosity for the 1-Butyl-2, 3-Dimethyl-Imidazolium-Based Ionic Liquids? *J. Phys. Chem. B* **2007**, *111* (18), 4844–4853.
- (52) Okoturo, O. O.; VanderNoot, T. J. Temperature Dependence of Viscosity for Room Temperature Ionic Liquids. *J. Electroanal. Chem.* **2004**. <https://doi.org/10.1016/j.jelechem.2003.12.050>.
- (53) Zistler, M.; Wachter, P.; Wasserscheid, P.; Gerhard, D.; Hinsch, A.; Sastrawan, R.; Gores, H. J. Comparison of Electrochemical Methods for Triiodide Diffusion Coefficient Measurements and Observation of Non-Stokesian Diffusion Behaviour in Binary Mixtures of Two Ionic Liquids. *Electrochim. Acta* **2006**, *52* (1), 161–169. <https://doi.org/10.1016/J.ELECTACTA.2006.04.050>.
- (54) Every, H.; Bishop, A. .; Forsyth, M.; MacFarlane, D. . Ion Diffusion in Molten Salt Mixtures. *Electrochim. Acta* **2000**, *45* (8–9), 1279–1284. [https://doi.org/10.1016/S0013-4686\(99\)00332-1](https://doi.org/10.1016/S0013-4686(99)00332-1).

- (55) Suarez, P. A. Z.; Selbach, V. M.; Dullius, J. E. L.; Einloft, S.; Piatnicki, C. M. S.; Azambuja, D. S.; de Souza, R. F.; Dupont, J. Enlarged Electrochemical Window in Dialkyl-Imidazolium Cation Based Room-Temperature Air and Water-Stable Molten Salts. *Electrochim. Acta* **1997**, *42* (16), 2533–2535. [https://doi.org/10.1016/S0013-4686\(96\)00444-6](https://doi.org/10.1016/S0013-4686(96)00444-6).
- (56) Suarez, P. A. Z.; Consorti, C. S.; Souza, R. F. de; Dupont, J.; Gonçalves, R. S. Electrochemical Behavior of Vitreous Glass Carbon and Platinum Electrodes in the Ionic Liquid 1-n-Butyl-3-Methylimidazolium Trifluoroacetate. *J. Braz. Chem. Soc.* **2002**, *13*, 106–109.
- (57) Droessler, J. Direct Dissolution and Electrochemical Investigation of Cerium and Uranium in Ionic Liquid, University of Nevada, Las Vegas, 2016.
- (58) Cammarata, L.; Kazarian, S. G.; Salter, P. A.; Welton, T. Molecular States of Water in Room Temperature Ionic Liquids. *Phys. Chem. Chem. Phys.* **2001**, *3* (23), 5192–5200.
- (59) Widegren, J. A.; Laesecke, A.; Magee, J. W. The Effect of Dissolved Water on the Viscosities of Hydrophobic Room-Temperature Ionic Liquids. *Chem. Commun.* **2005**, No. 12, 1610–1612.
- (60) Fitchett, B. D.; Knepp, T. N.; Conboy, J. C. 1-Alkyl-3-Methylimidazolium Bis(Perfluoroalkylsulfonyl)Imide Water-Immiscible Ionic Liquids - The Effect of Water on Electrochemical and Physical Properties. *J. Electrochem. Soc.* **2004**, *151* (7), E219–E225. <https://doi.org/10.1149/1.1751197>.
- (61) Ohno, H. *Electrochemical Aspects of Ionic Liquids*; Wiley-Interscience/J. Wiley: Hoboken, N.J., 2005.
- (62) Visser, A. E.; Rogers, R. D. Room-Temperature Ionic Liquids: New Solvents for f-

- Element Separations and Associated Solution Chemistry. *J. Solid State Chem.* **2003**, *171* (1), 109–113. [https://doi.org/https://doi.org/10.1016/S0022-4596\(02\)00193-7](https://doi.org/10.1016/S0022-4596(02)00193-7).
- (63) Rao, C. J.; Venkatesan, K. A.; Nagarajan, K.; Srinivasan, T. G. Dissolution of Uranium Oxides and Electrochemical Behavior of U (VI) in Task Specific Ionic Liquid. *Radiochim. acta* **2008**, *96* (7), 403–409.
- (64) Katz, J.; Rabinowitch, E. Extraction of Uranium from Ores and Preparation of Uranium Metal. In *The Chemistry of Uranium*; Dover Publications, Inc., 1951; pp 111–132.
- (65) De Waele, R.; Heerman, L.; D’Olieslager, W. Electrochemistry of Uranium(IV) in Acidic $\text{AlCl}_3\text{+N-(n-Butyl)Pyridinium Chloride}$ Room-Temperature Molten Salts. *J. Electroanal. Chem. Interfacial Electrochem.* **1982**, *142* (1), 137–146. [https://doi.org/https://doi.org/10.1016/S0022-0728\(82\)80011-9](https://doi.org/10.1016/S0022-0728(82)80011-9).
- (66) De Waele, R.; Heerman, L.; D’olieslager, W. Potentiometric and Spectroscopic Study of Uranium (IV)-Uranium (III) in Acidic $\text{AlCl}_3\text{-N-(n-BUTYL) Pyridinium Chloride}$ Melts. *J. Less Common Met.* **1986**, *122*, 319–327.
- (67) Nikitenko, S. I.; Moisy, P.; Berthon, C.; Bisel, I. *Spectroscopic and Voltammetric Study of NpCl_6^{2-} and PuCl_6^{2-} Complexes in Hydrophobic Room Temperature Ionic Liquid $[\text{BuMeIm}][(\text{CF}_3\text{SO}_2)_2\text{N}]$* ; Institute of Physical Chemistry, 2004.
- (68) I. Nikitenko, S.; Cannes, C.; Le Naour, C.; Moisy, P.; Trubert, D. Spectroscopic and Electrochemical Studies of U(IV)–Hexachloro Complexes in Hydrophobic Room-Temperature Ionic Liquids $[\text{BuMeIm}][\text{Tf}_2\text{N}]$ and $[\text{MeBu}_3\text{N}][\text{Tf}_2\text{N}]$. *Inorg. Chem.* **2005**, *44* (25), 9497–9505. <https://doi.org/10.1021/ic051065b>.
- (69) Bhatt, A. I.; May, I.; Volkovich, V. A.; Hetherington, M. E.; Lewin, B.; Thied, R. C.; Ertok, N. Group 15 Quaternary Alkyl Bistriflimides: Ionic Liquids with Potential

- Application in Electropositive Metal Deposition and as Supporting Electrolytes. *J. Chem. Soc. Dalt. Trans.* **2002**, No. 24, 4532–4534.
- (70) Bhatt, A. I.; May, I.; Volkovich, V. A.; Collison, D.; Helliwell, M.; Polovov, I. B.; Lewin, R. G. Structural Characterization of a Lanthanum Bistriflimide Complex, $\text{La}(\text{N}(\text{SO}_2\text{CF}_3)_2)_3(\text{H}_2\text{O})_3$, and an Investigation of La, Sm, and Eu Electrochemistry in a Room-Temperature Ionic Liquid, $[\text{Me}_3\text{N}^n\text{Bu}][\text{N}(\text{SO}_2\text{CF}_3)_2]$. *Inorg. Chem.* **2005**, *44* (14), 4934–4940.
- (71) Allen, D.; Baston, G.; Bradley, A. E.; Gorman, T.; Haile, A.; Hamblett, I.; Hatter, J. E.; Healey, M. J. F.; Hodgson, B.; Lewin, R.; et al. An Investigation of the Radiochemical Stability of Ionic Liquids. **2002**. <https://doi.org/10.1039/b111042j>.
- (72) Berthon, L.; Nikitenko, S. I.; Bisel, I.; Berthon, C.; Faucon, M.; Saucerotte, B.; Zorz, N.; Moisy, P. Influence of Gamma Irradiation on Hydrophobic Room-Temperature Ionic Liquids $[\text{BuMeIm}]\text{PF}_6$ and $[\text{BuMeIm}](\text{CF}_3\text{SO}_2)_2\text{N}$. *Dalt. Trans.* **2006**, No. 21, 2526–2534.
- (73) Zanello, P. *Inorganic Electrochemistry*; The Royal Society of Chemistry, 2003. <https://doi.org/10.1039/9781847551146>.
- (74) Sun, J.; Forsyth, M.; R. MacFarlane, D. Room-Temperature Molten Salts Based on the Quaternary Ammonium Ion. *J. Phys. Chem. B* **1998**, *102* (44), 8858–8864. <https://doi.org/10.1021/jp981159p>.
- (75) Mabbott, G. A. An Introduction to Cyclic Voltammetry. *J. Chem. Educ.* **1983**, *60* (9), 697.
- (76) Elgrishi, N.; Rountree, K. J.; McCarthy, B. D.; Rountree, E. S.; Eisenhart, T. T.; Dempsey, J. L. A Practical Beginner's Guide to Cyclic Voltammetry. *J. Chem. Educ.* **2018**, *95* (2), 197–206.

- (77) Saheb, A.; Janata, J.; Josowicz, M. Reference Electrode for Ionic Liquids. *Electroanalysis* **2006**, *18* (4), 405–409. <https://doi.org/10.1002/elan.200503435>.
- (78) Rocha, F. S.; Gomes, A. J.; Lunardi, C. N.; Kaliaguine, S.; Patience, G. S. Experimental Methods in Chemical Engineering: Ultraviolet Visible Spectroscopy—UV-Vis. *Can. J. Chem. Eng.* **2018**, *96* (12), 2512–2517.
- (79) Ismail, A. A.; van de Voort, F. R.; Sedman, J. Fourier Transform Infrared Spectroscopy: Principles and Applications. In *Techniques and instrumentation in analytical chemistry*; Elsevier, 1997; Vol. 18, pp 93–139.
- (80) Edinburch Instruments. What is the Stokes Shift? <https://www.edinst.com/blog/what-is-the-stokes-shift/> (accessed Feb 22, 2022).
- (81) Skoog, D. A.; Holler, F. J.; Crouch, S. R. *Principles of Instrumental Analysis*; Cengage learning, 2017.
- (82) Jarvis, I.; Jarvis, K. E. Inductively Coupled Plasma-Atomic Emission Spectrometry in Exploration Geochemistry. *J. Geochemical Explor.* **1992**, *44* (1–3), 139–200. [https://doi.org/10.1016/0375-6742\(92\)90050-I](https://doi.org/10.1016/0375-6742(92)90050-I).
- (83) Denecke, M. Actinide Speciation Using X-Ray Absorption Fine Structure Spectroscopy. *Coord. Chem. Rev.* **2006**, *250* (7–8), 730–754. <https://doi.org/10.1016/j.ccr.2005.09.004>.
- (84) Zhou, W.; Apkarian, R.; Wang, Z. L.; Joy, D. Fundamentals of Scanning Electron Microscopy (SEM). In *Scanning microscopy for nanotechnology*; Springer, 2006; pp 1–40.
- (85) Goldstein, J. I.; Newbury, D. E.; Michael, J. R.; Ritchie, N. W. M.; Scott, J. H. J.; Joy, D. C. *Scanning Electron Microscopy and X-Ray Microanalysis*; Springer, 2017.
- (86) Gordon, C.; Rohner, R. *Fundamentals of the Coulometric Karl Fischer Titration with*

- Selected Applications. Mettler Toledo Titrators DL32/DL39*; Mettler-Toledo GmbH: Switzerland, 2005.
- (87) Armand, M.; Endres, F.; Macfarlane, D. R.; Ohno, H.; Scrosati, B. Ionic-Liquid Materials for the Electrochemical Challenges of the Future. *Nat. Mater.* **2009**, 8 (8), 621–629. <https://doi.org/10.1038/nmat2448>.
- (88) Papageorgiou, N.; Athanassov, Y.; Armand, M.; Bonho, P.; Pettersson, H.; Azam, A.; Grätzel, M. The Performance and Stability of Ambient Temperature Molten Salts for Solar Cell Applications. *J. Electrochem. Soc.* **1996**, 143 (10), 3099.
- (89) *CRC Handbook of Chemistry and Physics*, 85th ed.; Weast, R. C., Ed.; CRC Press, 1990.
- (90) Matsumoto, H.; Yanagida, M.; Tanimoto, K.; Kojima, T.; Tamiya, Y.; Miyazaki, Y. Improvement of Ionic Conductivity of Room Temperature Molten Salt Based on Quaternary Ammonium Cation and Imide Anion. In *Molten Salts XII: Proceedings of the International Symposium*; Trulove, P. C., Ed.; Electrochemical Society, 2000; pp 186–192.
- (91) Sakaebe, H.; Matsumoto, H. N-Methyl-N-Propylpiperidinium Bis(Trifluoromethanesulfonyl)Imide (PP13-TFSI) - Novel Electrolyte Base for Li Battery. *Electrochem. commun.* **2003**, 5 (7), 594–598. [https://doi.org/10.1016/S1388-2481\(03\)00137-1](https://doi.org/10.1016/S1388-2481(03)00137-1).
- (92) Matsumoto, H.; Matsuda, T.; Miyazaki, Y. Room Temperature Molten Salts Based on Trialkylsulfonium Cations and Bis (Trifluoromethylsulfonyl) Imide. *Chem. Lett.* **2000**, 29 (12), 1430–1431.
- (93) Zheng, H.; Dong, T.; Sha, Y.; Jiang, D.; Zhang, H.; Zhang, S. Selective Extraction of Lithium from Spent Lithium Batteries by Functional Ionic Liquid. *ACS Sustain. Chem.*

- & Eng.* **2021**, 9 (20), 7022–7029. <https://doi.org/10.1021/acssuschemeng.1c00718>.
- (94) Howlett, P. C.; MacFarlane, D. R.; Hollenkamp, A. F. High Lithium Metal Cycling Efficiency in a Room-Temperature Ionic Liquid. *Electrochem. Solid-State Lett.* **2004**, 7 (5), A97. <https://doi.org/10.1149/1.1664051>.
- (95) Steiger, J.; Kramer, D.; Mönig, R. Microscopic Observations of the Formation, Growth and Shrinkage of Lithium Moss during Electrodeposition and Dissolution. *Electrochim. Acta* **2014**, 136, 529–536. <https://doi.org/10.1016/J.ELECTACTA.2014.05.120>.
- (96) Lewandowski, A.; Świdarska-Mocek, A. Ionic Liquids as Electrolytes for Li-Ion Batteries—An Overview of Electrochemical Studies. *J. Power Sources* **2009**, 194 (2), 601–609. <https://doi.org/10.1016/J.JPOWSOUR.2009.06.089>.
- (97) Zhang, B.; Yao, Y.; Shi, Z.; Xu, J.; Wang, Z. Direct Electrochemical Deposition of Lithium from Lithium Oxide in a Highly Stable Aluminium-Containing Solvate Ionic Liquid. *ChemElectroChem* **2018**, 5 (22), 3368–3372.
- (98) Bhatt, A. I.; Best, A. S.; Huang, J.; Hollenkamp, A. F. Application of the N-Propyl-N-Methyl-Pyrrolidinium Bis(Fluorosulfonyl)Imide RTIL Containing Lithium Bis(Fluorosulfonyl)Imide in Ionic Liquid Based Lithium Batteries. *J. Electrochem. Soc.* **2010**, 157 (1), A66. <https://doi.org/10.1149/1.3257978>.
- (99) Stark, J. K.; Ding, Y.; Kohl, P. A. Dendrite-Free Electrodeposition and Reoxidation of Lithium-Sodium Alloy for Metal-Anode Battery. *J. Electrochem. Soc.* **2011**, 158 (10), A1100. <https://doi.org/10.1149/1.3622348>.
- (100) Dilasari, B.; Jung, Y.; Kim, G.; Kwon, K. Effect of Cation Structure on Electrochemical Behavior of Lithium in [NTf₂]-Based Ionic Liquids. *ACS Sustain. Chem. & Eng.* **2015**, 4 (2), 491–496. <https://doi.org/10.1021/acssuschemeng.5b00987>.

- (101) Vega, J. A.; Zhou, J.; Kohl, P. A. Electrochemical Comparison and Deposition of Lithium and Potassium from Phosphonium- and Ammonium-TFSI Ionic Liquids. *J. Electrochem. Soc.* **2009**, *156* (4), A253. <https://doi.org/10.1149/1.3070657>.
- (102) Cama, C.; DiLeo, R. A.; Takeuchi, K. J.; Marschilok, A. C.; Takeuchi, E. S. Systematic Characterization of Ionic Liquid Electrolyte Systems for Lithium Ion Batteries. *ECS Trans.* **2014**, *61* (27), 79–85. <https://doi.org/10.1149/06127.0079ecst>.
- (103) Branco, L. C.; Rosa, J. N.; Moura Ramos, J. J.; Afonso, C. A. M. Preparation and Characterization of New Room Temperature Ionic Liquids. *Chem. Eur. J.* **2002**, *8* (16), 3671–3677.
- (104) Burke, L. D.; Nugent, P. F. The Electrochemistry of Gold: I the Redox Behaviour of the Metal in Aqueous Media. *Gold Bull.* **1997**, *30* (2), 43–53.
- (105) Lu, W.; López, C. M.; Liu, N.; Vaughey, J. T.; Jansen, A. Overcharge Effect on Morphology and Structure of Carbon Electrodes for Lithium-Ion Batteries. *J. Electrochem. Soc.* **2012**, *159* (5), A566.
- (106) Bossé, É.; Berthon, L.; Zorz, N.; Monget, J.; Berthon, C.; Bisel, I.; Legand, S.; Moisy, P. Stability of [MeBu 3 N][Tf 2 N] under Gamma Irradiation. *Dalt. Trans.* **2008**, No. 7, 924–931.
- (107) Wai, C. M.; Liao, Y.-J.; Liao, W.; Tian, G.; Addleman, R. S.; Quach, D.; Pasilis, S. P. Uranium Dioxide in Ionic Liquid with a Tri-n-Butylphosphate–HNO₃ Complex—Dissolution and Coordination Environment. *Dalt. Trans.* **2011**, *40* (18), 5039–5045.
- (108) Freiderich, J. W.; Wanigasekara, E.; Sun, X.-G.; Meisner, R. A.; Meyer III, H. M.; Luo, H.; Delmau, L. H.; Dai, S.; Moyer, B. A. Direct Electrodeposition of UO₂ from Uranyl Bis (Trifluoromethanesulfonyl) Imide Dissolved in 1-Ethyl-3-Methylimidazolium Bis

- (Trifluoromethanesulfonyl) Imide Room Temperature Ionic Liquid System. *Electrochim. Acta* **2014**, *115*, 630–638.
- (109) Wanigasekara, E.; Freiderich, J. W.; Sun, X.-G.; Meisner, R. A.; Luo, H.; Delmau, L. H.; Dai, S.; Moyer, B. A. Tandem Dissolution of UO₃ in Amide-Based Acidic Ionic Liquid and in Situ Electrodeposition of UO₂ with Regeneration of the Ionic Liquid: A Closed Cycle. *Dalt. Trans.* **2016**, *45* (25), 10151–10154.
- (110) Wei, Z.; Lu, C.; Zhou, Y.; Jiao, C.; Zhang, M.; Hou, H.; Gao, Y.; Tian, G. Asymmetric Diglycolamide in BmimNTf₂ as an Effective Solvent System for the Uranyl Extraction. *J. Radioanal. Nucl. Chem.* **2020**, *326* (1), 583–589.
- (111) Hatchett, D. W.; Droessler, J.; Kinyanjui, J. M.; Martinez, B.; Czerwinski, K. R. The Direct Dissolution of Ce₂(CO₃)₃ and Electrochemical Deposition of Ce Species Using Ionic Liquid Trimethyl-n-Butylammonium Bis(Trifluoromethanesulfonyl)Imide Containing Bis(Trifluoromethanesulfonyl)Imide. *Electrochim. Acta* **2013**, *89*, 144–151. <https://doi.org/10.1016/J.ELECTACTA.2012.10.083>.
- (112) Pemberton, W. J.; Droessler, J. E.; Kinyanjui, J. M.; Czerwinski, K. R.; Hatchett, D. W. Electrochemistry of Soluble UO₂²⁺ from the Direct Dissolution of UO₂CO₃ in Acidic Ionic Liquid Containing Water. *Electrochim. Acta* **2013**, *93*, 264–271. <https://doi.org/10.1016/j.electacta.2013.01.044>.
- (113) Yao, A.; Xiong, X.; Kang, M.; Guo, Y.; Chen, C.; Chu, T. Direct Dissolution of UO₂ in Carboxyl-Functionalized Ionic Liquids in the Presence or Absence of Fe-Containing Ionic Liquids. *Dalt. Trans.* **2020**, *49* (42), 14881–14890.
- (114) Hatchett, D. W.; Czerwinski, K. R.; Droessler, J.; Kinyanjui, J. Room Temperature Electrodeposition of Actinides from Ionic Solutions, April 25, 2017.

- (115) Yao, A.; Qu, F.; Liu, Y.; Qu, G.; Lin, H.; Hu, S.; Wang, X.; Chu, T. Ionic Liquids with Polychloride Anions as Effective Oxidants for the Dissolution of UO₂. *Dalt. Trans.* **2019**, 48, 16249. <https://doi.org/10.1039/c9dt03574e>.
- (116) Deetlefs, M.; Hussey, C. L.; Mohammed, T. J.; Seddon, K. R.; Van Den Berg, J.-A.; Zora, J. A. Uranium Halide Complexes in Ionic Liquids: An Electrochemical and Structural Study. **2006**. <https://doi.org/10.1039/b512212k>.
- (117) Kanatani, T.; Matsumoto, K.; Hagiwara, R. Syntheses and Physicochemical Properties of New Ionic Liquids Based on the Hexafluorouranate Anion. *Chem. Lett.* **2009**, 38 (7), 714–715.
- (118) Kanatani, T.; Matsumoto, K.; Nohira, T.; Hagiwara, R. Electrochemical Behavior of the Hexafluorouranate Anion in 1-Butyl-3-Methylimidazolium Bis (Trifluoromethylsulfonyl) Amide Room Temperature Ionic Liquid. *Electrochem. Solid State Lett.* **2010**, 14 (3), F1.
- (119) Selbin, J.; Ortego, J. D. Chemistry of Uranium (V). *Chem. Rev.* **1969**, 69 (5), 657–671.
- (120) Asprey, L. B.; Penneman, R. A. Properties of Uranium (V) in Hydrofluoric Acid Solution; the New Compounds HUF₆. 2.5 H₂O and HUF₆. 1.25 H₂O. *Inorg. Chem.* **1964**, 3 (5), 727–729.
- (121) Ryan, J. L. Halide Complexes of Pentavalent Uranium. *J. Inorg. Nucl. Chem.* **1971**, 33 (1), 153–177.
- (122) Rey, I.; Johansson, P.; Lindgren, J.; C. Lassègues, J.; Grondin, J.; Servant, L. Spectroscopic and Theoretical Study of (CF₃SO₂)₂N⁻ (TFSI⁻) and (CF₃SO₂)₂NH (HTFSI). *J. Phys. Chem. A* **1998**, 102 (19), 3249–3258. <https://doi.org/10.1021/jp980375v>.
- (123) Katsuhara, Y.; Hammaker, R. M.; DesMarteau, D. D. Synthesis and Properties of Chlorine

- (I) and Bromine (I) Trifluoromethanesulfonates and Raman Spectra of CF₃SO₂X (X= Fluorine, Hydroxyl, Hypochlorite). *Inorg. Chem.* **1980**, *19* (3), 607–615.
- (124) Foropoulos Jr, J.; DesMarteau, D. D. Synthesis, Properties, and Reactions of Bis ((Trifluoromethyl) Sulfonyl) Imide,(CF₃SO₂)₂NH. *Inorg. Chem.* **1984**, *23* (23), 3720–3723.
- (125) Mincher, B. J.; Wishart, J. F. The Radiation Chemistry of Ionic Liquids: A Review. *Solvent Extr. Ion Exch.* **2014**, *32* (6), 563–583.
- (126) Shkrob, I. A.; Marin, T. W.; Chemerisov, S. D.; Wishart, J. F. Radiation Induced Redox Reactions and Fragmentation of Constituent Ions in Ionic Liquids. 1. Anions. *J. Phys. Chem. B* **2011**, *115* (14), 3872–3888.
- (127) Chou, L.-H.; L. Hussey, C. An Electrochemical and Spectroscopic Study of Nd(III) and Pr(III) Coordination in the 1-Butyl-1-Methylpyrrolidinium Bis(Trifluoromethylsulfonyl)Imide Ionic Liquid Containing Chloride Ion. *Inorg. Chem.* **2014**, *53* (11), 5750–5758. <https://doi.org/10.1021/ic5005616>.
- (128) Grodkowski, J.; Neta, P. Reaction Kinetics in the Ionic Liquid Methyltributylammonium Bis(Trifluoromethylsulfonyl)Imide. Pulse Radiolysis Study of •CF₃ Radical Reactions. *J. Phys. Chem. A* **2002**, *106* (22), 5468–5473. <https://doi.org/10.1021/jp020165p>.
- (129) F. Wishart, J.; Neta, P. Spectrum and Reactivity of the Solvated Electron in the Ionic Liquid Methyltributylammonium Bis(Trifluoromethylsulfonyl)Imide. *J. Phys. Chem. B* **2003**, *107* (30), 7261–7267. <https://doi.org/10.1021/jp027792z>.
- (130) Tang, Y.; Wang, Z.; Chi, X.; D. Sevilla, M.; Zeng, X. In Situ Generated Platinum Catalyst for Methanol Oxidation via Electrochemical Oxidation of Bis(Trifluoromethylsulfonyl)Imide Anion in Ionic Liquids at Anaerobic Condition. *J.*

- Phys. Chem. C* **2016**, *120* (2), 1004–1012. <https://doi.org/10.1021/acs.jpcc.5b09777>.
- (131) Dietz, M. L.; Stepinski, D. C. Anion Concentration-Dependent Partitioning Mechanism in the Extraction of Uranium into Room-Temperature Ionic Liquids. *Talanta* **2008**, *75* (2), 598–603. <https://doi.org/10.1016/J.TALANTA.2007.11.051>.
- (132) Shen, Y.; Wu, J.; Liu, Z.; Wu, W. Environmentally Friendlier Approach to Nuclear Industry: Recovery of Uranium from Carbonate Solutions Using Ionic Liquids. *Ind. & Eng. Chem. Res.* **2015**, *54* (34), 8624–8628. <https://doi.org/10.1021/acs.iecr.5b02137>.
- (133) Vasudeva Rao, P. R.; Venkatesan, K. A.; Srinivasan, T. G. Studies on Applications of Room Temperature Ionic Liquids. *Prog. Nucl. Energy* **2008**, *50* (2–6), 449–455. <https://doi.org/10.1016/J.PNUCENE.2007.11.079>.
- (134) Giridhar, P.; Venkatesan, K. A.; Subramaniam, S.; Srinivasan, T. G.; Vasudeva Rao, P. R. Extraction of Uranium (VI) by 1.1 M Tri-n-Butylphosphate/Ionic Liquid and the Feasibility of Recovery by Direct Electrodeposition from Organic Phase. *J. Alloys Compd.* **2008**, *448* (1–2), 104–108. <https://doi.org/10.1016/J.JALLCOM.2007.03.115>.
- (135) Li, R.; Dalton, J.; Joly, F.; Simon, P.; Trivelli, X.; Arab, M.; Morel, B.; Solari, P. L.; Paul, J.-F.; Moisy, P.; et al. Direct Conversion of Uranium Dioxide UO₂ to Uranium Tetrafluoride UF₄ Using the Fluorinated Ionic Liquid [Bmim][PF₆]. *Dalt. Trans.* **2019**, *49*, 274. <https://doi.org/10.1039/c9dt04327f>.
- (136) Ohashi, Y.; Asanuma, N.; Harada, M.; Wada, Y.; Matsubara, T.; Ikeda, Y. Application of Ionic Liquid as a Medium for Treating Waste Contaminated with UF₄. *J. Nucl. Sci. Technol.* **2009**, *46* (8), 771–775.
- (137) Bossé, E.; Den Auwer, C.; Berthon, C.; Guilbaud, P.; S. Grigoriev, M.; Nikitenko, S.; Le

- Naour, C.; Cannes, C.; Moisy, P. Solvation of UCl_6^{2-} Anionic Complex by MeBu_3N^+ , BuMe_2Im^+ , and BuMeIm^+ Cations. *Inorg. Chem.* **2008**, *47* (13), 5746–5755. <https://doi.org/10.1021/ic702477z>.
- (138) Zarzana, C. A.; Groenewold, G. S.; Benson, M. T.; Delmore, J. E.; Tsuda, T.; Hagiwara, R. Production of Gas-Phase Uranium Fluoroanions Via Solubilization of Uranium Oxides in the $[\text{1-Ethyl-3-Methylimidazolium}][\text{F}(\text{HF})_2.3]^-$ Ionic Liquid. *J. Am. Soc. Mass Spectrom.* **2018**, *29* (10), 1963–1970.
- (139) Wagner, W.; Edelstein, N.; Whittaker, B.; Brown, D. Spectral Properties of Bis(Tetraethylammonium) Uranium Hexaiodide Bis(Tetraethylammonium) Uranium Hexafluoride. *Inorg. Chem.* **2002**, *16* (5), 1021–1026. <https://doi.org/10.1021/ic50171a010>.
- (140) Ryan, J.; Klixbüll Jørgensen, C.; L Ryan, by J.; Klixbull Jorgensen, C. Molecular Physics Electron Transfer and $5f \rightarrow 6f$ Transitions in Uranium(IV), Neptunium(IV), Plutonium(IV) Hexahalides Electron Transfer and $5f$ -, $6f$ Transitions in Uranium(IV), Neptunium(IV), Plutonium(IV) Hexahalides. **1964**, *7* (1), 17–29. <https://doi.org/10.1080/00268976300100781>.
- (141) Aoyagi, N.; Watanabe, M.; Kirishima, A.; Sato, N.; Kimura, T. Optical Properties of Tetravalent Uranium Complexes in Non-Aqueous Media. <https://doi.org/10.1007/s10967-014-3616-x>.
- (142) Ballhausen, C. J. The Crystal Field Splittings in the $5f$ Complexes. *Theor. Chim. Acta* **1972**, *24* (2), 234–240.
- (143) DeVore, M. A.; Villa-Aleman, E.; Felder, J. B.; Yeon, J.; zur Loye, H. C.; Wellons, M. S. Vibrational Spectroscopy of Uranium Tetrafluoride Hydrates. *Vib. Spectrosc.* **2021**, *115*,

103277. <https://doi.org/10.1016/J.VIBSPEC.2021.103277>.

- (144) Wagner, W.; Edelstein, N.; Whittaker, B.; Brown, D. Spectral Properties of Bis (Tetraethylammonium) Uranium Hexaiodide Bis (Tetraethylammonium) Uranium Hexafluoride. *Inorg. Chem.* **1977**, *16* (5), 1021–1026.
- (145) Shamir, J.; Silberstein, A. Laser Raman Spectra of the Uranium Hexachloride Molecule and Anions (UCl_6 , UCl_6^- 1 and UCl_6^- 2). *J. Inorg. Nucl. Chem.* **1975**, *37* (5), 1173–1175.
- (146) Abbott, K.; Geroux, Z.; Lubke, K. *Uranium Hexafluoride Processing Using Ionic Liquids*; 2017.
- (147) Haire, M. J.; Croff, A. G. *DUF6 Materials Use Road Map*; 2001.
- (148) Hatchett, D. W.; Higgins, C. J. Lithium Recovery from Lithium Salts Dissolved in Ionic Liquids. WO/2021/178748, 2021.

Curriculum Vitae

Cassara J. Higgins, Ph.D.

CassaraHiggins@gmail.com

Education

Ph.D. – Radiochemistry: University of Nevada, Las Vegas, Las Vegas, NV, May 2022.

B.Sc. – Chemistry: University of Northern Iowa, Cedar Falls, IA, May 2016.

B.Sc. – Physics: University of Northern Iowa, Cedar Falls, IA, May 2016.

Research Experiences

Ph.D. Dissertation Research – Advisor: Dr. David W. Hatchett. *The Dissolution and Recovery of Critical Materials (Li_2CO_3 and UF_6) from Ionic Liquid*, August 2016 thru May 2022.

Investigated and determined pathways for dissolution of Li_2CO_3 and UF_6 into ionic liquids (ILs). Characterized species in solution utilizing UV-Vis, FTIR, Raman, EXAFS, and electrochemical methods. Routes of recovery of lithium and uranium were determined through electrochemical reduction and precipitation. Precipitates were characterized using PXRD, TGA, SEM-EDS, UV-Vis, FTIR, and Raman.

Idaho National Lab Graduate Intern – Advisor: Dr. Donna Baek, Summer 2017. Investigated the recovery of $\text{Ln}(\text{H}_2\text{O})_x(\text{TFSI})_x$ compounds from IL using supercritical CO_2 as an extraction medium. Gained experience building high pressure system (up to 5000 psi).

Undergraduate Honors Thesis – Advisor: Dr. Colin Weeks, *Magnetic Properties of Cobalt(II) Containing Metal-Organic Frameworks*, May 2013 thru May 2016. Synthesized MOFs with $\text{Co}(\text{NO}_3)_2$ metal centers and 4,4'-bipyridine organic linkers. Multiple MOF structures were created and characterized using SCXRD, PXRD, and elemental analysis. Magnetic properties of the MOFs were measured using a PPMS.

Idaho National Lab Undergraduate Intern – Advisor: Dr. Travis Grimes, Summer 2015. Determined lanthanide K_a of several possible actinide holdback reagents to be used in advanced TALSPEAK processes.

Presentations

1. Higgins, C. J.; Lubke, K. I.; Poineau, F.; Czerwinski, K. R.; Hatchett, D. W. **“Dissolution of Uranium Hexafluoride and Precipitation of uranium from 1-Methyl-1-Propylpiperidinium Bis(trifluoromethylsulfonyl)imide”**, MARC XII, Kona, HI, April 3-8, 2022.
2. Higgins, C. J.; Lubke, K. I.; Poineau, F.; Czerwinski, K. R.; Hatchett, D. W. **“Reduction and Recovery of Uranium Hexafluoride from 1-Methyl-1-Propylpiperidinium Bis(trifluoromethylsulfonyl)imide”**, 44th Annual Actinide Separations Conference, Virtual, May 18-20, 2021.
3. Higgins, C. J.; Lubke, K. I.; Czerwinski, K. R.; Hatchett, D. W. **“The reduction of uranium hexafluoride with a room temperature ionic liquid (1-methyl-1-propylpiperidinium bis(trifluoromethylsulfonyl)imide)”**, International Youth Nuclear Congress 2020, Sydney, Australia, March 8-14, 2020.
4. Higgins, C. J.; Lubke, K. I.; Czerwinski, K. R.; Hatchett, D. W. **“The reduction of uranium hexafluoride with a room temperature ionic liquid (1-methyl-1-propylpiperidinium bis(trifluoromethylsulfonyl)imide)”**, ACS Spring 2019 National Meeting, Orlando, Florida, March 31- April 4, 2019.
5. Higgins, C. J.; Shand, P. M.; Weeks, C. L. **“Magnetic properties of cobalt(II) containing metal-organic frameworks”**, 251st National ACS Meeting, San Diego, CA March 9-17, 2016.
6. Higgins, C. J.; Weeks, C. L. **“Building a brick wall: Creating Metal Organic Frameworks”**, 247st National ACS Meeting, Dallas, TX, March 17-19, 2014.
7. Higgins, C. J.; Weeks, C. L. **“Building a brick wall: Creating Metal Organic Frameworks”**, 23rd Annual Argonne Undergraduate Symposium, Chicago, IL, November 1, 2013.

Publications

1. Higgins, C. J.; Lubke, K. I.; Poineau, F.; Czerwinski, K. R.; Hatchett, D. W. “**Direct Dissolution and Spectroscopic Characterization of Uranium Hexafluoride in Ionic Liquid**”, (2022) *J. Radioanal. Nucl. Chem.*, Submitted.
2. Poineau, F.; Louis-Jean, J.; Jang, H.; Higgins, C. J.; Balasekaran, S. M.; Hatchett, D. W.; Sattelberger, A. P. “**X-ray absorption fine structure spectroscopic study of $(\text{NH}_4)_2\text{ReF}_6$** ”, (2019) *SN Applied Sciences* 1(11), 1-7.

Patents

1. Hatchett, D. W.; Czerwinski, K. R.; Lubke, K. I.; Higgins, C. J. *Conversion of Uranium Hexafluoride and Recovery of Uranium from Ionic Liquids*. Patent WO/2020/204879. 08 Oct 2020.
2. Hatchett, D. W.; Higgins, C. J. *Stoichiometric Recovery of UF_4 from UF_6 Dissolved in Ionic Liquids*. Patent WO/2021/178751. 09 Oct 2021.
3. Hatchett, D. W.; Higgins, C. J. *Lithium Recovery from Lithium Salts Dissolved in Ionic Liquids*. Patent WO/2021/178748. 09 Oct 2021.